



TECHNISCHE UNIVERSITÄT WIEN

MASTER THESIS

Anchor losses of non-slender MEMS resonators and the impact of mode shape interference at frequency crossing and avoided crossing

for the achievement of the academic degree

DIPLOM-INGENIEUR

*in the field of study Electrical Engineering
submitted in the*

Faculty of Electrical Engineering and Information Technology, ETIT

at the

Institute of Sensor and Actuator Systems, ISAS

under the supervision of

Univ.Prof. Dipl.-Phys. Dr.rer.nat. Ulrich Schmid

and co-supervision of

Daniel Platz, MSc. PhD
Dr.techn. Andre Loch Gesing, MEng.

by

Erwin Gietl, BSc.

Matr.Nr.: 01526986

Vienna, May 2024



Die approbierte gedruckte Originalversion dieser Diplomarbeit ist an der TU Wien Bibliothek verfügbar
The approved original version of this thesis is available in print at TU Wien Bibliothek.

Acknowledgments

First and foremost, I would like to express my deepest gratitude to Prof. Ulrich Schmid for providing me with the opportunity to undertake this work. His support has been instrumental in making this thesis possible.

I am profoundly thankful to my supervisor, Daniel Platz, PhD, for his invaluable ideas, suggestions, and guidance throughout this journey. His expertise and insights have shaped this thesis into its final form.

I extend my heartfelt thanks to Dr.techn. Andre Loch Gesing for his unwavering support, countless discussions, and thorough assessments. His continuous support and technical expertise were crucial for the progress of this research.

Finally, I would like to express my sincerest appreciation to my fiancée, Valerie, for her unwavering support and encouragement during this time. Her understanding and patience have been a cornerstone of my efforts.

Abstract

This work investigates frequency crossing phenomena in non-slender MEMS resonators. Special focus is put on the influence of anchor losses and the related quality factors (Q-factors). To evaluate the anchor losses and resonance frequencies of higher-order-out-of-plane (HO-OOP) modes, a mathematical model of the resonator is developed and solved with the finite element method (FEM). The results show that non-slender geometries vibrating in OOP modes exhibit very high Q-factors up to 10^7 , while in-plane (IP) mode shapes have low Q-factors below 10. These results motivated an extensive investigation into the OOP and IP vibrational modes, their Q-factors, and resonance frequencies as the resonator changes from a slender beam to a wider plate. The resonance frequencies of different mode shapes evolve differently when the width of non-slender resonators is increased, and at some widths, the resonance frequencies cross. Three phenomena are identified: simple crossing, avoided crossing, and "Q-drop" crossing. Simple crossing does not exhibit an interference between the crossing mode shapes, and their Q-factors are not changed. The avoided crossing describes the repulsion of the natural frequencies while increasing the width due to the strong coupling of the natural modes. "Q-drop" crossing does not affect the resonance frequencies but drastically reduces the quality factor of a single mode. A novel method for mathematically analyzing modal displacement patterns is introduced, employing the Fourier transformation (FT) to analyze these mode shape interference patterns that significantly affect the Q-factor. In avoided crossing, the vibrational modes and Q-factors are exchanged while the resonance frequencies are repelled from each other. In "Q-drop" crossing, the displacement patterns of the interfering mode shapes are only slightly affected. Avoided crossing occurs between OOP-OOP modes, as well as OOP-IP, while "Q-drop" crossing occurs only in OOP-IP resonance frequency crossing. The identified phenomena explain the Q-factor drop in previous experimental studies.

Kurzfassung

In dieser Arbeit werden die auftretenden Phänomene bei Kreuzung der Resonanzfrequenzen in nicht schlanken MEMS-Resonatoren untersucht. Besonderes Augenmerk wird auf den Einfluss der Ankerverluste und die damit verbundenen Qualitätsfaktoren (Q-Faktoren) gelegt. Zur Bewertung der Ankerverluste und der Resonanzfrequenzen von out-of-plane Moden höherer Ordnung (HO-OOP) wird ein mathematisches Modell des Resonators entwickelt und mit der Finite-Elemente-Methode (FEM) gelöst. Die Ergebnisse zeigen, dass nicht-schlank Geometrien, die in OOP-Moden schwingen, sehr hohe Q-Faktoren bis zu 10^7 aufweisen, während in-plane (IP) Modenformen niedrige Q-Faktoren unter 10 haben. Diese Ergebnisse motivierten zu einer umfassenden Untersuchung der OOP- und IP-Schwingungsmoden, ihrer Q-Faktoren und Resonanzfrequenzen, wenn der Resonator von einem schlanken Balken zu einer breiteren Platte wechselt. Die Resonanzfrequenzen der verschiedenen Modenformen entwickeln sich unterschiedlich, wenn die Breite von nicht schlanken Resonatoren erhöht wird, und bei einigen Breiten kreuzen sich dadurch die Resonanzfrequenzen. Drei Phänomene werden unterschieden: simple crossing, avoided crossing und "Q-drop" crossing. Bei simple crossing kommt es zu keiner Interferenz zwischen den sich kreuzenden Modenformen, und ihre Q-Faktoren werden nicht verändert. Avoided crossing beschreibt die Abstoßung der Eigenfrequenzen bei gleichzeitiger Vergrößerung der Breite aufgrund der starken Kopplung der Eigenformen. "Q-drop"-crossing hat keinen Einfluss auf die Resonanzfrequenzen, verringert aber den Qualitätsfaktor einer einzelnen Mode drastisch. Es wird eine neuartige Methode zur mathematischen Analyse von Modenformen vorgestellt, bei der die Fourier-Transformation (FT) eingesetzt wird, um die Interferenzmuster der Moden zu analysieren, die den Q-Faktor erheblich beeinflussen. Bei avoided crossing werden die Schwingungsmoden und Q-Faktoren ausgetauscht, während die Resonanzfrequenzen voneinander abgestoßen werden. Bei der "Q-drop"-Kreuzung werden die Modenformen durch die Überlagerung nur sehr gering verändert. Avoided crossing tritt sowohl zwischen den OOP-OOP-Moden als auch zwischen den OOP-IP-Moden auf, während die "Q-drop"-Kreuzung nur bei der OOP-IP-Resonanzfrequenzkreuzung auftritt. Die festgestellten Phänomene erklären den Abfall des Q-Faktors in früheren experimentellen Studien.

Contents

1	Introduction	1
2	Numerical model for wider MEMS resonators	4
2.1	Analytic models for different dissipation mechanisms	4
2.1.1	Resonance frequency	4
2.1.2	Anchor losses	6
2.1.3	Thermoelastic damping	6
2.1.4	Volume and surface losses	7
2.1.5	Combined results of damping mechanisms	8
2.2	Numerically modeling of anchor losses for non-slender geometries	9
2.3	Convergence and validation of the FEM model	12
2.4	Adaptation of the model to fabricated MEMS resonators	13
2.5	Conclusions	15
3	Vibrational modes and anchor losses on non-slender resonators	16
3.1	The slender beam resonator	17
3.1.1	Analysis of the displacement patterns	17
3.1.2	Analysis of the anchor losses	19
3.1.3	Analysis of the mechanical energy flux	20
3.2	A square plate resonator	23
3.2.1	Analysis of higher-order displacement patterns	23
3.2.2	Analysis of the anchor losses	24
3.2.3	Analysis of the mechanical energy flux	25
3.3	The wider rectangular plate resonator	26
3.3.1	Analysis of the anchor losses	26
3.3.2	Analysis of the mechanical energy flux	27
3.4	Conclusions	28
4	Avoided crossing and "Q-drop" crossing in cantilevered plates	30
4.1	Fourier transformation based mode shape identification	32
4.2	Anchor losses of higher-order-out-of-plane mode shapes	37
4.2.1	Mode shape interference on 1:3 RTS mode related paths	38
4.2.2	Analysis of mode shape interference on other paths	48
4.2.3	Comparison of anisotropic silicon and polycrystalline silicon	57
4.2.4	Summary of interfering mode shapes	57
4.3	Conclusions	58
5	Conclusions and outlook	60

Appendix	62
A Definition of the exported Data from <i>Comsol Multiphysics</i>	63
B Interfering mode shapes	63
B.1 Avoided crossing between path <i>L</i> and <i>M</i>	63
B.2 "Q-drop" crossing on path <i>S</i>	67
B.3 Avoided crossing between path <i>P</i> and <i>S</i>	68
B.4 Avoided crossing between path <i>O</i> and <i>P</i>	71
C Results ploycrystalline silicon	73
List of Figures	79
List of Symbols	82
List of Acronyms	83
Bibliography	83

1 Introduction

Since the first commercial device in the late 1980s, Micro-Electro-Mechanical Systems (MEMS) has been a success story. In the last decade, the development was pushed by mobile devices and the Internet of Things (IoT) [1]. MEMS devices are used as sensors, e.g., for mass sensing [2], accelerometers [3]; as actuators, e.g., for fluid pumps [4], audio applications [5], RF switches [6]; for communication, e.g., within 5G mobile transmitters [7], as energy harvesters [8]; and for many other applications.

MEMS resonators or resonant MEMS are a special class of MEMS. MEMS resonators are mechanical structures that are capable of vibrating mechanically and are typically operated in resonance. Applying an external oscillating force to the device generates a vibrational deformation pattern on the resonator. Changing the frequency of the applied force will result in different displacement patterns appearing on the resonator surface. At some specific frequencies, the displacement amplitude increases sharply while the applied force remains the same. These frequencies are called resonance frequencies, or also natural frequencies or eigenfrequencies. When the resonator is excited with a natural frequency, the corresponding displacement pattern is called the eigenmode. Each eigenmode shows a specific mode shape. A higher amplitude of the mode shapes requires more stored energy in the resonator. As the energy supplied by the external force remains constant, the dissipated energy has to decrease at the resonance frequency. MEMS resonators with lower energy dissipation tend to oscillate more stable in frequency with less supplied energy. Therefore, the ratio between the stored and dissipated energy is a key parameter that characterizes the performance of MEMS resonators. This parameter is called the quality factor or Q-factor, defined as

$$Q = 2\pi \frac{\text{Energy stored}}{\text{Energy dissipated per cycle}}, \quad (1.1)$$

where the stored energy includes the kinetic energy and the potential energy, and the dissipated energy is the portion of energy the resonator loses to its environment during each oscillation cycle. Resonant MEMS with high Q-factors can be used to build sensors with higher sensitivity, an often required design feature. Therefore, many research activities were taken to develop high Q-factor devices or even the tuning of this important parameter [9].

The dissipation of energy on MEMS resonators is also interpreted as damping. Damping refers to the process of reducing the amplitude of oscillations. Damping is affected by various mechanisms, depending on material properties, design properties, and environmental conditions. The major intrinsic dissipation mechanisms are thermo-elastic damping (TED) and anchor losses, also called clamping losses [10]. Furthermore, volume losses and surface losses are also not negligible factors [11]. The environment can also contribute to damping, e.g., if the resonator is immersed in fluid [12] or other external forces are applied to the resonator, e.g., electrical fields [13]. The sum of all participating

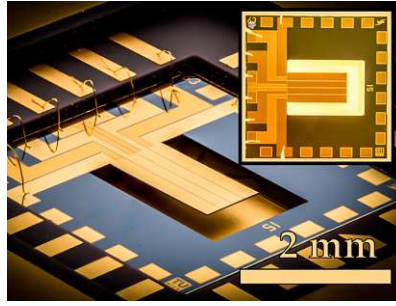


Figure 1.1: Fabricated MEMS cantilevered plate resonator [14]

factors is the total quality factor given by

$$\frac{1}{Q_{\text{Total}}} = \sum_i \frac{1}{Q_i} = \frac{1}{Q_{\text{Clamping}}} + \frac{1}{Q_{\text{TED}}} + \frac{1}{Q_{\text{Volume}}} + \frac{1}{Q_{\text{Surface}}} + \frac{1}{Q_{\text{Environment}}}. \quad (1.2)$$

Cantilevered resonators are ideally suited for investigations on these various dissipation mechanisms. Figure 1.1 shows an example of a fabricated device. The cantilever resonator has a very simple structure that does not impose any restrictions on the findings for resonators with multiple carriers. The implementation as a slender beam resonator has been part of research since the late 60s [15]. Still, nowadays, many research activities are taking place for this structure. It is used in many MEMS devices, e.g., atomic force microscopy [16], magneto-resistive sensing [17], and gas sensing [18]. Further possible applications are part of current research, e.g., MEMS timing devices [19] and energy harvesting MEMS for wireless applications [20].

Previous work [12, 21] has shown a high potential for reducing anchor losses using higher-order-out-of-plane mode shapes. For the slender beam resonator, analytical methods were presented for the natural frequency [22] and individual aspects of damping [23, 24]. However, all the analytic solutions presented so far are limited to one-dimensional oscillation. Investigations into resonator designs for higher-order-out-of-plane mode shapes have shown that wider plates could better suit this purpose. However, Stixenberger [21] showed a significant change in the Q-factor in small width in-

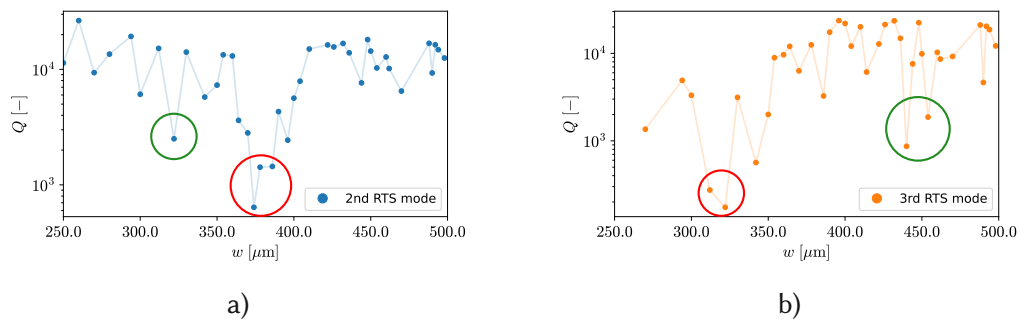


Figure 1.2: Measured quality factor of roof-tilde-shaped modes at different widths w of fabricated devices reported by Stixenberger [21]

tervals in the experimental results for some mode shapes. Figure 1.2 shows in a) the quality factor for the 2nd roof-tilde-shaped mode. The strongest dip is circled in red and shows a very sharp decrease of around 1.5 orders of magnitude. Between the initial high Q-factor and the lowest value, the width only increases by $14\mu\text{m}$. The increase in the Q-factor is also quite strong, with a change in width of only $36\mu\text{m}$. For the second dip circled in green, the quality factor decreases and increases by more than $12 \cdot 10^3$ in an interval of less than $20\mu\text{m}$. In b), the 3rd roof-tilde-shaped mode is shown. The strongest dip is also marked in red and shows a drop in Q-factor of more than one order of magnitude within an interval of $30\mu\text{m}$. Around a width of $450\mu\text{m}$ two strong decreases of more than one order of magnitude are marked in green. Both plots also show some other outliers, but the described examples affect the quality factor much more strongly. Further investigations on plate resonators are needed to understand the reasons for this behavior in the Q-factor.

Goal:

In this work, higher-order-out-of-plane mode shapes on non-slender geometries are analyzed, with a focus on resonance frequency and Q-factor. The MEMS plate resonator is modeled numerically and solved with the Finite Element Method (FEM). To improve the understanding of the relation between the anchor losses and mode shapes, the mechanical energy flow in the modeled substrate is discussed. Further, the resulting displacement patterns are analyzed with a mathematical method to identify the appearing mode shapes. The main objective is to investigate Q-factor-related mode shape interference phenomena, such as avoided crossing and other superposition effects.

2 Numerical model for wider MEMS resonators

In this chapter, the analytic solutions for EB mode shapes will be discussed. Figure 2.1 a) shows the unexcited cantilever resonator and b) the resonator excited by the 2nd EB mode. To analyze anchor losses of higher-order mode shapes, it will establish a general physical model, which is solved numerically using the Finite Element Method (FEM). The numerical solution of the model is validated using the analytical solution. In addition, the parameters for the accuracy of the solution are defined to achieve the objective of this work. The analytical solutions are based on simplifications of the geometry and the material. However, they are relevant for a more realistic model to evaluate mode shapes. Therefore, the physical model will be adapted to define a model closer to fabricated MEMS cantilever resonators.

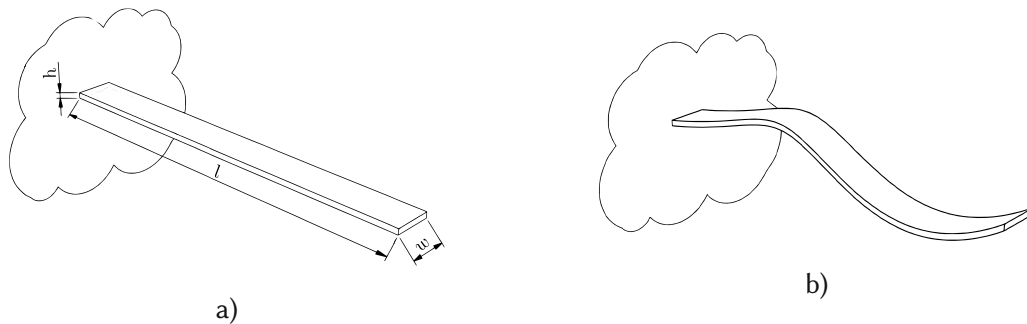


Figure 2.1: Cantilever resonator, in a) in the non-excited state, and in b) excited in the 2nd Euler-Bernoulli mode

2.1 Analytic models for different dissipation mechanisms

Understanding which dissipation mechanism dominates in cantilever resonators is essential. Therefore, the analytic solutions for the individual components of the damping factor are presented and compared. Before diving into the different loss mechanisms, the analytic solution for the second important characteristic is presented, the resonance frequency. In order to quantitatively evaluate the analytical models, their solutions are presented for silicon resonators with different lengths. The material properties and the resonator dimensions are defined in Table 2.1.

2.1.1 Resonance frequency

Judge et al. [22] presented an analytic solution for the natural frequency of cantilever resonators as

$$f_n = \frac{1}{2\pi} k_m^2 \sqrt{\frac{EI_{in}}{\rho wh}}, \quad (2.1)$$

Material properties of isotropic silicon:

Young's modulus:	$E = 170 \text{ GPa}$
Poisson's ratio:	$\nu = 0.28$
Mass density:	$\rho = 2329 \text{ kg/m}^3$
Thermal expansion coefficient:	$\alpha_{th} = 2.6 \cdot 10^{-6} \text{ 1/K}$
Thermal conductivity:	$\kappa = 130 \text{ W/(m}\cdot\text{K)}$
Heat capacity:	$C_p = 700 \text{ J/(kg}\cdot\text{K)}$

Cantilever Resonator:

Resonator length:	$l = \{100; 200; 300; 400; 500; 1000\} \mu\text{m}$
Resonator width:	$w = 100 \mu\text{m}$
Resonator thickness:	$h = 15 \mu\text{m}$

Table 2.1: Material properties and dimensions for quantitative evaluation

with E the Young's modulus, I_{in} the moment of inertia, ρ the mass density, w the width, h the thickness and, k_m is the root of the eigenvalue λ_m , defined from equation

$$\cosh(\lambda_m) \cdot \cos(\lambda_m) = -1, \quad \lambda_m \in \{\lambda_1, \lambda_2, \dots, \lambda_n\} \quad (2.2)$$

with $\lambda_m = k_m l$, where l is the length of the cantilever. For each eigenvalue λ_m exists an eigenmode, the displacement pattern of the cantilever. This equation is derived from EB assumptions and gives only eigenvalues for EB mode shapes [11]. The moment of inertia I_{in} of the resonator is defined as

$$I_{in} = \frac{wh^3}{12}. \quad (2.3)$$

Inserting I_{in} and λ_m in Equation 2.1 lead to

$$f_n = \frac{1}{2\pi} \lambda_m^2 \frac{h}{l^2} \sqrt{\frac{E}{12\rho}}, \quad (2.4)$$

which shows that the natural frequency for resonators of the same material decreases by h/l^2 . Cantilever resonators are desired to have a very small ratio between thickness and length ($h/l \ll 1$) because of other properties discussed later in this section. Therefore, length is the dominant factor, which leads to a quadratic decrease in resonance frequency. This drawback of EB mode shapes on slender beam resonators is depicted in Figure 2.2.

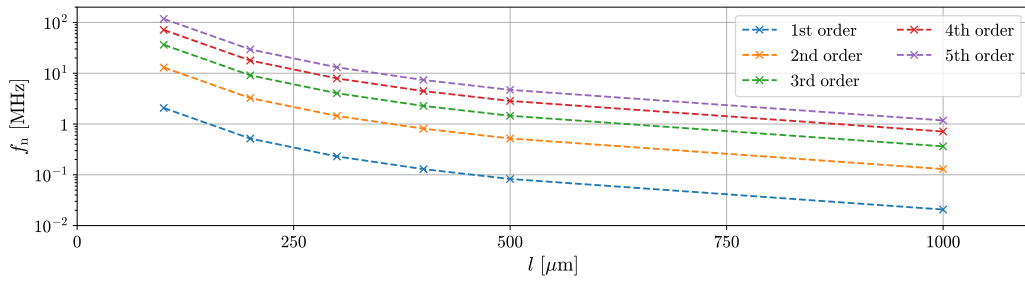


Figure 2.2: Natural frequency f_n of the EB modes for the first five eigenvalues for different lengths l . The resonator material properties and geometry are defined in Table 2.1

2.1.2 Anchor losses

The anchor losses refer to the dissipation of vibrational energy through the support that connects the resonating structure to the substrate. This region is directly exposed to the cantilever deformation field and significantly influences the kinetic energy flow into the substrate. For this damping mechanism, Wilson-Rae [23] presented the analytic solution for the quality factor as

$$Q_{\text{anchor}} = \frac{3.9}{\pi^4 \gamma C_m} \frac{l^5}{wh^4} \left(\frac{3\pi}{2\lambda_m} \right)^4, \quad (2.5)$$

with the number of supports γ equals 1 for the clamped-free beam and the additional damping factor

$$C_m = \left(\tanh^2 \frac{\lambda_m}{2} \right)^{(-1)^m}, \quad m \in \mathbb{N}, \quad (2.6)$$

depending only from eigenvalue λ_m and its order m .

Equation 2.5 shows that, for resonators of the same material, the anchor losses of EB mode shapes mainly depend on the ratio between height and length. Therefore, to achieve high Q-factors, this ratio is desired to be very small. Furthermore, the anchor loss Q-factor depends inversely on the width. Therefore, lower quality factors for EB modes are expected on wider plates.

2.1.3 Thermoelastic damping

The oscillating displacement of the mode shapes leads to compression and stretching inside the cantilever structure. These elastic deformations influence the temperature field of the resonator and lead to a dissipative flow of thermal energy in the material. Roszhart et al. [25] presented a solution for the Q-factor of the thermoelastic damping as

$$Q_{\text{TED}} = \frac{1}{2\Gamma(T)\Omega(f)}, \quad (2.7)$$

where Γ contains the material parameters as

$$\Gamma(T) = \frac{\alpha_{th}^2 TE}{4\rho C_p}, \quad (2.8)$$

including the thermal expansion coefficient α_{th} and the specific heat capacity C_p , and temperature T of the resonator. Furthermore, Equation 2.7 contains Ω

$$\Omega(f) = \frac{2f/F_0}{1 + (f/F_0)^2}, \quad (2.9)$$

depending only from ratio between the frequency in the resonator f and the characteristic damping frequency of the resonator F_0 , defined as

$$F_0 = \frac{\pi \kappa}{2\rho C_p} \frac{1}{h^2}, \quad (2.10)$$

with in the first term the thermal conductivity κ and other material properties, and in the second term only the cantilever thickness.

Assuming the material remains the same, the TED depends only on the thickness of the resonator and not on length and or width. To improve the Q-factor for TED, the ratio of f/F_0 shall be much higher or much lower than one so that Ω becomes small. Therefore, for the desired frequencies $f \approx f_n$ from equation 2.1, MEMS resonators' thickness shall be very small.

2.1.4 Volume and surface losses

The elasticity of the material itself contributes to the quality factor of the resonator. Volume and surface losses are related significantly to the elasticity of the used material.

Yasumura et al. [24] presented the quality factor for volume loss as

$$Q_{\text{Volume}} = \frac{\Re(E^*)}{\Im(E^*)}, \quad (2.11)$$

depending only on the complex Young's modulus E^* . This modulus is a material property affected neither by the resonator dimensions nor the eigenmodes. Montalvão et al. [26] describe the real part as equal to Young's modulus E and the imaginary part as the losses modulus. The loss modulus is defined as $E\eta$ with the material loss coefficient η . So E^* is represented as $E(1 + j\eta)$, and the volume quality factor depends only on the inverse loss coefficient. Ashby [27] estimated the loss coefficient for SiO_2 below $2 \cdot 10^{-5}$, resulting in a Q_{Volume} above $5 \cdot 10^4$.

Furthermore, Yasumura et al. [24] calculate the quality factor for surface loss as

$$Q_{\text{Surface}} = \frac{wh}{2\delta(3w + h)} \frac{\Re(E)}{\Im(E_s)}, \quad (2.12)$$

depending on the resonator's width and height, the surface layer thickness δ , the com-

plex Young's modulus E^* , and the surface layer complex Young's modulus E_S^* . For E_S^* , neither analytic expressions nor experimental values are known. A value of above 10^5 for the surface quality factor is found from experiments.

No strategies were presented to improve these two quality factors. Therefore, they are defining together the maximum possible Q-factor for fabricated silicon MEMS resonators of all possible geometries and mode shapes.

2.1.5 Combined results of damping mechanisms

Figure 2.3 shows the total quality factor, defined in Equation 1.2, including all presented components. This plot demonstrates that EB mode shapes trend to higher Q-factors on more slender geometries because of the decreasing height-to-length ratio. However, the initial increase is much stronger for higher EB orders. This Q-factor increase is related to the eigenvalue dependency of the anchor losses. Nevertheless, at higher lengths, the impact of the volume and surface losses delimits the increase.

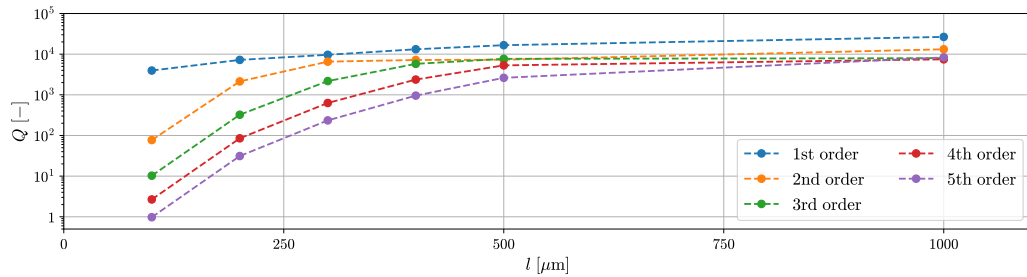


Figure 2.3: Total quality factor of the EB modes for the first five eigenvalues assuming isotropic silicon cantilevers with $w = 100 \mu\text{m}$, $h = 15 \mu\text{m}$ and different lengths l from the interval $100 \mu\text{m}$ to $1000 \mu\text{m}$.

In Figure 2.4, the total Q-factor and its single components are plotted over the natural frequency. For resonance frequencies between 100 kHz and 1 MHz, the TED is the limiting mechanism. Above 3 MHz, the anchor losses for the EB mode shapes dominate, and the Q-factor decreases strongly. From the estimated individual loss mechanisms, it is concluded that all mode shapes with a quality factor for anchor losses above 10^3 and natural frequencies above 3 MHz are considered for high Q-factor resonators. Previous studies have shown that HO-OOP mode shapes have much higher Q-factors for the anchor losses than EB modes [21]. Therefore, a numerical model is developed in the next section to determine the plate resonators' anchor losses.

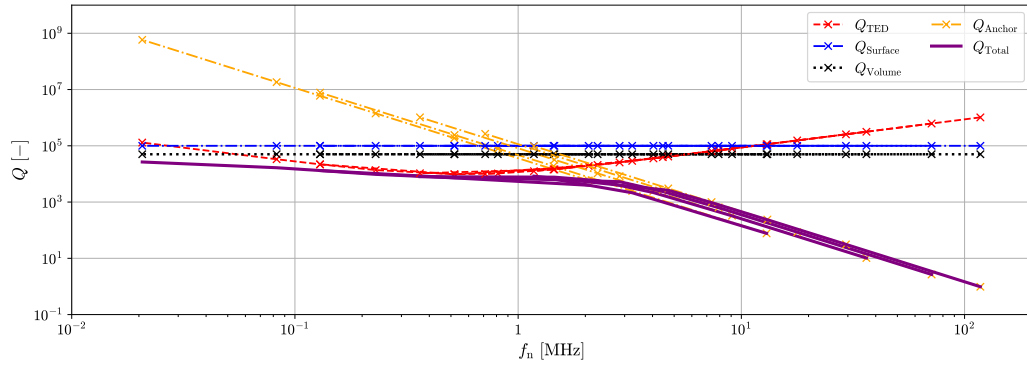


Figure 2.4: Total quality factor and as well as individual Q-factor contributions plotted over the frequency range of the first five EB mode shapes assuming isotropic silicon cantilevers with $w = 100 \mu\text{m}$, $h = 15 \mu\text{m}$ and different lengths l starting from $100 \mu\text{m}$ to $1000 \mu\text{m}$.

2.2 Numerically modeling of anchor losses for non-slender geometries

No analytical solutions for resonance frequency and quality factor were found for non-slender resonator designs. Using a mathematical model of the material and applying this to a given geometry makes it possible to solve this complex problem numerically. The most important property of resonating cantilevers is that all deformations are small, in the range of a few nanometers. So, it can be assumed a linear behavior of the material and only elastic deformations. Therefore, the theory of linear elasticity is used to model the resonator's mechanical behavior. The theory of linear elasticity uses a set of equations to describe the state of stress, strain, and displacement at each point of an elastically deformable structure [28]. The stress represents the forces during deformation, and the strain represents the deformation. The spatial displacement, in its vector representation \mathbf{u} , is given from the solution of the equation of motion for continuum mechanics. The environmental damping shall not be part of the model. Therefore, the undamped version of this equation is used, defined as

$$\rho \frac{\partial^2 \mathbf{u}}{\partial t^2} - \nabla \cdot \boldsymbol{\sigma} = \mathbf{F}, \quad (2.13)$$

where ρ is the mass density, \mathbf{F} is an external force density and $\boldsymbol{\sigma}$ the stress tensor [30]. To solve this partial differential equation (PDE) is needed to define the stress tensor. From the generalized Hooke's law the stress tensor σ_{ij} for linear materials is given as

$$\sigma_{ij} = \mathbf{K}_{ijkl} \epsilon_{kl}, \quad (2.14)$$

where \mathbf{E}_{ijkl} is the fourth-order elasticity tensor and $\boldsymbol{\varepsilon}_{kl}$ the linear elastic strain tensor. For relatively stiff elastic materials, the elastic strain tensor is approximated as

$$\boldsymbol{\varepsilon}_{kl}(\mathbf{u}) = \frac{1}{2} (\nabla \mathbf{u} + (\nabla \mathbf{u})^T), \quad (2.15)$$

which defines the strain only as a function of the displacement vector [30]. Furthermore, the stress tensor and the strain tensor can be written in vector notation using the symmetry of these tensors. The fourth-order elasticity tensor shows multiple symmetries and can be written as a symmetric 6×6 matrix. With this reshaping, it is possible to reduce Equation 2.14 to

$$\boldsymbol{\sigma} = \mathbf{K} \boldsymbol{\varepsilon}(\mathbf{u}), \quad (2.16)$$

where \mathbf{K} is the elasticity matrix and $\boldsymbol{\varepsilon}$ the strain vector. This representation of the stress vector is further used in Equation 2.13 to define

$$\rho \frac{\partial^2 \mathbf{u}}{\partial t^2} - \nabla \cdot (\mathbf{K} \boldsymbol{\varepsilon}(\mathbf{u})) = \mathbf{F}, \quad (2.17)$$

as the PDE to solve numerically. The same material properties as those used for the analytical solution are used. The elasticity matrix for isotropic materials is defined as

$$\mathbf{K} = \frac{E}{(1 + \nu)(1 - 2\nu)} \begin{bmatrix} 1 - \nu & \nu & \nu & 0 & 0 & 0 \\ \nu & 1 - \nu & \nu & 0 & 0 & 0 \\ \nu & \nu & 1 - \nu & 0 & 0 & 0 \\ 0 & 0 & 0 & \frac{1-2\nu}{2} & 0 & 0 \\ 0 & 0 & 0 & 0 & \frac{1-2\nu}{2} & 0 \\ 0 & 0 & 0 & 0 & 0 & \frac{1-2\nu}{2} \end{bmatrix}, \quad (2.18)$$

with the Young's modulus E and the Poisson's ratio ν as defined in Table 2.1. To solve this PDE, the Finite Element Method (FEM) is a suitable tool. The FEM requires, besides the PDE and material definition, the definition of a geometric structure and a mesh to divide the geometry into small elements. To solve the PDE, initial values, boundary conditions, and environmental constraints are required. These can be deformations of the structure, applied external forces, and artificial layers.

The geometry of the structure is chosen to correspond as closely as possible to the assumptions of the analytical models. All these models assume that the resonator is attached to the semi-infinite substrate, which implies that the energy flow is only directed from the resonator to infinity without any reflection. Therefore, an artificial absorbing layer is used to eliminate the reflections of the faces from the modeled substrate. Frangi et al. [31] demonstrated the effectivity of the concept of the perfectly matched layer (PML) for the evaluation of anchor losses. This layer simulates a material that absorbs waves generated from the deformation of the cantilever, traveling in the normal direction of the interface surface. The tangential component is not affected by the PML. This effect has to be considered in the modeled substrate. If the resonator

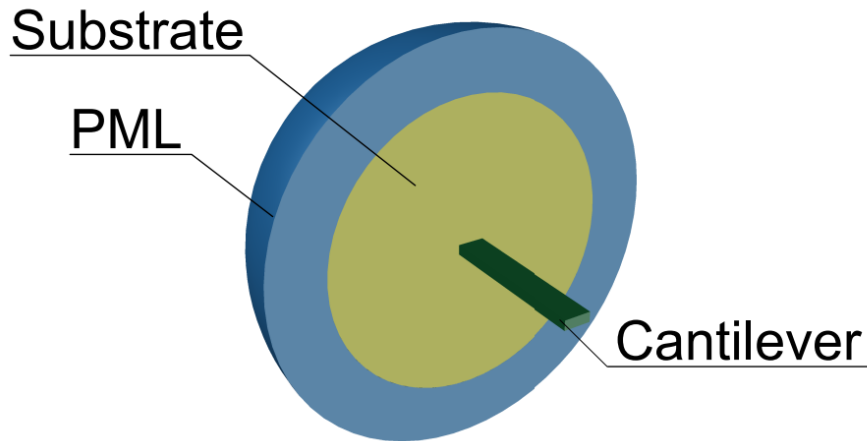


Figure 2.5: Geometry of the half-sphere model

is assumed to be a point source of the mechanical waves, spherical propagation can be expected. For this wave propagation, the interface surface has to be a spherical shell. Therefore, the substrate is modeled as a half sphere. For the assumption of the resonator as a point source, a sufficient distance to the interface shell must be defined to achieve wave propagation in the normal direction. This distance depends significantly on the wavelength λ_{WAVE} , defined as

$$\lambda_{WAVE} = \frac{v_p}{f_{SYSTEM}}, \quad (2.19)$$

where v_p is the phase velocity, and f_{SYSTEM} is the natural frequency of the resonator. For the used material single-crystalline silicon, a phase velocity of sound of 5000 m/s can be assumed [32]. A previous work shows the wavelength times two as a suitable value [21]. Furthermore, the thickness of the PML layer also has to be defined for sufficient absorption. This work also shows that this shell must be at least one wavelength thick. The PML layer thickness is defined as λ_{WAVE} times 1.3, to ensure sufficient absorption. Figure 2.5 shows the defined geometrical structure.

As mentioned, initial values and boundary conditions are also required. The initial values for the displacement and structural velocity fields are defined as zero. The boundary conditions are defined so that all external surfaces of the resonator and the substrate are free to move and can be affected by displacement. Also, no external forces or deformations are applied to the structure. Therefore, the force \mathbf{F} in equation 2.17 is equal to zero. The definition of the mesh size is needed to solve the PDE. The mesh size is strongly related to the precision of the numerical results. The required precision is determined according to the results of the analytical solution. Therefore, the resonant frequency and the Q-factor must first be derived from the numerical solution. The FEM solves the equation 2.17 for the eigenmode displacement vectors \mathbf{u} and its complex eigenvalues λ_{EIGEN} . The eigenmode displacement vectors represent the displacement patterns of the whole geometry. These displacement vectors are normalized to a predefined value and are not related to a physical unit. From each eigenvalue, the

complex eigenfrequency f_{EIGEN} is derived as

$$f_{\text{EIGEN}} = -\frac{\lambda_{\text{EIGEN}}}{2\pi j}, \quad (2.20)$$

with the imaginary unit j . The resonance frequency of the resonating cantilever is the absolute value of the complex eigenfrequency. From this value, the quality factor is derived with

$$Q = \frac{1}{2} \frac{\Re(f_{\text{EIGEN}})}{\Im(f_{\text{EIGEN}})}. \quad (2.21)$$

The model presented is implemented and solved in Comsol Multiphysics. The only missing parameter is the definition of the mesh. This definition is made iteratively by continuously refining the size of the mesh elements.

2.3 Convergence and validation of the FEM model

As mentioned, the accuracy of the FEM results depends on the number and size of the mesh elements. Smaller elements allow finer variations of the physical phenomenon to be recognized. The finer the variations, the better the numerical solution matches the PDE solution. However, the finer the mesh, the longer the execution time of the simulation. Therefore, a trade-off between these two factors is needed. Figure 2.6 shows a series of simulation series with increasing mesh element numbers. The maximum tolerable deviation is defined as 5% compared to the finest mesh result. This deviation is acceptable for analyzing the loss phenomena. The execution time for the corresponding number of elements is also within a tolerable time range for executing the expected amount of simulations. Figure 2.7 shows the selected mesh size.

After defining the mesh, it is started a simulation to compare the FEM results of the defined model with the presented analytical solutions for the natural frequency from equation 2.1 and the anchor losses from equation 2.5. Figure 2.8 shows both results. For lower frequencies, the Q-factors and frequencies fit very well. A significant frequency

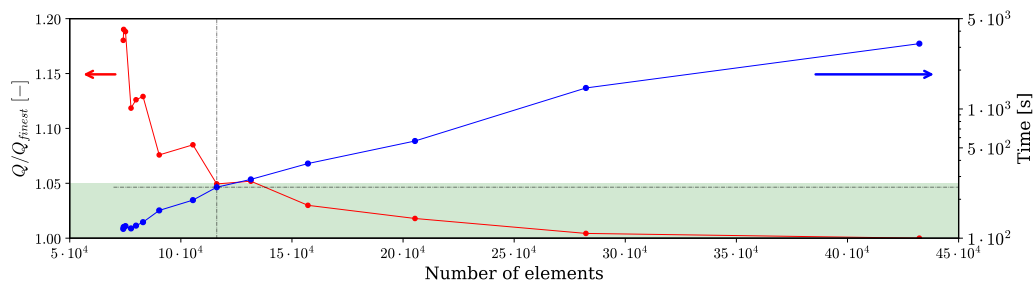


Figure 2.6: Convergence of mesh for the half-sphere model for the first EB mode. The red line is assigned to the left axis and shows the ratio of the Q-factor and the Q-factor with the finest mesh size over the number of mesh elements. The blue line is assigned to the right axis and shows the execution time. The green section marks the acceptable deviation of the ratio.

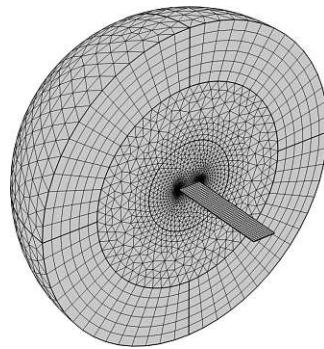


Figure 2.7: Half sphere model with defined mesh from COMSOL Multiphysics

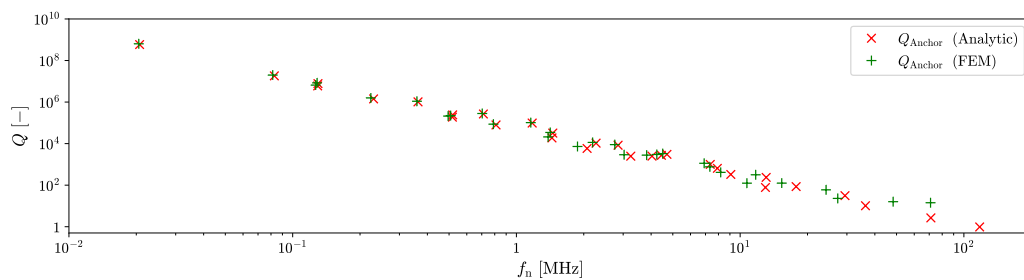


Figure 2.8: Q-factor Q for anchor losses over resonance frequency f_n , in blue from the analytic solution and in red the simulation results of the FEM

shift is visible for frequencies over 1 MHz. Above 10 MHz, the Q-factors deviations are increasing. However, the results overall show the same behavior and demonstrate that the defined model is valid.

2.4 Adaptation of the model to fabricated MEMS resonators

FEM gives the opportunity to fit the model closer to the physical reality of MEMS devices. The cantilever structures in MEMS are mostly attached to the upper edge of the

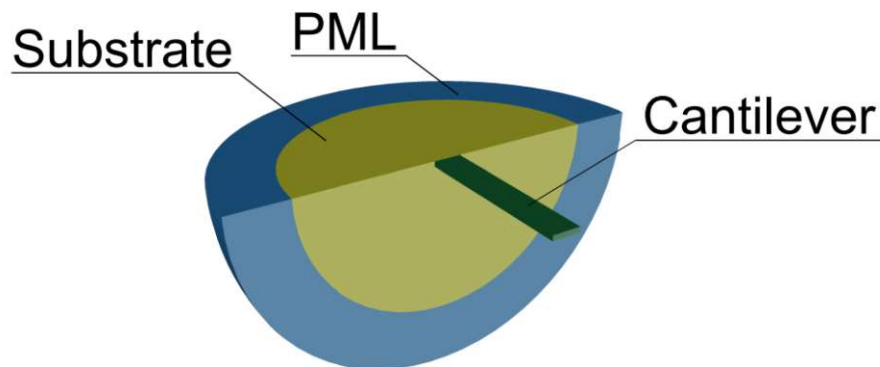


Figure 2.9: Geometry of the quarter-sphere model

substrate. The free upper surface influences the results with this mounting position. Changing the geometry to a quarter sphere. This influence is integrated into the model by changing the geometry to a quarter sphere, shown in Figure 2.9.

Furthermore, it is possible to implement more complex materials. MEMS often consist of anisotropic single-crystalline silicon, which has different elasticity properties depending on the orientation of the crystal. For the representation of anisotropy, the elasticity matrix

$$\mathbf{K} = \begin{bmatrix} 194.5 & 35.7 & 64.1 & 0 & 0 & 0 \\ 35.7 & 194.5 & 64.1 & 0 & 0 & 0 \\ 64.1 & 64.1 & 165.7 & 0 & 0 & 0 \\ 0 & 0 & 0 & 50.9 & 0 & 0 \\ 0 & 0 & 0 & 0 & 79.6 & 0 \\ 0 & 0 & 0 & 0 & 0 & 79.6 \end{bmatrix} \text{ GPa}, \quad (2.22)$$

as described by Hopcroft et al. for the $[110]$, $[\bar{1}10]$, $[001]$ orientation is used [33]. All other relevant properties are taken as defined in Table 2.1.

Figure 2.10 shows the results for the half-sphere model with isotropic silicon in green and the quarter-sphere model with anisotropic silicon in blue. The quarter-sphere model has a slightly lower Q-factor. For the anisotropic material, the elasticity matrix changes only slightly in the longitudinal direction of the resonator. Therefore, it is not expected to impact EB mode shapes significantly. It is more probable that the free upper surface of this model influences the Q-factor. For the half-sphere model, the waves are propagated in the upper and lower part of the substrate. In the quarter sphere model, the upper surface reflects the wave and causes interference with the directly emitted waves of the resonator.

For frequencies below 2 MHz, the gap between the related Q-factors is relatively stable, and the resonance frequencies match well. There is no clear pattern for the differences between the values at higher frequencies. In this frequency region, the slightly different elasticity matrix may also influence both values.

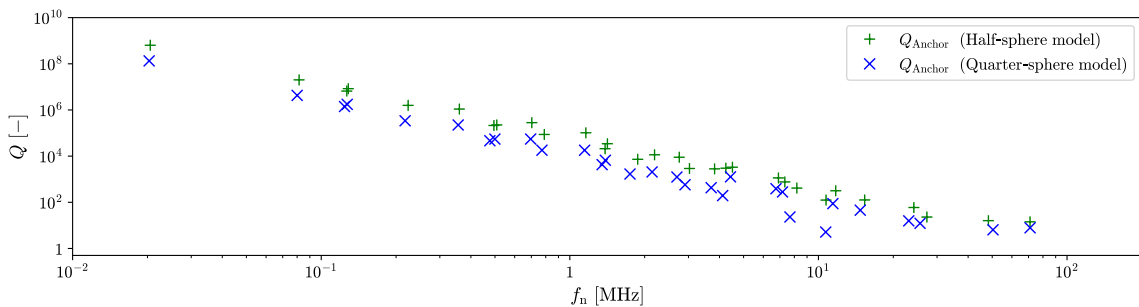


Figure 2.10: The Q-factor for anchor losses over the resonance frequency of the half-sphere and the quarter-sphere model

2.5 Conclusions

The analytical solutions for the most important loss sources are shown to identify the dominant damping mechanism. For EB modes, the anchor losses decrease sharply and dominate above a resonance frequency of 3 MHz. For resonators with high Q-factors, anchor losses above 10^3 and natural frequencies higher than 3 MHz are desired. The lack of solutions for anchor losses of higher-order-mode shapes makes it necessary to define a physical model of the plate resonator. The theory of linear elasticity is used to model the material, and a half-sphere geometry is selected to model the substrate. Then, the model is implemented in COMSOL Multiphysics, and a proper mesh is defined. Furthermore, the convergence of the model is shown. The completely defined model is successfully validated, referring to the analytical equations. The last step is to adapt the model to real MEMS devices. Therefore, the geometry is changed to a quarter sphere and the material to anisotropic silicon. Subsequently, this new model is validated successfully with the isotropic half-sphere model.

3 Vibrational modes and anchor losses on non-slender resonators

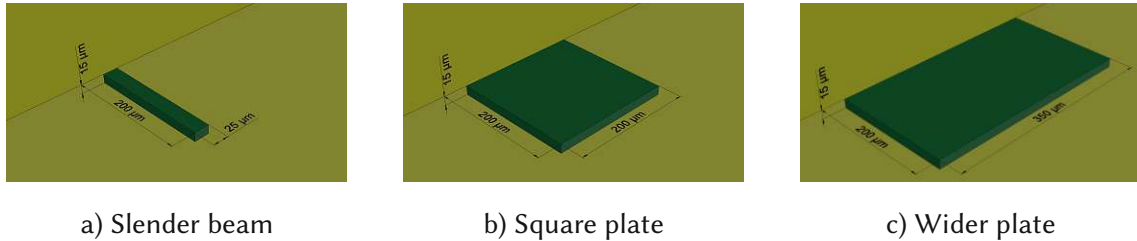


Figure 3.1: Geometries of the evaluated cantilevers

The model presented in section 2.4 is now used to evaluate three different geometries and analyze the resulting mode shapes in relation to anchor losses. Furthermore, the energy flow in the substrate generated by the anchor losses is evaluated to identify the major flow directions. Figure 3.1 shows the resonator geometries of the models, which are solved using COMSOL Multiphysics for the approximately first 30 eigenmodes. To distinguish the resonator modes from the so-called substrate modes, a quality factor of 5 is defined as the lower limit. First, the slender beam, shown in a), is analyzed as a reference geometry. This beam is 200 μm long, 25 μm wide and 15 μm thick. Then, a square resonator, shown in b), is evaluated. The length and thickness are taken from the slender beam so that the results can be compared only in terms of width. Finally, a wide plate, shown in c), is analyzed. This plate is 350 μm wide. The length and thickness are also kept constant in this case. Table 3.1 summarizes the used parameters for the FEM simulations.

<i>Substrate model:</i>	Quarter sphere
<i>Material:</i>	Anisotropic single-crystalline silicon
<i>Orientation:</i>	$[110]$, $[\bar{1}10]$, $[001]$
<i>Resonator length:</i>	$l = 200 \mu\text{m}$
<i>Resonator width:</i>	$w = \{25, 200, 350\} \mu\text{m}$
<i>Resonator thickness:</i>	$h = 15 \mu\text{m}$

Table 3.1: Parameters of the FEM simulations

Before starting with the evaluation of these geometries, the relevant mode types for the free-clamped resonator are presented briefly. Figure 3.2 shows examples of these mode types. Figure a) shows the 1st Euler-Bernoulli (EB) mode shape. This mode type has only a displacement in an out-of-plane (OOP) direction, and the cross-sections of the beam are not deformed. Figure b) shows a further type of OOP mode, the so-called torsional mode. In contrast to the EB modes, the cross-section is indeed changed and affected by a rotary movement. The subfigures c) and d) show the higher-order OOP (HO-OOP) mode shapes. The base type for HO-OOP mode shapes are the roof tile-shaped (RTS) modes, shown in c). Figure d) shows the example for the more complex

HO-OOP mode shapes. This type is formed from the superposition of HO-EB modes and RTS modes. In addition to the OOP modes, there are also in-plane (IP) modes divided into lateral (lat.) modes in e), extensional (ext.) modes in f), and the so-called bulk modes in g) and h).

3.1 The slender beam resonator

First, is executed a simulation of a 200 μm long, 25 μm wide, and 15 μm thick resonator. Before investigating natural frequencies and Q-factors, the types of eigenmodes for this geometry are analyzed with a focus on the displacement patterns of the resonator and the anchor region.

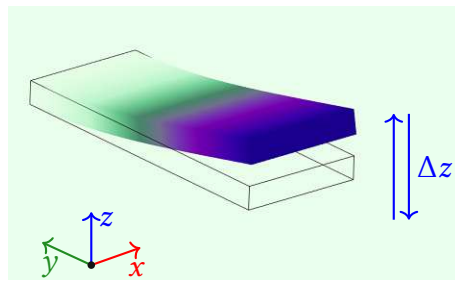
3.1.1 Analysis of the displacement patterns

The appearing mode shapes can be divided into two major classes referring to the main displacement direction, the out-of-plane mode types, and the in-plane mode types. In the OOP direction, Euler-Bernoulli mode shapes and torsional mode shapes are found. For the IP direction, EB mode shapes with lateral bending and extensional mode shapes occur.

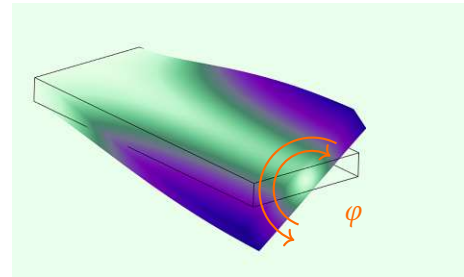
The first example in Figure 3.3 a) shows the 5th OOP EB mode shape. The white areas do not exhibit any displacement. In the center of these areas are located the so-called nodal lines. The areas of higher displacement are colored in blue and oscillate in time between positive and negative deflection. In the image, the displacement is greatly magnified. The real peak deformation in the darkest areas is in the order of a few nanometers, as experiments have shown [21]. The beam length itself does not vary significantly compared to the OOP displacement. For OOP EB mode shapes, all nodal lines are parallel to the substrate edge along the whole width and half height of the beam. The count of nodal lines refers to the order of the mode shape. In this example, four nodal lines are on the cantilever, and a fifth is in the anchor to the substrate. At the upper surface of the substrate, a slight deformation is visible. This area is the so-called anchor region. This part of the substrate is affected directly by the surface acoustic wave (SAW) and the bulk acoustic waves (BAW) radiated from the cantilever. SAWs propagate the dissipated energy from the resonator at the upper and front surfaces to the PML surfaces. The energy of the BAWs is diffused in the substrate volume and also dissipated in the PML.

An example of the second OOP mode type is shown in Figure 3.3 b), the 3rd torsional mode shape. The nodal lines are visible in white, three parallel to the substrate edge and one along the beam. This longitudinal nodal line is located in the center of the beam cross-section and is the rotary axis of the torsional movement. The parallel nodal lines are extended to the whole beam section. The anchor region is affected by a deformation, mostly at the lateral beam edges in opposite directions.

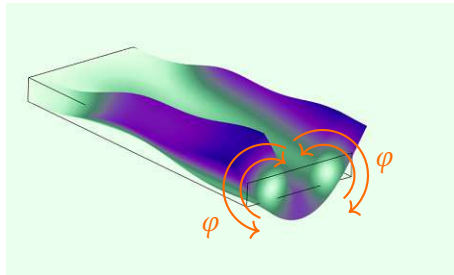
For the IP mode types, as an example, is shown in Figure 3.4 a) the 5th lateral EB mode shape. The properties of this mode type are essentially the same as those of the OOP EB, with the direction of deflection changed to lateral. However, the direction



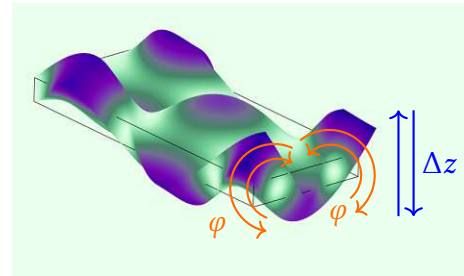
a) 1st EB mode shape. Up and down bending only in z -direction.



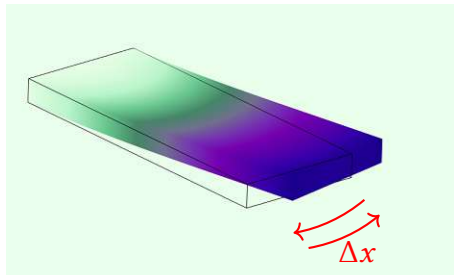
b) 1st torsional modes shape. Rotary motion along the y -axis.



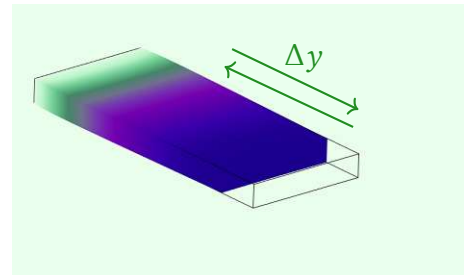
c) 1st RTS mode. Two contrary rotary motions in parallel to the y -axis.



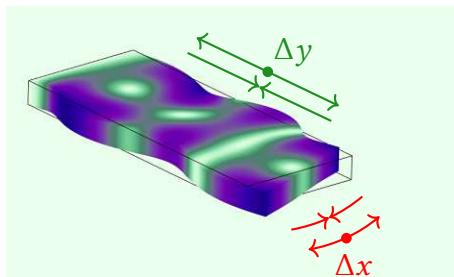
d) HO-OOP mode shape. Superposition of the 3rd EB mode shape and the 1st RTS mode.



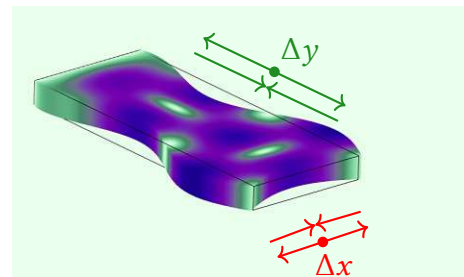
e) 1st lateral EB mode shape. Left and right bending only in x -direction.



f) 1st extensional mode shape. Compression and elongation in y -direction.



g) Bulk mode. Superposition of lateral and extensional mode shapes.



h) Bulk mode. Compression and elongation in x - and y -directions.

Figure 3.2: Examples for the different mode types on cantilever resonators

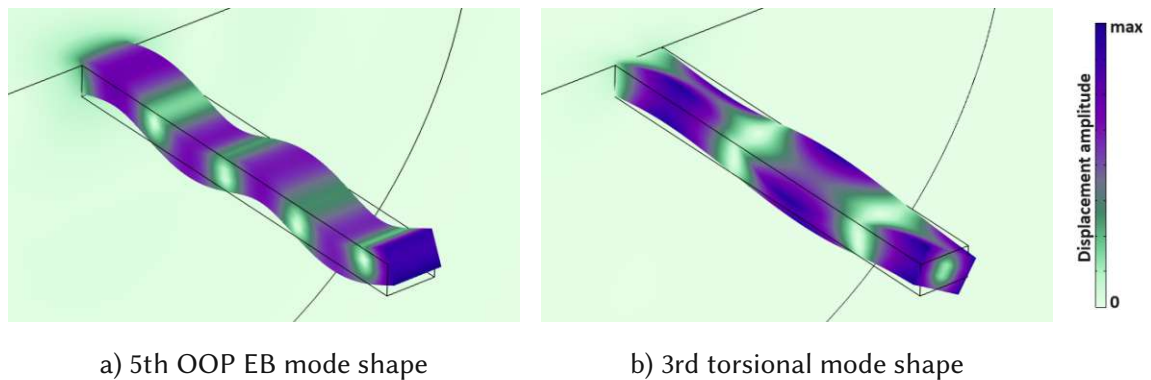


Figure 3.3: Types of out-of-plane mode shape on slender beam resonator.

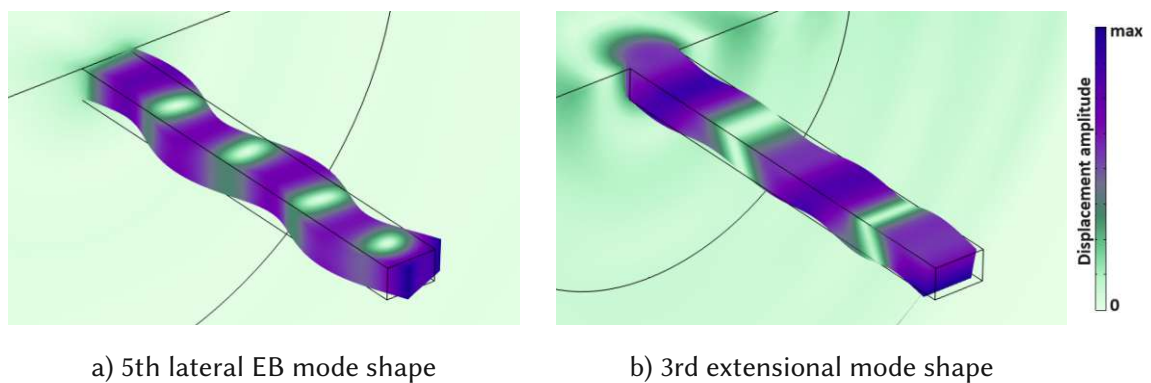


Figure 3.4: Types of in-plane mode shape on slender beam resonator.

of force applied to the substrate is different. The upper surface shows no significant displacement. The lateral beam edges are causing an oscillating stretching on the front substrate plane.

The last example is the 3rd extensional mode shape, depicted in Figure 3.4 b). In this case, the length of the beam is changed periodically, with stretching and compressing forces acting alternately. The direction of this force is strictly longitudinal and acts uniformly on the entire beam cross-section. Therefore, nodal surfaces are present in this mode type rather than lines. This planar cyclic force acts on the substrate through the anchor. The surface of the substrate at the anchor is also significantly deformed.

3.1.2 Analysis of the anchor losses

Figure 3.5 shows the simulation results, separated by the deflection planes. On the y-axis, the Q-factor is plotted on a logarithmic scale, and on the x-axis, the natural frequency is plotted on a linear scale. The natural frequency range to find the 30 eigenmodes is relatively large. It starts with the 1st OOP EB mode shape at around 0.5 MHz and reaches more than 80 MHz for the 10th lateral mode shape. Figure 3.5 a) shows that for the OOP mode types EB and torsional mode shapes are found. The first EB mode has

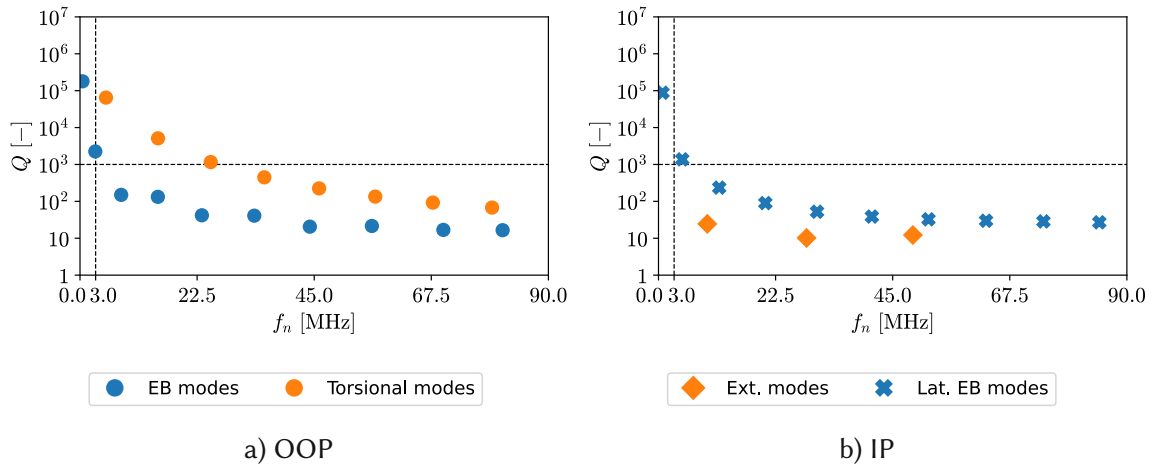


Figure 3.5: Occurring mode shapes for the slender beam resonator, showing the quality factor Q over the natural frequency f_n . The dashed lines delimit the region of promising mode shapes with resonant frequencies above 3 MHz and Q -factor above 10^3 .

a high quality factor of around $2 \cdot 10^5$, but it decreases rapidly afterward. From the 3rd EB mode on, with the resonance frequency of around 8 MHz, all modes have Q -factors below 200. The behavior for the torsional mode shapes is slightly better. They also start very high from around $6.5 \cdot 10^4$ and decrease not so sharply as EB modes. They drop under 10^3 around an eigenfrequency of 25 MHz and are all above 100, besides the last highest orders. Figure 3.5 b) shows the identified in-plane mode shapes. For lateral EB mode shapes, the frequencies and the Q -factors are very similar to those of the OOP EB modes. These similar values are because of the small difference between beam width and thickness. The extensional mode shapes are further apart in terms of frequency than the other mode types. However, all of them have low Q -factors below 25.

From these results, only the first three torsional mode shapes and the second lateral EB mode are in the region with the potential to reduce the anchor losses with higher orders. However, no HO-OOP mode shape appeared in this large range of frequency. Therefore, non-slender geometries are mandatory for these modes.

3.1.3 Analysis of the mechanical energy flux

To better understand the behavior of anchor losses, its effect on the substrate is investigated. As described in Equation 1.1, the Q -factor is related to periodic energy dissipation. The anchor losses induce a mechanical energy flux from the cantilever into the substrate. This mechanical energy flux vector \mathbf{I} in the time domain is defined as

$$\mathbf{I}_{mech}(t) = -\sigma_{ij} \cdot \mathbf{v}(t), \quad (3.1)$$

with t the time, σ_{ij} the stress tensor and \mathbf{v} the velocity vector. The minus sign is defined by the direction convention from the energy source, the resonator, to the load, the PML. For the FEM calculations is used the frequency domain. The energy flux in the complex

form is obtained from

$$\mathbf{I}_{mech}(j\omega) = -\sigma_{ij} \cdot \mathbf{v}^*(j\omega), \quad (3.2)$$

with j the imaginary unit, ω the angular frequency, and $*$ indicates the complex conjugate form. The average mechanical energy flux is derived as

$$\mathbf{I}_{mech,avg} = \frac{1}{2} \Re(-\sigma_{ij} \cdot \mathbf{v}^*(j\omega)). \quad (3.3)$$

Only the normal component of the energy flux gives information about the effective flow from the source to the load. Therefore, it is necessary to define the normal direction of the flux. In this case, it is the direction in which the energy is propagated from the resonator to the PML layer. For simplification, the resonator is assumed to be a point source in the sphere's center. Therefore, the normal direction is defined in this model as the radial component of the energy flux and is obtained as

$$I_{norm}(\mathcal{P}) = \mathbf{I} \cdot \frac{\mathbf{x}(\mathcal{P})}{|\mathbf{x}(\mathcal{P})|}, \quad (3.4)$$

with \mathbf{x} the radial vector from origin \mathcal{O} at the center of the sphere to a specific point \mathcal{P} and $|\cdot|$ means the Euclidean norm of a vector. Because of the simplification, the values only become valid above a certain distance from the resonator, for which one wavelength is assumed.

The radial component is shown at the surfaces of a substrate section to visualize the energy flux. The section depicted in Figure 3.6 is defined as the half of the substrate, from which an inner sphere with a radius of one wavelength is cut out. From the symmetry of the structure, it can be assumed that the same radial behavior of the energy flux is present in both halves of the substrate.

Figure 3.7 a) shows the energy flux for the 1st OOP EB mode shape. The major flow directions are illustrated in the figure with the arrows A to C . The energy for this mode type is mainly propagated on the surfaces. The highest densities are well distributed on the upper surface in the direction A and in the direction B . A smaller portion is also

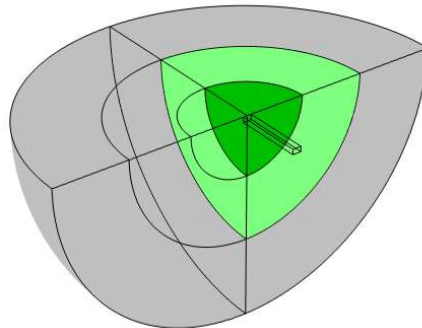


Figure 3.6: Quarter sphere model: The section of the substrate evaluated for the mechanical energy flow is marked in green.

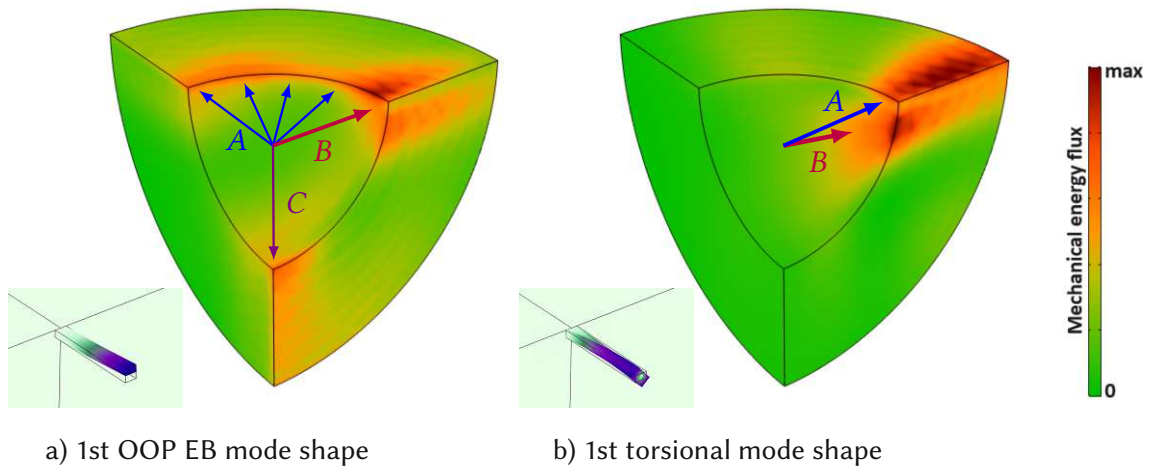


Figure 3.7: Radial mechanical energy flux for out-of-plane modes.

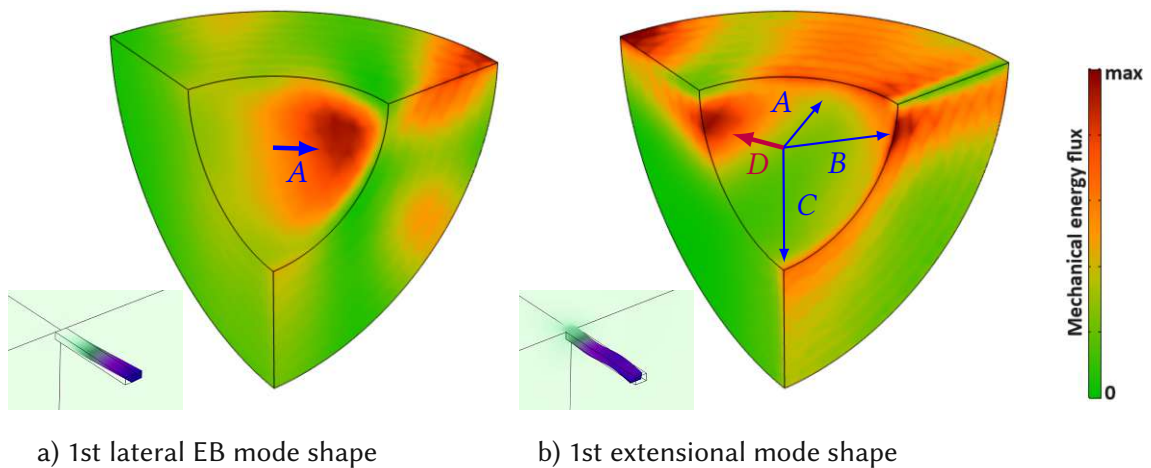


Figure 3.8: Radial mechanical energy flux for in-plane modes.

radiated in the direction C . Inside the substrate, no significant flux is present.

Figure 3.7 b) shows that for the 1st torsional mode shape, the energy flux is highly concentrated on the upper surface in the direction A . In the same direction, a significant portion of energy also flows deeper into the substrate, marked with B . The other parts of the substrate are not affected by any flux.

The energy flux for the 1st lateral EB mode shape, depicted in Figure 3.8 a), is propagated inside the bulk in the direction A . On the outer surfaces, no significant flow is visible.

In Figure 3.8 b) is shown that for the 1st extensional mode shape, the energy flux is more concentrated on the upper surface in the direction A , and on the front surface mainly in the direction B and C . A significant flow is also visible deeper inside the substrate in the direction D .

3.2 A square plate resonator

As the first step to investigate non-slender geometries, a square plate with dimensions $200\ \mu\text{m}$ long, $200\ \mu\text{m}$ wide, and $15\ \mu\text{m}$ thick is simulated. Different higher-order mode types are found in both displacement planes in this geometry. In the beginning, the individual aspects of these displacement patterns are described. Further, the resonance frequency and quality factor results are presented, and the mechanical energy flux is discussed.

3.2.1 Analysis of higher-order displacement patterns

Figure 3.9 a) shows an example of a HO-OOP mode shape. To uniquely identify HO-OOP mode shapes, the naming convention presented by Leissa is used subsequently [34]. It is based on the nodal line count. The directions of the nodal lines are illustrated in the figure. The nodal line parallel to the anchor is shown in red, and in blue, the longitudinal nodal line along the plate length is shown. All nodal lines of the resonator are numbered according to their direction. The naming format is defined as $n_y : n_x$. The first number, n_y , refers to the parallel nodal lines, and the second number, n_x , refers to the longitudinal nodal lines. The mode shape shown as an example is identified as the 3:4 mode. This notation works well also for Euler-Bernoulli mode shapes, described as $n_y:0$, and torsional mode shapes as $n_y:1$. For these modes, the mode order is equal to n_y . The first order of HO-OOP mode types is called roof tile-shaped modes and is defined as $1:n_x$, with $n_x > 1$. All other HO-OOP mode shapes are defined from the superposition of EB and RTS modes. To use the naming convention also for the IP mode shapes, there the name abbreviation is added. For lateral mode shapes, it is lat. $n_y:0$; and for extensional mode shapes, ext. $n_y:0$.

A new mode type appeared for the in-plane mode shapes, the bulk mode. An example is depicted in Figure 3.9 b). This mode type can show stretching, compressing, and lateral bending waves in both in-plane directions. The concept from Leissa is not applicable for such mode shapes, as they do not have strict parallel or longitudinal nodal

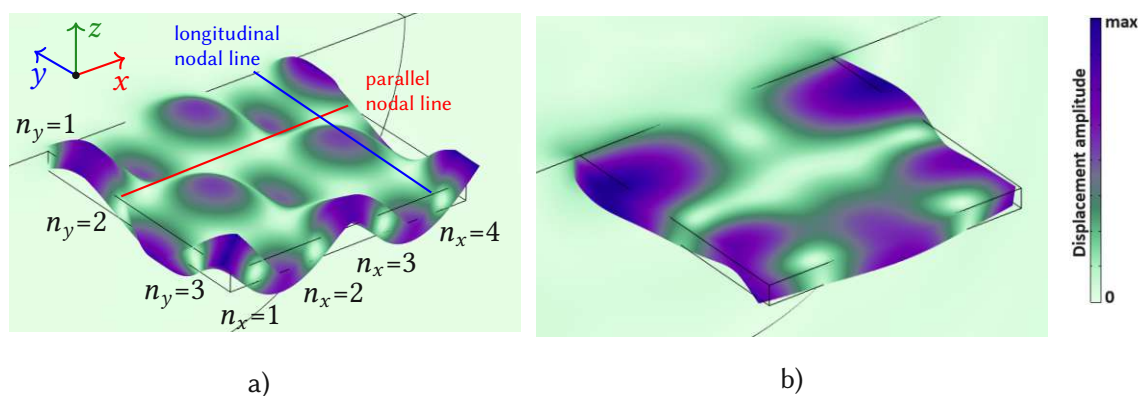


Figure 3.9: New appearing mode shapes for non-slender resonators. In a) the 3:4 HO-OOP mode shape and in b) an IP bulk mode.

lines. Moreover, node points, as shown in the example, are also possible. As shown later in this section, the resulting Q-factors are out of scope to improve anchor losses. Therefore, bulk modes are not classified in detail and are called simply IP mode shapes.

3.2.2 Analysis of the anchor losses

Figure 3.10 shows the first 30 eigenmodes found with a Q-factor above 5.

For the OOP mode shapes in Figure 3.10 a), it is visible that besides the EB and torsional mode shapes are appearing many HO-OOP mode shapes. With this wider structure, the natural frequency range for the amount of found eigenmodes decreases and reaches only 30 MHz. The comparison with the result from the slender beam resonator in Figure 3.5 a) shows that the eigenfrequency for EB modes remains nearly constant. This behavior matches the prediction from the analytic solution in Equation 2.1. The resonance frequencies for torsional modes are significantly lower compared to the slender beam, e.g., by a factor of 5 for the 1:1 and a factor of 2 for the 5:1 mode. The quality factor of EB and torsional mode shapes is significantly lower for the quadratic plate, besides the 1st torsional mode. The HO-OOP mode shapes have mostly Q-factors above 10^3 and are very well distributed in the frequency range above 3 MHz. Not less than ten promising mode shapes are identified within this region.

In Figure 3.10 b) are shown the the IP mode shapes. The natural frequency of the lateral EB modes is shifted to higher frequencies, and their quality factors dropped drastically, compared to Figure 3.5 b). Only one extensional mode is found, approximately constant in frequency, but with a very low Q-factor of around 9. Most bulk modes have poor quality factors below 100. Therefore, IP mode shapes do not show any potential to improve anchor losses.

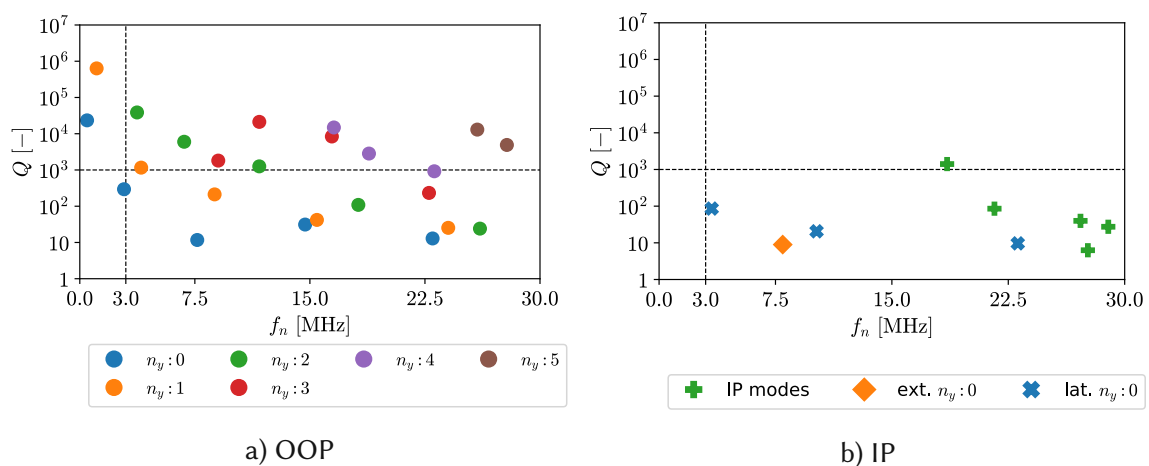


Figure 3.10: Occurring mode shapes for the quadratic plate resonator, showing the quality factor Q over the natural frequency f_n . The dashed lines delimit the region of promising mode shapes with resonant frequencies above 3 MHz and Q-factor above 10^3 .

3.2.3 Analysis of the mechanical energy flux

Analyzing the mechanical energy flux in Figure 3.11 a) for the 1st OOP EB mode shows the same directions as for the slender geometry. The main direction is still lateral and also on the upper surface. A significant flow is present on the front surface, only below the resonator. Figure 3.11 b) shows that only a very small section around the substrate edge energy is propagated. Compared to Figure 3.7 b) the energy is much more concentrated at the surfaces and no more inside the bulk.

Figure 3.12 a) shows for the 1st lateral EB mode shape, that the energy flows mostly inside the substrate and on the upper surface in direction A. For the 1st extensional mode shape is shown in Figure 3.12 b) that the energy flux is propagated mainly on the front surface in direction A and B. A smaller portion is radiated in the bulk in the direction C.

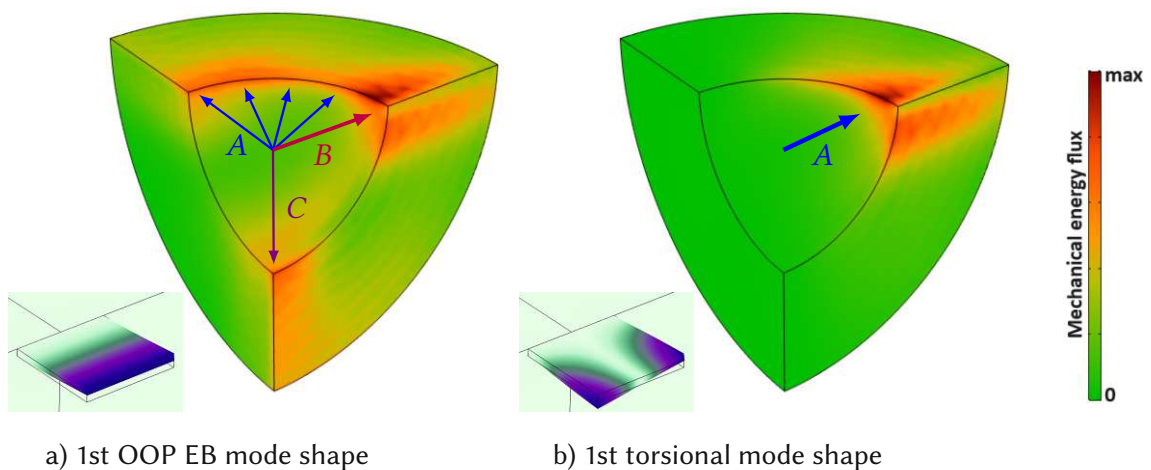


Figure 3.11: Radial mechanical energy flux for out-of-plane modes.

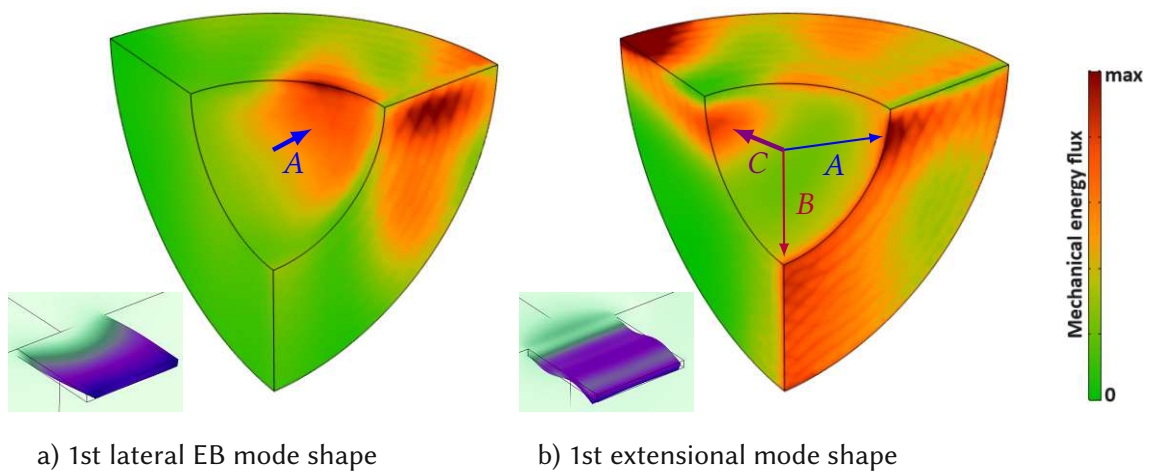


Figure 3.12: Radial mechanical energy flux for in-plane modes

3.3 The wider rectangular plate resonator

In this section, a wider rectangular plate is analyzed. The length and thickness of the rectangular plate were not changed to compare the results with the previously shown square plate. The dimensions are selected as 200 μm long, 350 μm wide, and 15 μm thick. Many more HO-OOP mode shapes are identified with promising Q-factors from this simulation. No new mode types are identified for this wider geometry.

3.3.1 Analysis of the anchor losses

Figure 3.13 shows the appearing mode shapes. In a) for the OOP mode shapes, the order of founded HO-OOP modes increased compared to the quadratic plate. The highest appearing resonance frequency decreased and is only slightly above 18 MHz, while the lowest eigenfrequencies are still remaining below 1 MHz. The eigenfrequency for EB mode shapes does not change between the three different widths, as expected from the shown analytic solution (EQ. 2.4). The resonance frequency does not change much for torsional mode shapes from square to the wider plate. Compared to the slender beam, it is decreased a lot. The HO-OOP mode shapes are shifted downwards in frequency, but not all mode types in the same way. The EB and torsional are once more affected by decreasing quality factors. However, more than 12 HO-OOP mode shapes have promising Q-factor above 10^3 . The RTS modes 1:3 and 1:5 show lower Q-factors as their related second-order mode shapes. The same behavior is observed also on the square plate for the 1:3 mode. The expectation that the RTS modes always have the highest quality factor can not be confirmed following these results. Further investigations are needed to understand the underlying loss mechanisms.

Figure b) shows that only a few modes were found, all with poor Q-factors below 100 for the IP mode shapes.

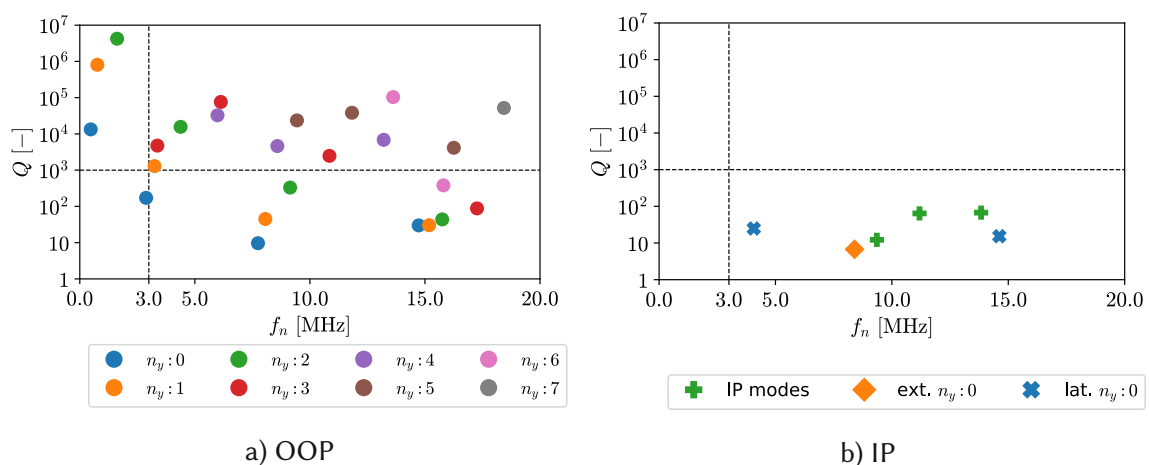


Figure 3.13: Occurring mode shapes for the wider plate resonator, showing the quality factor Q over the natural frequency f_n . The dashed lines delimit the region of promising mode shapes with resonant frequencies above 3 MHz and Q-factor above 10^3 .

3.3.2 Analysis of the mechanical energy flux

Figure 3.14 a) shows the same directions and intensities as for the slender and the square geometry. This similar energy flux leads to the conclusion that the width does not significantly affect the energy flux for this mode shape. Similar behavior is also visible for the 1st torsional mode shape in Figure 3.14 b). Also, on the wider plate, the energy is propagated along the substrate edge, mainly on the upper and front surfaces.

Figure 3.15 a) shows the energy flux for the 1st lateral EB mode shape. The main flow is in the direction of *A* inside the substrate and also on the upper surface. This behavior is very similar to the quadratic plate. For the 1st extensional mode shape in Figure 3.15 b), the energy flux is mainly present on the front surface concentrated below the resonator in direction *A*. A relatively small portion is propagated inside the substrate in direction *B*. The mechanical energy flux for this mode is very similar for the slender beam and the quadratic plate, but the lateral flow is no longer present for the wider structure.

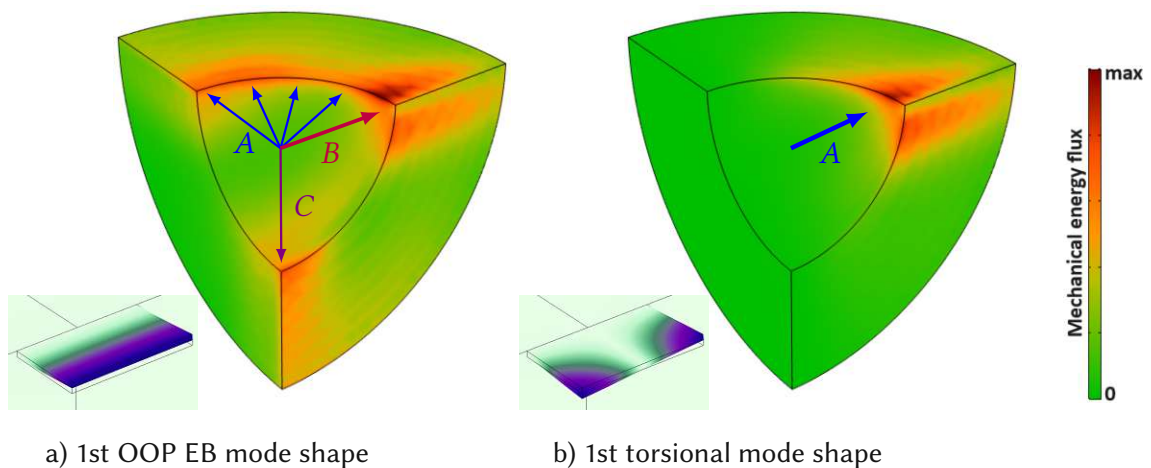


Figure 3.14: Radial mechanical energy flux for out-of-plane modes.

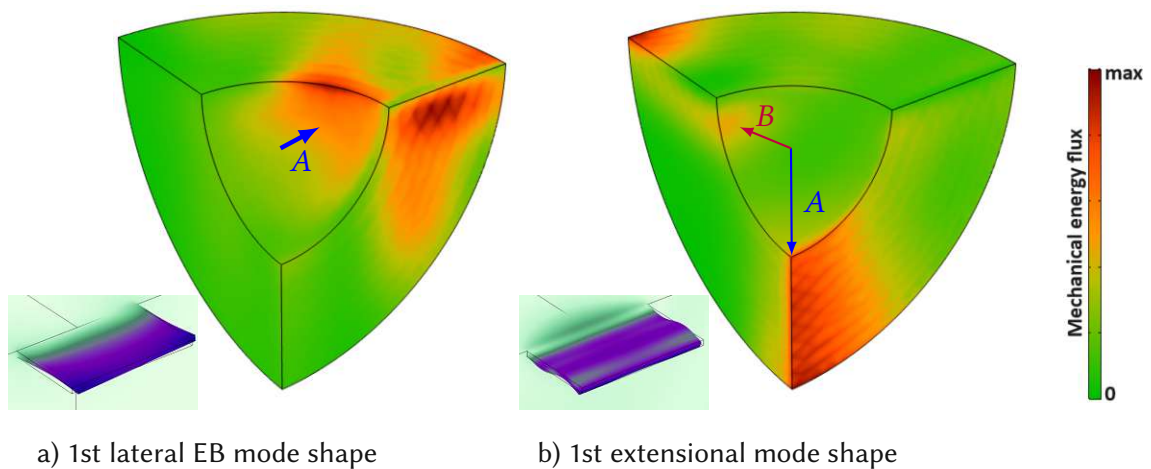


Figure 3.15: Radial mechanical energy flux for in-plane modes.

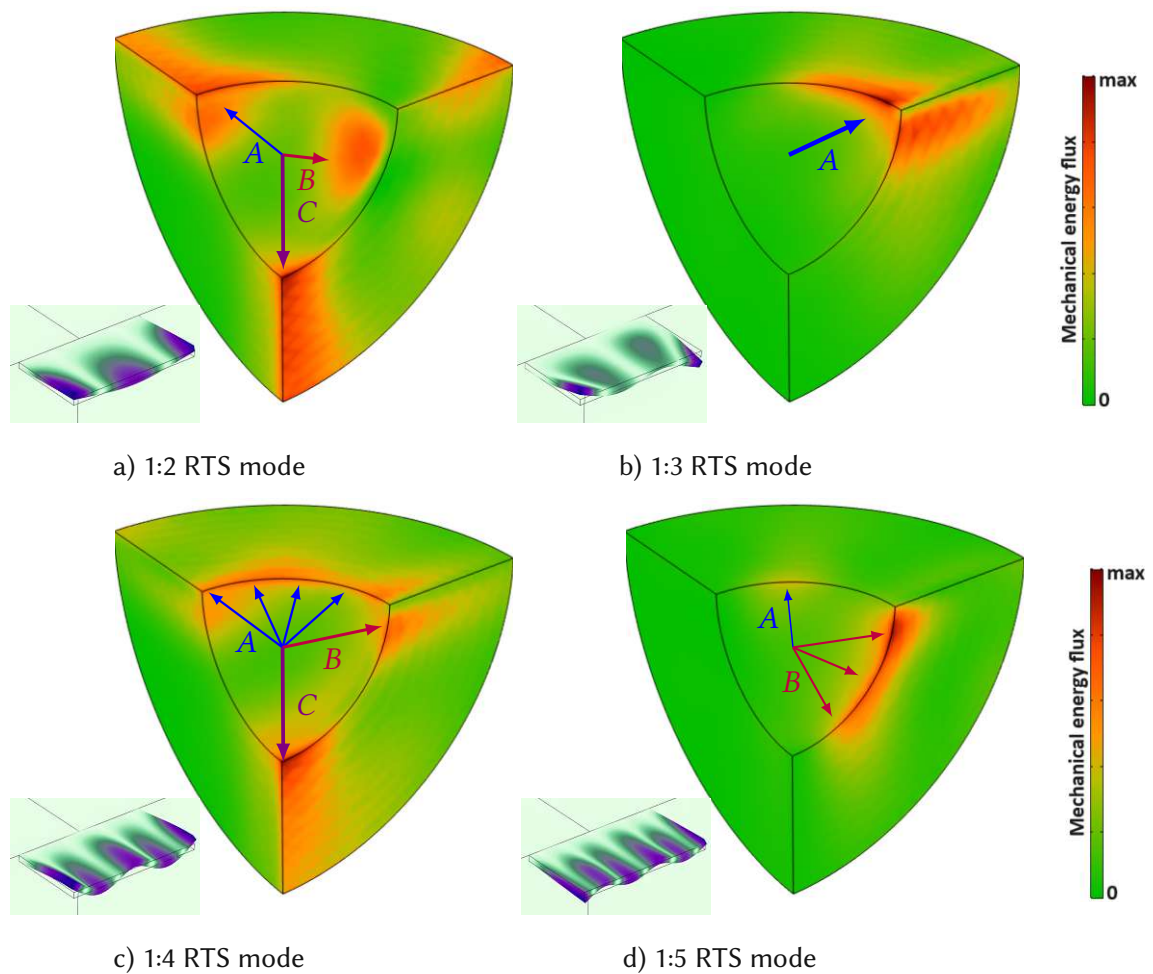


Figure 3.16: Radial mechanical energy flux for RTS modes.

Figure 3.16 shows the mechanical energy flux for the first four RTS modes. For the 1:2 RTS mode, shown in a), the major energy flow is in direction *C* on the front surface. Another significant flow is visible in direction *B* inside the substrate. On the upper surface, a minor flow is in direction *A*. In Figure b), for the 1:3 RTS mode, only one energy flux direction is visible. This flux is in direction *A* on the front and upper surface around the substrate edge. The 1:4 mode shows a main energy flux in the direction *C* below the resonator. Significant energy flows are also visible on the upper surface, in the direction *A* and along the substrate edge in *B*. Lastly, the 1:5 RTS mode shows, besides a small energy flux in direction *A*, a dominant flow on the front face in the direction *B*.

3.4 Conclusions

The square and the wider plate results show that these geometries are well suited for HO-OOP mode shapes. Most of these mode have Q-factors above 10^3 with resonance frequencies above 3 MHz. The RTS modes tend to have the highest quality factors, but

not always. Some of these mode shapes have significantly lower Q-factor. However, they are very promising for high quality factor applications. The next chapter investigates the underlying mechanisms for the inconsistent Q-factor behavior.

4 Avoided crossing and "Q-drop" crossing in cantilevered plates

In the previous chapter, the mode shapes on different widths are analyzed. Many HO-OOP mode shapes are found on non-slender resonators. The torsional and x:2 modes show a descending Q-factor for higher-order mode shapes. This trend is also expected for the other HO-OOP mode shapes. However, the x:3 modes are evolving differently. The 1:3 shows a significantly lower Q-factor than the 2:3. No explanation is found for this different Q-factor behavior compared to the 1:2 mode. Other mode shapes also do not show a distinct, descending, or ascending order in the Q-factor. In order to identify the mechanisms behind the relationship between Q-factor and mode order in different plate resonators, a simulation sweep is performed. For the sweep simulation are defined different plate resonators with an increasing width from 250 μm to 500 μm , with an increase of 2 μm . Figure 4.1 shows the limiting geometries for the sweep. All used parameters for the simulation are defined in Table 4.1.

<i>Substrate model:</i>	Quarter sphere
<i>Material:</i>	Anisotropic single-crystalline silicon
<i>Orientation:</i>	[110], $[\bar{1}10]$, [001]
<i>Resonator length:</i>	$l = 200 \mu\text{m}$
<i>Resonator width:</i>	$w = \{250; 252; 254; \dots 500\} \mu\text{m}$
<i>Resonator thickness:</i>	$h = 15 \mu\text{m}$
<i>Maximum resonance frequency:</i>	$f_{n,max} = 10 \text{ MHz}$
<i>Minimum Q-factor:</i>	$Q_{min} = 5$

Table 4.1: Parameters of the FEM simulations

From the simulation results, over 2000 eigenmodes with a Q-factor over five on the different plate widths are identified. The identification of the mode shapes is started with RTS modes. Figure 4.2 shows the simulation results for the natural frequency over the width. All identified RTS modes are highlighted in color, and so far, the uniden-

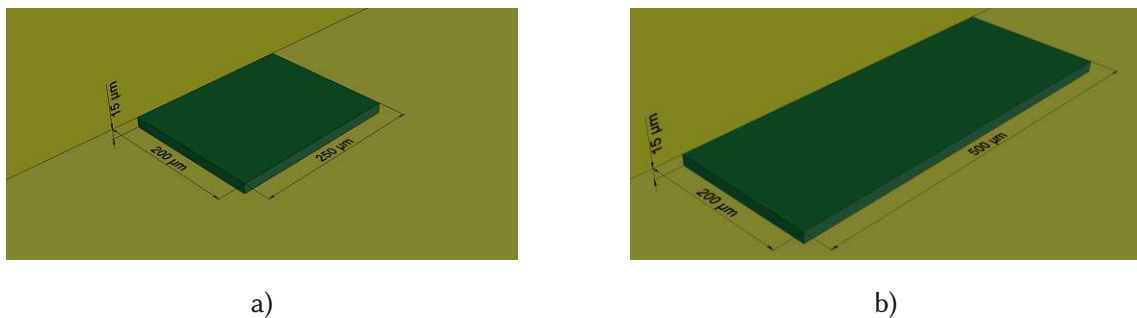


Figure 4.1: Examples of the analyzed plate widths. In a) the smallest plate with 250 μm and in b) the widest plate with 500 μm

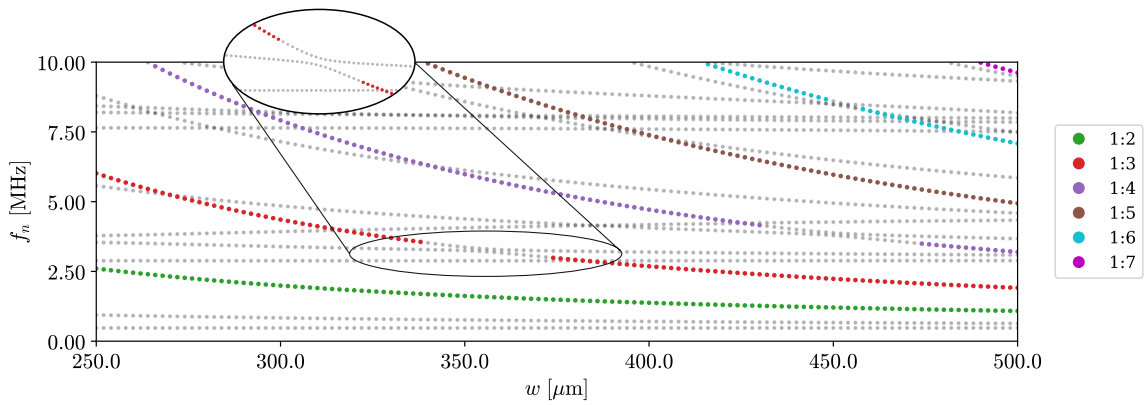


Figure 4.2: Result of the simulation sweep: The resonance frequencies f_n over the plate width w . Highlighted are all identified RTS modes. The other modes are in gray in the background. For some widths, the 1:3, 1:4, and 1:6 mode shapes cannot be identified. For the 1:3 mode, a zoom is shown in this area. The resonance frequencies in grey between the identified red dots show a repulsive trend.

tified mode shapes are gray in the background. Some of these RTS modes cannot be identified at each plate width. For the 1:3 mode, a zoom is shown in this area. In this zoomed region, it is visible that the resonance frequencies in gray do not build a connection between the red dots. The paths of natural frequency are repelling each other. This repulsive trend is also identified for other paths. Figure 4.3 shows the simulation result, sorted to follow the identified progression of the natural frequencies. In all areas where the mode shapes are not possible to categorize, this repulsive behavior in resonance frequency is found. Between the width where the mode shape disappears on one path and the width where it reappears on the other, the mode shapes do not show a displacement pattern, which can be described with the Leissa notation. Therefore, the following section presents a mathematical method to classify the displacement patterns in this transition zone.

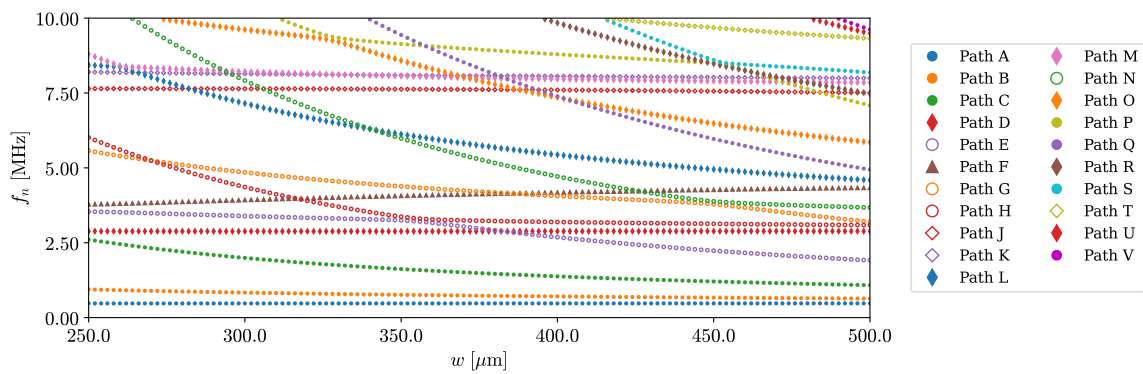


Figure 4.3: Results of the simulation with increasing width. The natural frequencies are grouped by paths from A to V ordered by ascending frequency.

4.1 Fourier transformation based mode shape identification

To overcome the not classifiable displacement patterns is presented an analytical method to detect automatically all mode shapes. The input data is defined as the specific displacement pattern from a resonance frequency of a specific plate width. No additional information is needed. The method is developed using the script language *Python*. This language was selected because of the libraries offered for scientific computing, data analysis, and visualizations. The *Python* library *NumPy* is used for numerical computations, which offers a broad range of mathematical functions and efficient array operations.

The displacement data to evaluate is obtained from the FEM solver in *Comsol Multiphysics*. The FEM solves the defined problem in the spatial frequency domain. Therefore, the displacement field is complex-valued. The displacement field is represented from the displacement vector $\mathbf{u} = (u_x, u_y, u_z)$. All vectors \mathbf{u} of a particular displacement pattern are normalized to a predefined value in relation to the highest absolute value that occurs and does not refer to a physical unit. Because the simulated plates are thin, the displacement field along the z -axis does not vary significantly. Therefore, reducing data from the 3D structure to a 2D surface is possible. The surface is defined in the x - y plane at half thickness on the cantilever. Figure 4.4 shows the defined surface. The relevant steps to the export are shown in Appendix A. The exported data is sorted for the displacement components u_x , u_y , and u_z in the matrices \mathbf{U}_x , \mathbf{U}_y , and \mathbf{U}_z in relation to the position in x and y on the grid.

Figure 4.5 shows the maximum displacement for the 1:1 mode shape. The development of the mode shape identification algorithm is presented based on this mode shape. This mode shape is selected because it is the first mode showing oscillating in x - and y - directions.

Initially, the algorithm is only used to analyze OOP mode shapes with the displacement component matrix \mathbf{U}_z with shape $M \times N$. The Fourier transformation (FT) is often used for vibration analysis. The FT allows the analysis of displacement fields in the frequency domain, revealing the amplitudes and phase of the underlying wavenumbers. The wavenumbers, also called the spatial frequencies of a wave, represent the number of wave cycles on a defined distance in a given direction. The FT implementation as

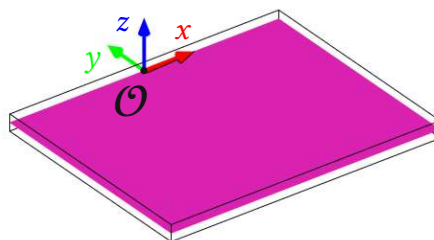


Figure 4.4: The plate, drawn as a wire body, with the axis orientation at the origin \mathcal{O} . The plane at half thickness marked in magenta is used for the data export.

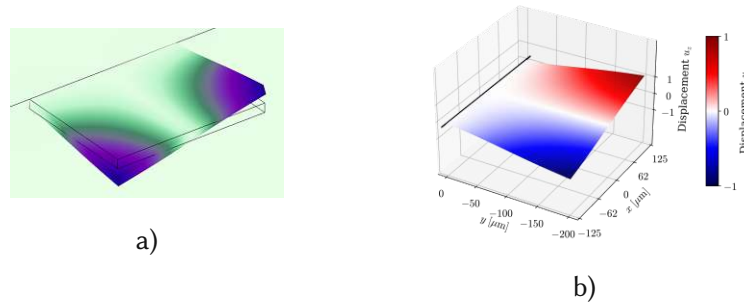


Figure 4.5: Visualizzazione of the 1:1 mode shape. In a) from *Comsol Multiphysics* and in b) the maximum displacement matrix $U_{z,max}$. The black tick line at $y = 0$ marks the anchor of the plate. In both images, the plate is $200 \mu\text{m}$ long and $250 \mu\text{m}$ wide.

2-dimensional discrete FT (2D DFT) will be used to analyze the extracted displacement field. *Numpy* this function is defined as

$$\alpha_{z,kl} = \sum_{m=0}^{M-1} \sum_{n=0}^{N-1} u_{z,mn} e^{-2\pi j(\frac{mk}{M} + \frac{nl}{N})}, \quad k = 0, \dots, M-1; \quad l = 0, \dots, N-1; \quad (4.1)$$

where $u_{z,mn}$ are the complex elements of the displacement matrix U_z and j the imaginary unit [35]. The resulting complex coefficients $\alpha_{z,kl}$ were stored the matrix α_z with the same shape as U_z . Because of the symmetry of the 2D DFT, the result contains the positive and negative count of the wavenumbers for both dimensions. However, only the positive spatial frequencies have a physical meaning. Therefore, the matrix can be reduced to the first quadrant. In order to better illustrate the relationship between the coefficients and the vibrations on the plate, $k \rightarrow \xi_x$ and $l \rightarrow \xi_y$ are used subsequently.

Figure 4.6 shows the heat map of the displacement matrix U_z and the amplitudes of the wavenumbers of the 2D DFT. The result marks the strongest amplitude at $\xi = (\xi_y, \xi_x)$

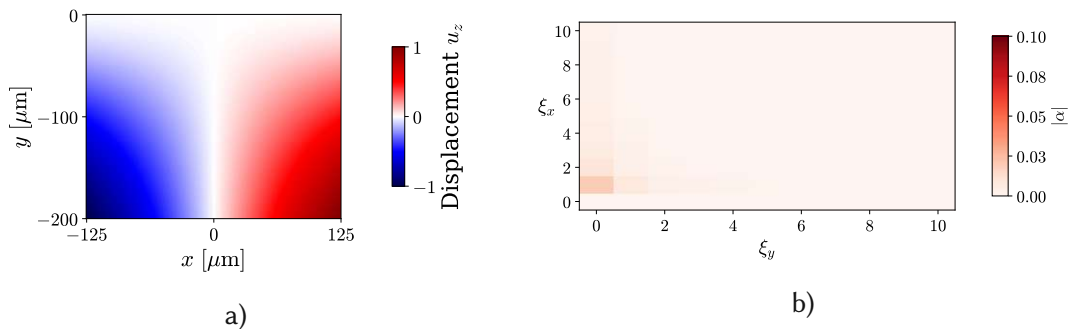


Figure 4.6: a) The maximum displacement field U_z for a 1:1 mode as a heat map. b) Plot of the amplitudes $|\alpha|$ for the wavenumbers of the displacement field U_z . Only a slice from the result matrix of the 2D DFT containing the first ten spacial oscillations in both directions is shown to ensure the visibility of the highest expected oscillation. It shows a maximum in $(\xi_y, \xi_x) = (0, 1)$. Each amplitude is normalized to the sum of all amplitudes in the first quadrant.

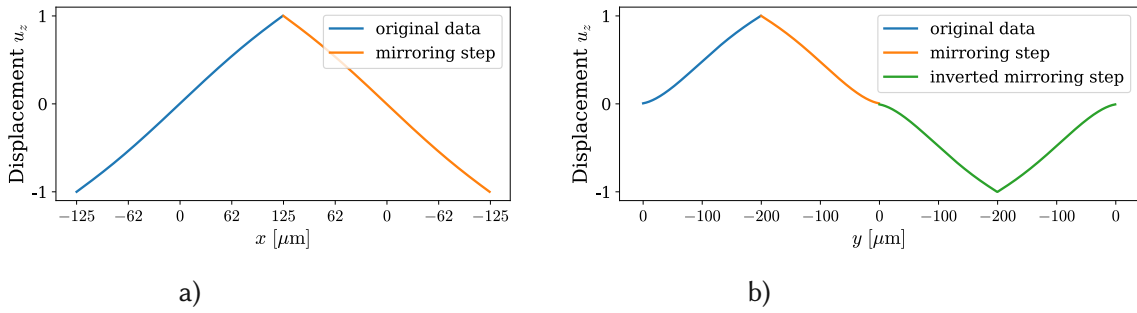


Figure 4.7: Steps from original to the extended displacement data for the 1:1 mode in a) along the free edge and b) along a lateral edge. Displacement is normalized and not in scale.

$=(0, 1)$. The wavenumber component $\xi_y=0$ shows that the section of the spatial oscillation period in this direction is not long enough to be recognized by the FT. For proper detection of the mode shapes, extending the dataset to obtain at least one complete oscillation period is necessary.

A series of mirroring steps are performed on the original data to achieve this extended dataset. Figure 4.7 a) shows the original displacement in x -direction along the free edge plotted in blue. This displacement shows a half period with positive and negative displacement. One mirroring step, plotted in orange, is enough to obtain a complete period.

In the y -direction, the first nodal line is fixed at the anchor, and in the 1: x mode, this is the only nodal line. Figure 4.7 b) shows the progress of the initial data along a lateral edge in blue. It is necessary to mirror the dataset at least two times to build a periodic displacement form from this merely rising line without a sign change. The second mirroring step data must be inverted to create the negative half period. Figure 4.7 b) shows the obtained period with all steps in different colors.

Figure 4.8 a) shows the extended dataset for the 1:1 mode shape as a 2D heat map. In b), the amplitudes of the wavenumbers from 2D DFT are shown. The significant maximum is located in (1,1). This result matches the nodal line count for this mode shape.

Inspecting higher mode shapes with the same algorithm shows that the result for ξ_y differs from nodal lines count. Because of the second mirroring step, the dataset is doubled twice in this direction. For the clamped-free plate, the displacement in the y -direction is always a nodal line at $x=0$ and never a nodal line on the free edge. Therefore, an even number of displacement periods in the extended dataset for this direction can never appear, and the wavenumbers with the component $\xi_y=\{2, 4, 6, \dots\}$ always have zero amplitude. This property of the wavenumbers is used to transform the FT result matrix to the nodal line count matrix. The nodal line count matrix is defined as $\xi \rightarrow n = (n_y, n_x)$ with $n_x=\xi_x$ and $n_y=\xi_{y'}$ for $y'=\{0, 1, 3, 5, \dots\}$. Analogous to the wavenumber ξ , the term n is called nodal number. With this transformation, the nodal line count matrix matches all possible mode shapes on cantilever resonators. Figure 4.9 shows as an example the 2:3 mode. In a), the original 2D DFT result matrix is shown, and in b), the nodal lines

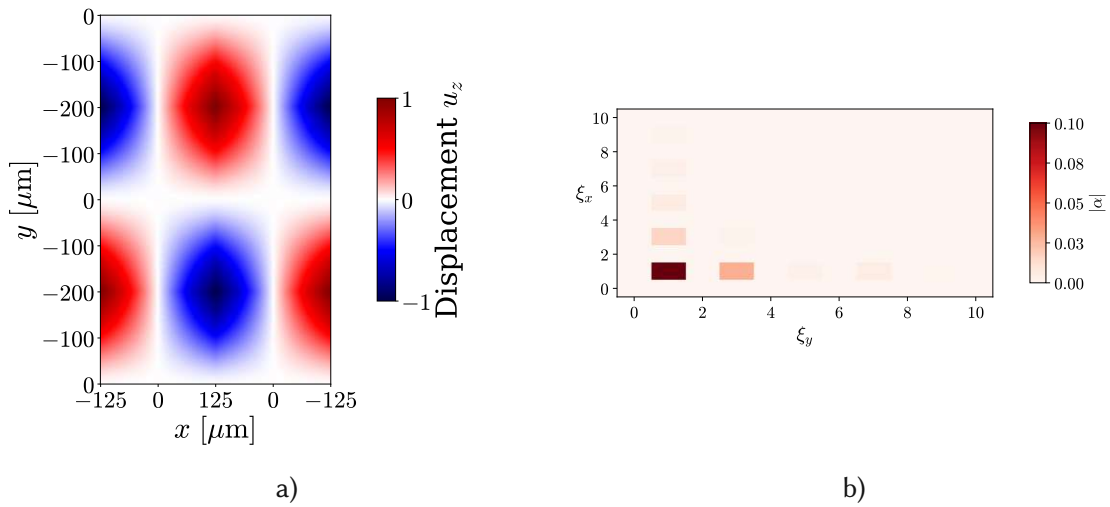


Figure 4.8: a) The extended dataset from U_z as a heat map. b) Slice of the result matrix from 2D DFT with the extended dataset

count matrix is shown. The presented method is also validated on higher-order mode shapes.

So far, only mode shapes that can be classified using the Leissa notation have been analyzed. Now, the result of a non-classifiable mode shape is shown. Figure 4.10 shows the analysis of a mode shape from the zoom region in Figure 4.2. Figure 4.10 a) shows the mode shape in 3D from *Comsol Multiphysics*, b) the 2D representation of the displacement matrix U_z , and c) the nodal lines count matrix for this displacement component. Significant amplitudes are shown for the nodal numbers (1, 3) and (2, 1). These different amplitudes show interference between two mode shapes, the 1:3 and the 2:1 modes. The amplitude for the nodal number (1, 3) is higher than for the (2, 1). Therefore, this mode shape is classified as a 1:3 mode. The interpretation of the different strengths of amplitudes is discussed in the following section.

From the results of the previous chapter, it is known that lateral and extensional mode shapes also appear in the defined frequency range. Therefore, the FT method is applied also to the displacement components U_x and U_y . Figure 4.11 shows the mode shape and the nodal lines matrices for the 1:0 mode. A significant amplitude is visible

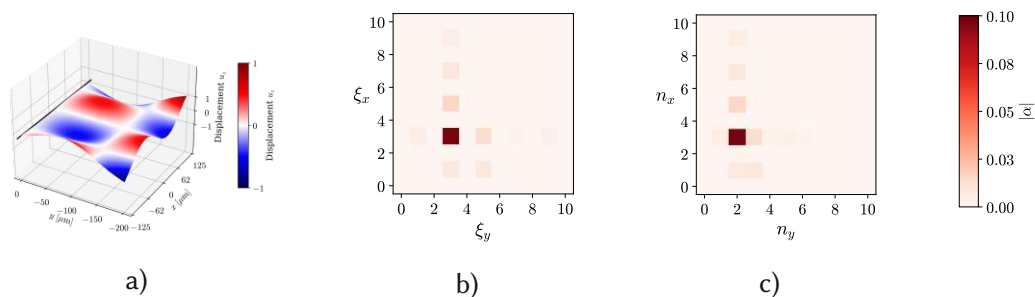


Figure 4.9: FT result matrices for the 2:3 mode, in a) the result matrix of the 2D-DFT with the extended data and in b) the nodal lines count matrix.

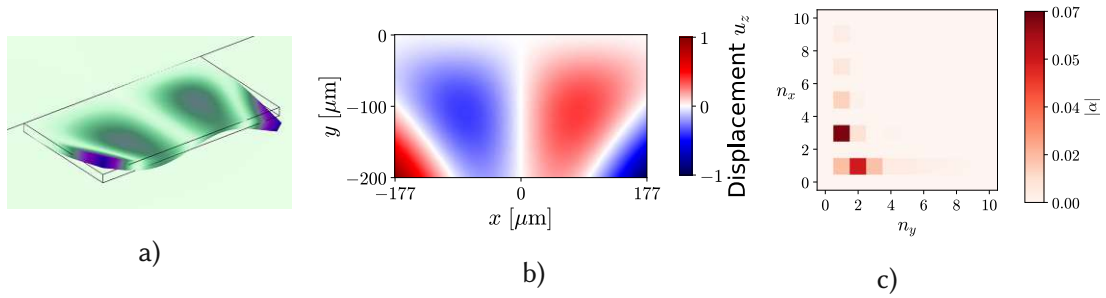


Figure 4.10: Transition mode shape: In a) the displacement pattern from *Comsol Multiphysics*, in b) the heat map of the displacement matrix U_z and in c) the nodal lines count matrix for the displacement component U_z .

only in c). This nodal number marks the OOP 1:0 mode. Figure 4.12 shows the mode shape and the nodal lines matrices for the 1st lateral EB mode. All sub-figures contain significant values, but the amplitude in b) is much higher. Therefore, the mode shape is identified from the displacement component U_x , as the expected 1st lateral EB mode. As an example of the extensional displacement, Figure 4.13 shows the 1st extensional mode shape. Besides the expected maxima in b) for the component U_y , also in the plot, c) a maxima is visible. The values are very close. The highest amplitude $|\alpha|$ is in c) for $u_y(1,0)$ 0.106 and in d) for $u_z(3,0)$ 0.103. So, the mode is correctly identified from the

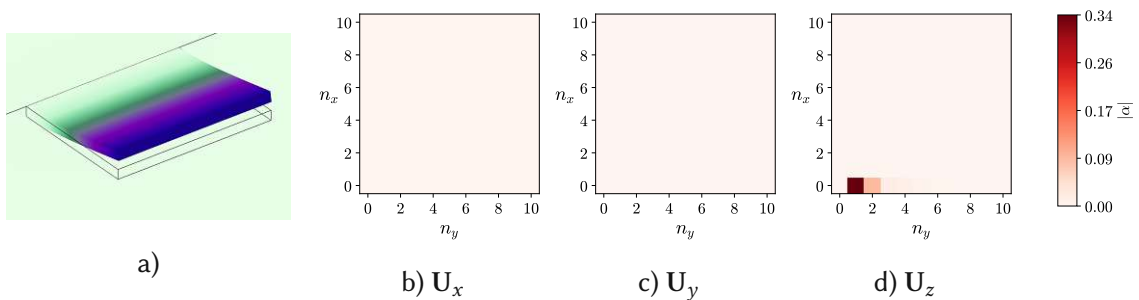


Figure 4.11: The 1:0 mode shape: The displacement pattern in a) and the nodal lines count matrix from displacement component U_x in b), from displacement component U_y in c), and from displacement component U_z in d).

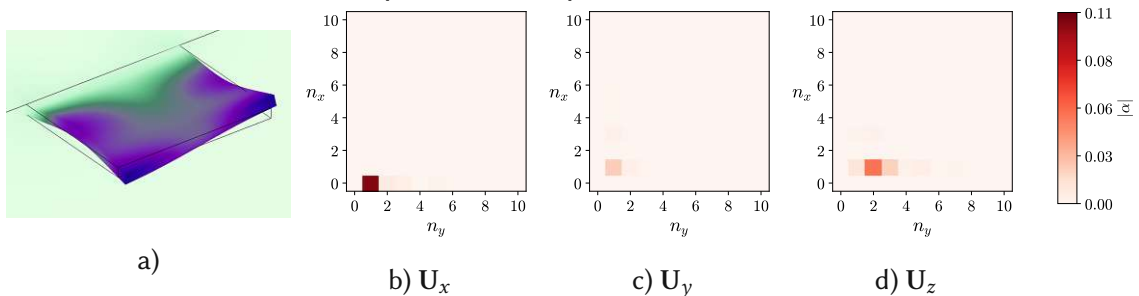


Figure 4.12: The 1st lateral EB mode: The displacement pattern in a) and the nodal lines count matrix from displacement component U_x in b), from displacement component U_y in c), and from displacement component U_z in d).

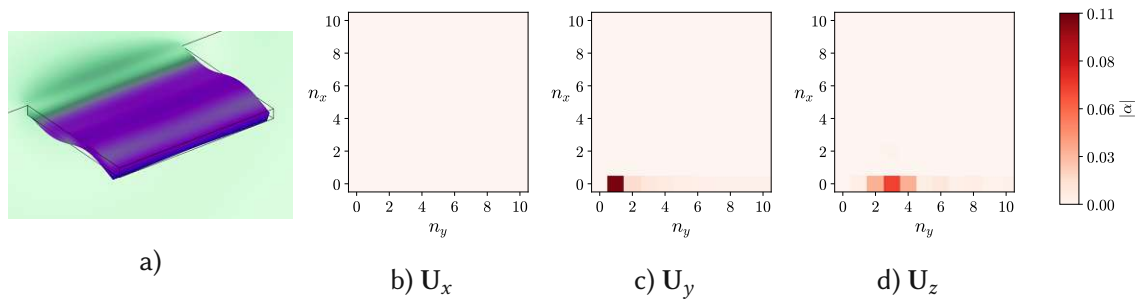


Figure 4.13: The 1st extensional mode shape: The displacement pattern in a) and the nodal lines count matrix from displacement component U_x in b), from displacement component U_y in c), and from displacement component U_z in d).

maximum amplitude in c).

By extending the FT method to all three spatial directions, an efficient tool has been developed to analyze the mode shapes. The resulting nodal line count matrices contain information about the underlying wavenumbers, represented by the nodal numbers. With this information, it is possible to characterize all occurring mode shapes.

4.2 Anchor losses of higher-order-out-of-plane mode shapes

Figure 4.14 shows the natural frequencies of a width sweep grouped by the identified mode shapes. The mode shape identification is made using the presented FT-based method. All the names are derived from the highest amplitude $|\alpha|$ of the three FT result matrices. The paths of Figure 4.3, which are identical to the mode shape curves, are annotated to the mode shapes in the legend. More often, these are paths with no intersections, but not only. The previous chapter showed that RTS modes tend to have

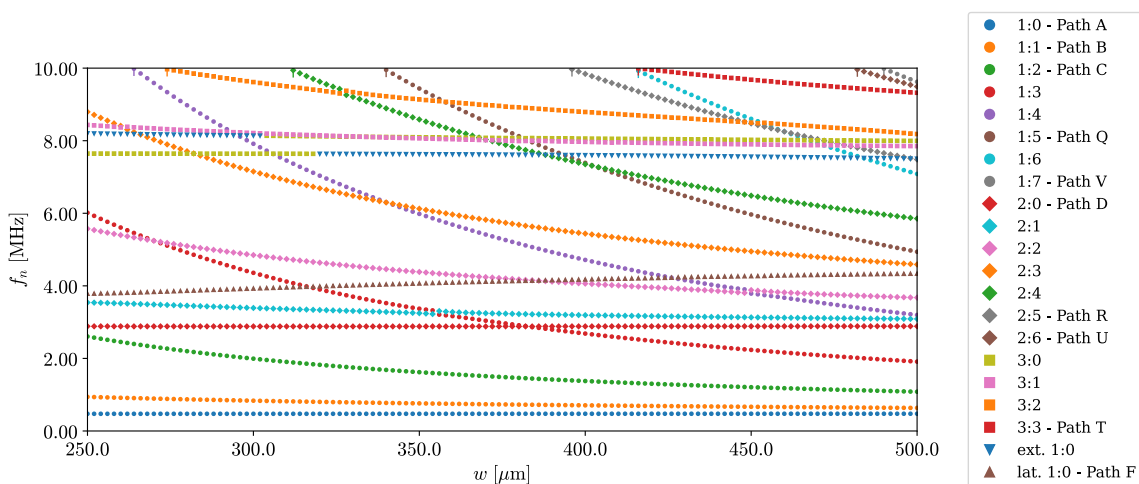


Figure 4.14: The resonance frequencies (f_n), identified from the FT based method, of the sweep simulation sorted by the mode shapes. For paths that only have one mode shape, it is noted in the legend.

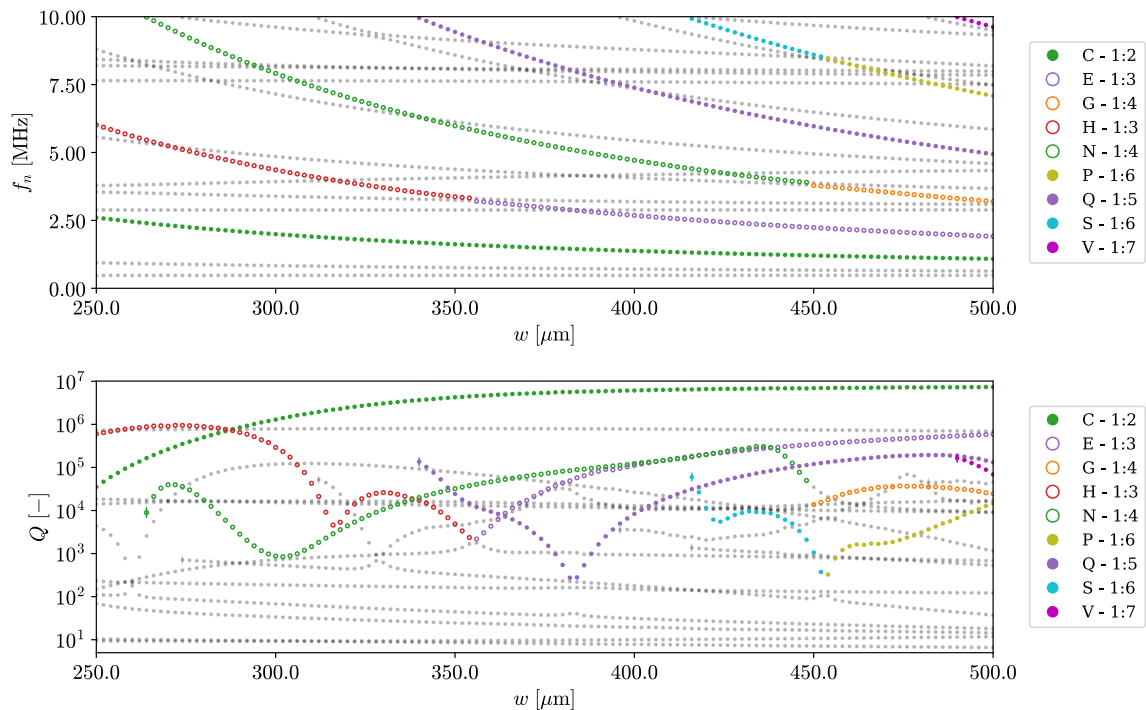


Figure 4.15: Plots of the natural frequency (f_n) and quality factor (Q) for the RTS modes. Different marks are used for different mode shapes. The first occurring point with a natural frequency below 10 MHz of each path is marked with | over the marker. In the background, all other eigenmodes are shown in gray.

higher Q-factors such as x:2, x:3, etc. However, this is not valid for all identified mode shapes. The reasons for these different Q-factors are evaluated with the information from this simulation sweep.

Figure 4.15 shows the natural frequency and the quality factor for all identified RTS modes. In frequency, all RTS mode shapes have a downward gradient and appear in ascending order of the mode types. The resonance frequency for the 1:2 mode shape is the lowest, followed by the 1:3, and so on. However, different paths of natural frequencies often appear on one mode shape curve. The quality factor is shown in the lower graph. For the first RTS mode, the 1:2 mode shape on path C, the natural frequency is always below 3 MHz. In this frequency region, the TED is contributing strongly to the total Q-factor, as presented in Section 2.1. However, this RTS mode shows the highest quality factor above 290 μm . This path increases and approaches asymptotically a maximum Q-factor slightly below 10^7 . A similar behavior is also expected for the other RTS modes, but they are all affected by variations. The underlying mechanisms of these variations are investigated in the next sections, beginning with the 1:3 RTS mode.

4.2.1 Mode shape interference on 1:3 RTS mode related paths

Figure 4.16 shows the resonance frequency and the quality factor for the 1:3 RTS mode. Two significant drops in Q-factor are identified. The first drop is around 320 μm and

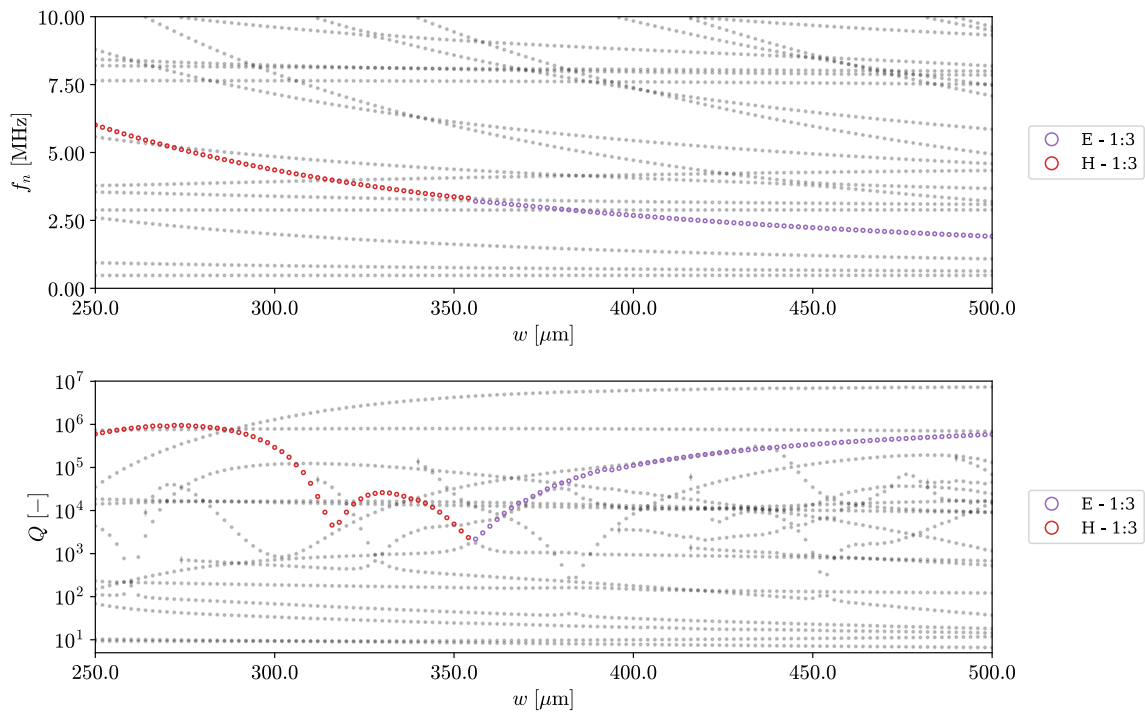


Figure 4.16: Plots of the natural frequency (f_n) and the quality factor (Q) for the 1:3 mode on the paths E and H . The \bullet marker identifies the 1:6 mode and the \diamond marker the 3:2 mode.

the second is around $355\ \mu\text{m}$. The region of the second drop is discussed in Figure 4.2. For these plate widths, the mode shape cannot be classified manually. The FT-based method shows that the dominant amplitude is the nodal number (1,3). This region is investigated first, and the first drop is discussed afterward.

Avoided crossing between path E and path H

The 1:3 RTS mode appears on two different natural frequency paths, on path H and path E . The resonance frequencies and the Q-factors for the simulated widths of both paths are shown in Figure 4.17. The natural frequency is shown in the upper plot. Initially located on path H , the resonance frequency of this mode shape is above 3 MHz. After the exchange to path E , the natural frequency sinks and reaches approximately 2 MHz. The quality factor is shown in the plot below. On path H for plate widths below $300\ \mu\text{m}$, the Q-factor is extremely high, always above $5 \cdot 10^5$. Afterward, a strong drop is visible, with the minimum below $5 \cdot 10^3$. This is a drop of more than two orders of magnitude for a change in width of only $17\ \mu\text{m}$. Afterward, the Q-factor increases to $3 \cdot 10^4$ in a short interval. Subsequently, the value is newly decreasing until the crossing with path E .

The region where path E and path H are very close in frequency and the quality factors cross is evaluated more in detail. Figure 4.18 shows the results of this simulation with $0.5\ \mu\text{m}$. In the frequency plot, it is visible that the path E and Path H are always apart from each other. Nevertheless, it seems that the respective slopes are exchanged. In literature, this phenomenon of noncrossing eigenfrequencies is called

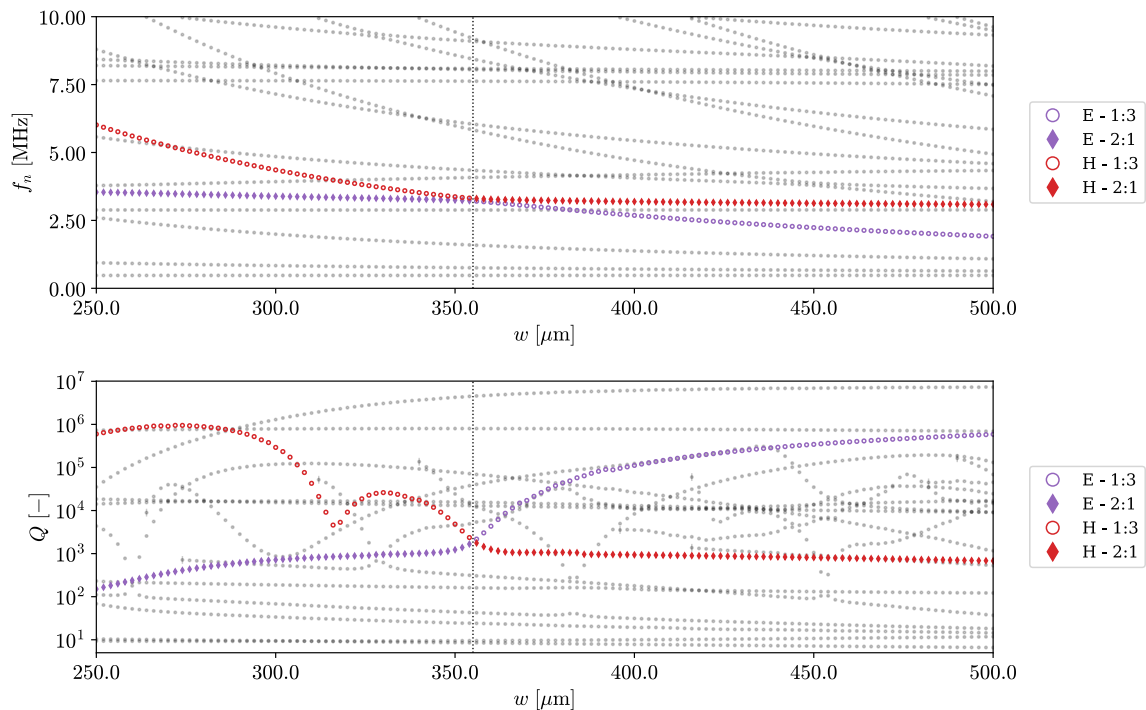


Figure 4.17: Plots of the natural frequency (f_n) and the quality factor (Q) for paths E and H . The \circ marker identifies the 1:3 mode, and the \blacklozenge marker the 2:1 mode.

avoided-crossing, curve veering, mode-splitting, etc. [36, 37]. This phenomenon is related to the dispersive coupling of two eigenmodes, which leads to a repulsion of the natural frequencies. This phenomenon only appears if the coupling between these mode shapes is strong enough. Therefore, not all interfering mode shapes can be affected by avoided crossing [38].

In Figure 4.18, the identified mode shapes are annotated at the resonance frequency curves' beginning and end. Different marker styles were also used to identify the mode shapes along the paths. The circle marks the 1:3 mode, and the diamond marks the 2:1 mode. The width III marks the plate where the natural frequencies are at the minimum distance. The other width markers are only for reference and are positioned arbitrarily. At the width III , it is visible that both paths were identified as the 1:3 mode. This will be further discussed when analyzing the FT result. The displacement patterns at the different marked widths are shown in the upper and lower part of Figure 4.18 widths. The upper row shows path H and the lower path E . The mode shapes can be clearly identified at the lowest and highest widths for both paths. However, in between, the nodal lines are not positioned only in the parallel or longitudinal direction. Therefore, assigning them a mode shape with the selected notation is not always possible. However, viewing the images for each path one after the other, it looks like the nodal lines are moving and rotating in the x - y plane. Only the longitudinal nodal line in the center of the plate, which appears on both mode shapes, is not moving. This movement in the displacement pattern creates the transition from the initial mode shape to the ending mode shape. For path H at width I , the 1:3 mode is clearly identifiable. However, in

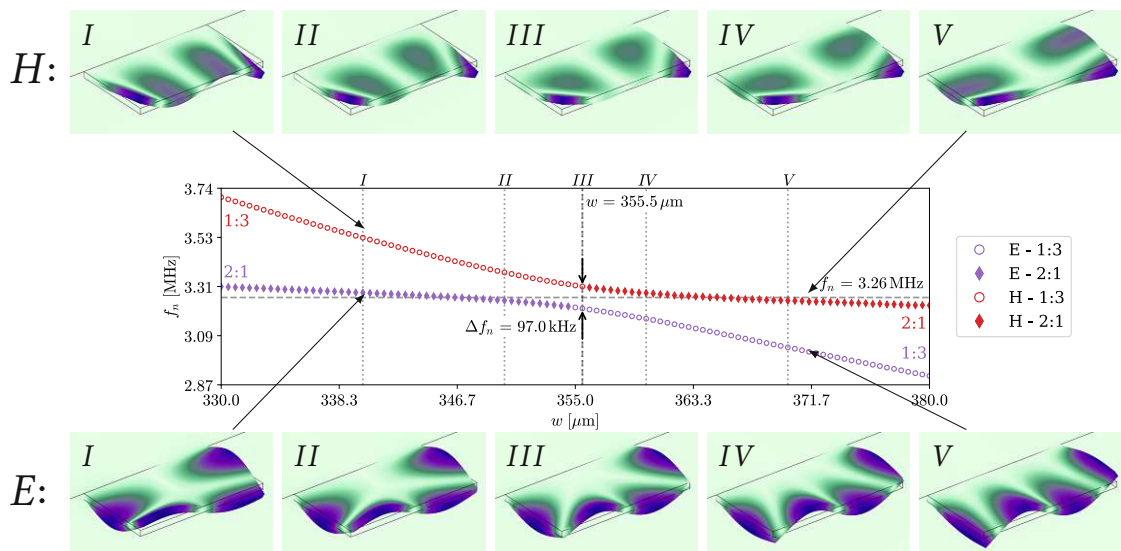


Figure 4.18: Avoided-crossing of path E and H : The graph in the middle shows the natural frequency (f_n) over the plate width (w). The pictures above and below show the displacement patterns at the widths I to V , as marked in the plot. Above for the path H , below for path E .

mode shape II , the lateral nodal lines no longer end in the anchor region. Instead, they end on the lateral surfaces of the plate. This movement continues in the third and fourth images. In the mode shape at width V , the former lateral nodal lines merge and build the second parallel nodal line for the 2:1 mode. Comparing the last mode shape from path H with the first from path E shows the opposite inclination of the parallel nodal line on the plate. However, both are clearly showing a 2:1 mode. The following image shows how the parallel nodal line in the center moves to the anchor while the ends move from the lateral edges to the free edge. In the displacement pattern III , the lines start from the free corners and end at half-width in the anchor. At this plate, the distance between the two natural frequencies has its minimum. From the following image, the mode shape is identifiable as 1:3 mode. At the width V , the lateral nodal lines show the opposite inclination compared to the initial 1:3 mode on path H .

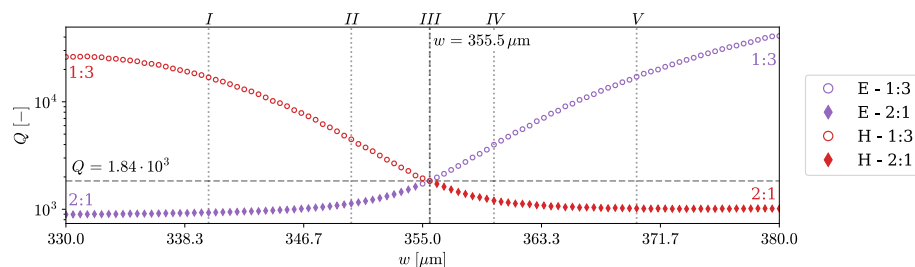


Figure 4.19: Avoided-crossing of path E and H : The graph shows the quality factor (Q) over the plate width (w). The markers I to V are referring to the displacement patterns depicted in Figure 4.18.

Figure 4.19 shows the related quality factor for the two paths in frequency. The Q-factor is strongly affected on an interval of only $30\ \mu\text{m}$. For the curve E starts below 10^3 and reaches more than $2 \cdot 10^4$. The opposite inclination is visible on path H . It starts slightly below $2 \cdot 10^4$ and drops to approx. 10^3 . The quality factors for the same mode shape at the beginning and the end are very close. This shows that the Q-factors are a property of the displacement pattern. In the transition zone between I and V , the higher Q-factors decrease by about one order of magnitude up to the equality point in III , while the lower Q-factors only increase by a factor of around two. The equality point is found exactly at the same plate width, where the minimum distance in eigenfrequency is located. Compared to the natural frequency plot, the impact of avoided crossing is visible much stronger in the Q-factor plot.

Figure 4.20 shows the FT method result for the widths I to V . The amplitude $|\alpha|$ for the participating nodal number u_z (1,3) and (2,2) are annotated in each subfigure. No other significant amplitude is found. Starting in the upper row from the left, it shows that path H is initially a 1:3 mode shape. The second maxima appears for the nodal number u_z (1,3) and has a much lower value. In the lower row, it is the opposite situation. The nodal number u_z (2,2) has a much higher value than the nodal number u_z (1,3). In the second column, both higher values decrease while the lower ones increase. In the middle column for width III , the values for each path are very close. At this width is the intersection point of the Q-factor and the nearest distance in frequency for the paths. As mentioned before, it is also remarkable that the highest amplitudes appear at the same point for both result matrices. Therefore, both paths were classified as being in the 1:3 mode. This shows that for one simulated plate width, it is possible to detect the same mode shape as FT maximum in two different natural frequencies while they are in avoided crossing. However, in Figure 4.18, the displacement patterns III of both paths can be distinguished clearly from each other. The increased amplitudes at the width IV in Figure 4.20 are also visible in the mode shape plots from Figure 4.18. They are becoming more similar to the initial mode shapes of the opposite path. To focus more on the two significant nodal numbers, Figure 4.21 shows the amplitudes of these nodal numbers over the width. In the upper plot for path H in the lower plot for path

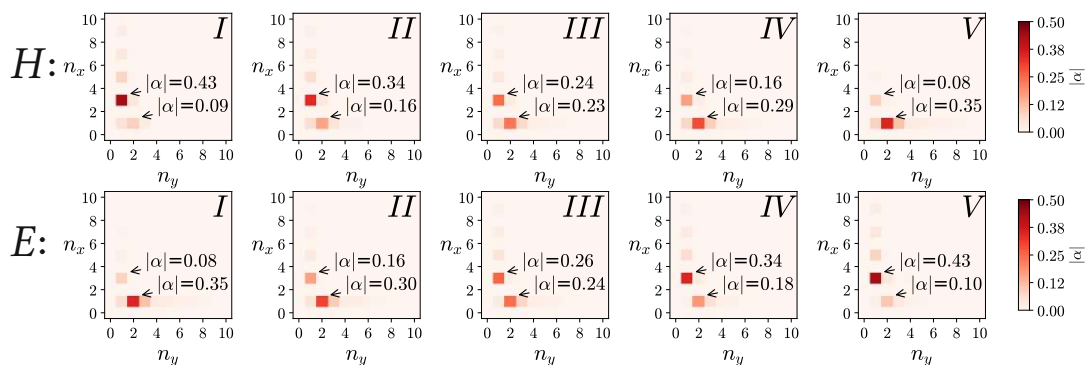


Figure 4.20: Nodal lines count matrices from FT-based method for U_z for the widths I to V . Nodal lines count matrices from FT-based method result for the widths I to V . The amplitudes for nodal numbers u_z (3,1) and u_z (2,1) are annotated.

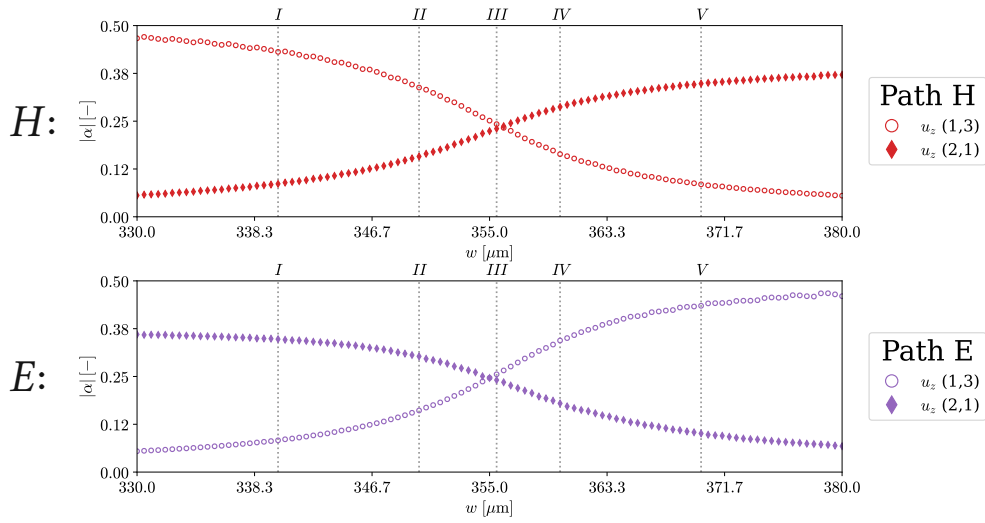


Figure 4.21: The amplitudes of the nodal numbers $u_z(1,3)$ and $u_z(2,1)$ for path H and path E .

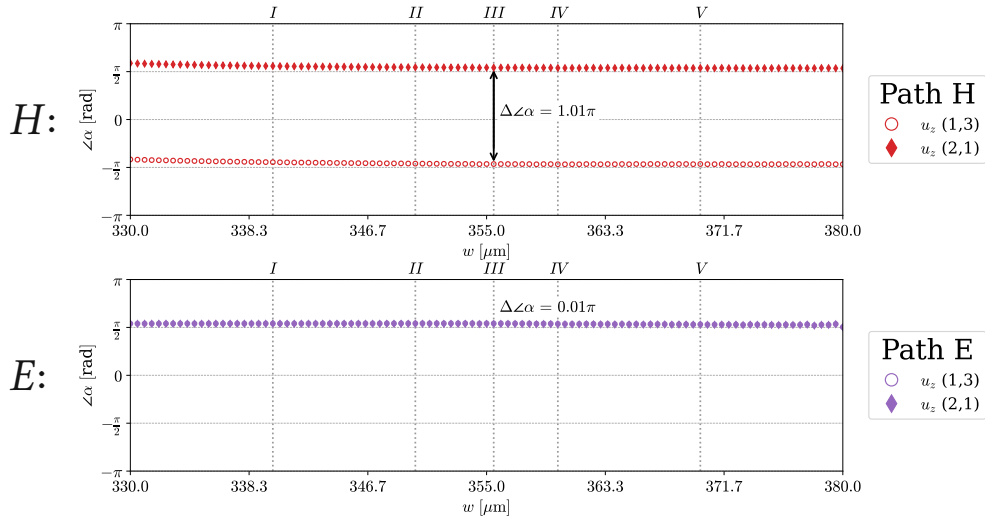


Figure 4.22: The phase of the nodal numbers $u_z(1,3)$ and $u_z(2,1)$ for path H and path E .

E . It is visible that for each path, the amplitudes of both maxima have the intersection point around the width III . Figure 4.22 shows the phase of both maxima. For path H , the nodal numbers $u_z(1,3)$ and $u_z(2,2)$ are anti-phase. However, they are both constant around the avoided crossing and are distant approximately π . For path E , the nodal numbers are in-phase. These two plots show that the complex FT result is different for both paths, also when the amplitudes are equal.

This evaluation shows the advantage of the FT-based analysis on the simulation data. It makes it possible to analyze the curve veering more effectively and precisely than manual visual inspection.

"Q-drop" crossing on path H

Figure 4.16 shows for the path H at the first dip in the Q-factor plot no interacting curve. In the resonance frequency plot, a crossing with another path is visible. This path is identified as the 1st lateral EB mode shape on path F . Figure 4.23 shows these two paths, with the marked width of the minimum Q-factor on path H . The region among this drop is evaluated in more detail. Therefore, a sweep with smaller steps in width is executed. The results are shown in Figure 4.24. In the upper part are shown five displacement patterns, visualized from Comsol Multiphysics, for the path H . All displacement patterns for path H are showing a clean 1:3 RTS mode. In the lower part are shown the displacement patterns for path F at the same widths. All displacement patterns in this row look the same, and the lateral deflection is clearly visible. From visual comparison, no interaction is found. Between these images are shown the plots of resonance frequency and quality factor. The widths I to V of the depicted displacement patterns are marked in these plots. Also, the width of the intersection is marked in the frequency plot, and in the Q-factor plot, the width is marked with the minimum difference in the quality factor.

Figure 4.25 shows the related nodal numbers from the nodal lines count matrix. The plots at the right show that only the nodal number for the visible mode shape has a significant amplitude for both paths. The interfering nodal number's amplitude is very low in both cases. In the upper plot in the middle of the shown interval, the nodal number u_x (1,0) significantly increases. The larger amplitude of the u_z (1,3) decreases slightly only around this position. In the lower plot, the curves have similar behavior, but the changes are weaker, as for the path H . On the left is the plot of the phases. It shows that the nodal number u_z (1,3) has a phase change in opposite directions. The

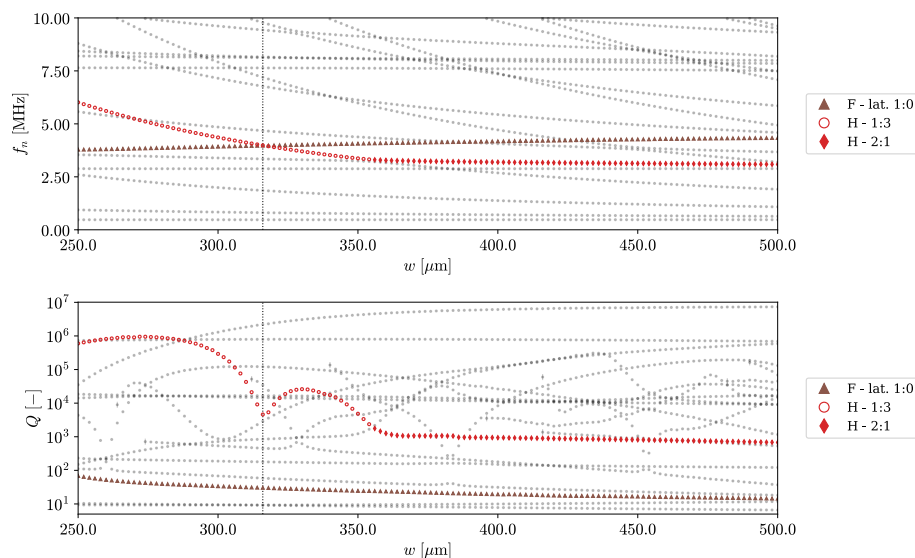


Figure 4.23: Plots of the natural frequency (f_n) and the quality factor (Q) for paths F and H . The \circ marker identifies the 1:3 mode, the \diamond marker the 2:1 mode, and the \blacktriangle the lateral 1:0 mode. The width of the first minimum of path H is marked with a dotted line.

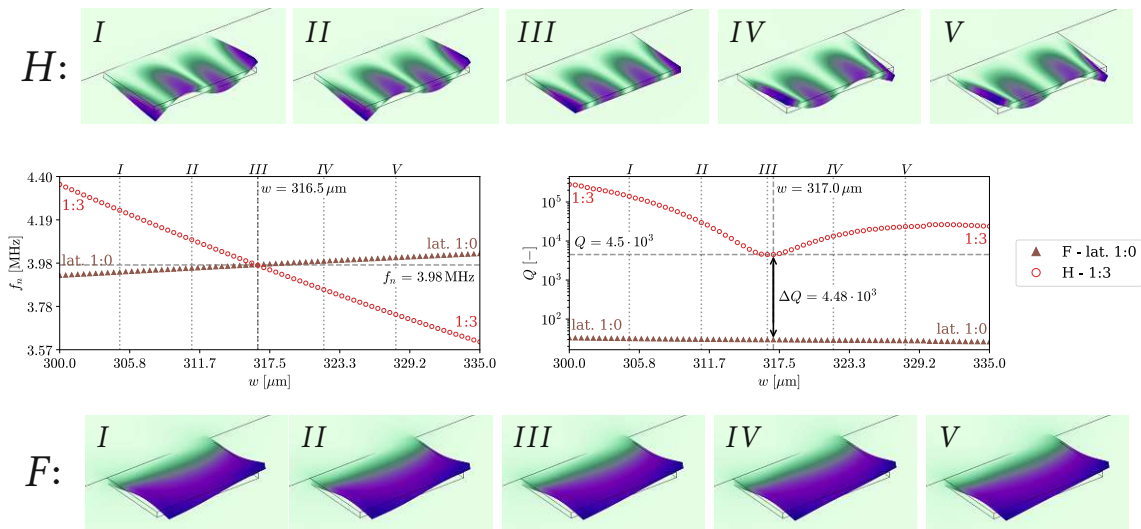


Figure 4.24: Crossing of path F and H : The graph in the middle at left shows the natural frequency (f_n), and the graph at middle right shows the Q-factor (Q). The pictures above and below show the displacement patterns at the widths I to V . Above for the path H , below for path F .

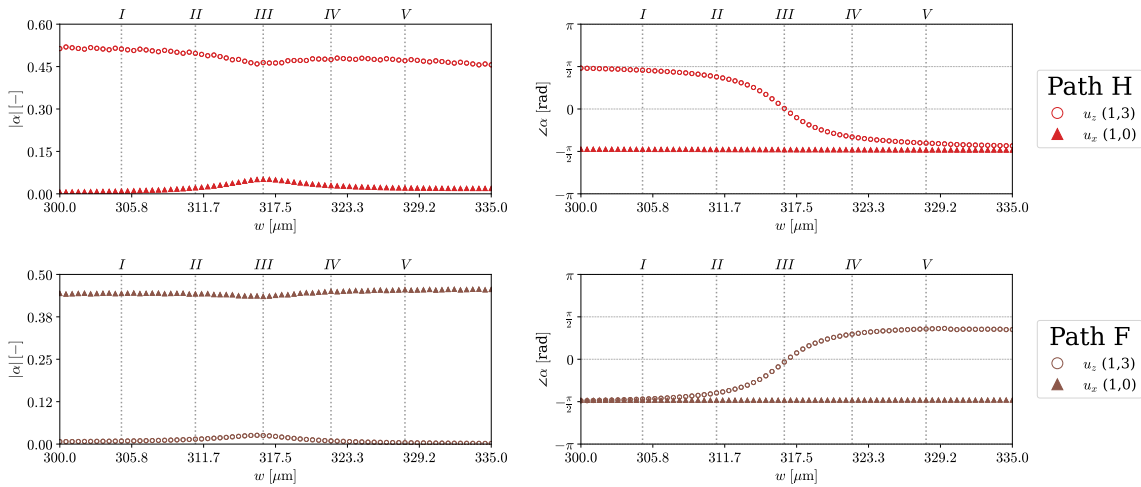


Figure 4.25: The complex amplitudes of the nodal number u_z (1,3) and u_x (1,0) from FT result splitted in modulus at left and argument at right. Above is shown the path H and below the path F .

phases in both plots cross 0 around the intersection of the natural frequency.

This mode shape interference affects, in contrast to avoided crossing, only the losses of the path with the higher quality factor. The Q-factor of the other interacting path is initially more than four orders of magnitude lower and, at the minimum, more than two orders of magnitude. While these paths cross in frequency, a tiny interference is detected. This small perturbation in the displacement pattern has a major impact on the Q-factor of path H .

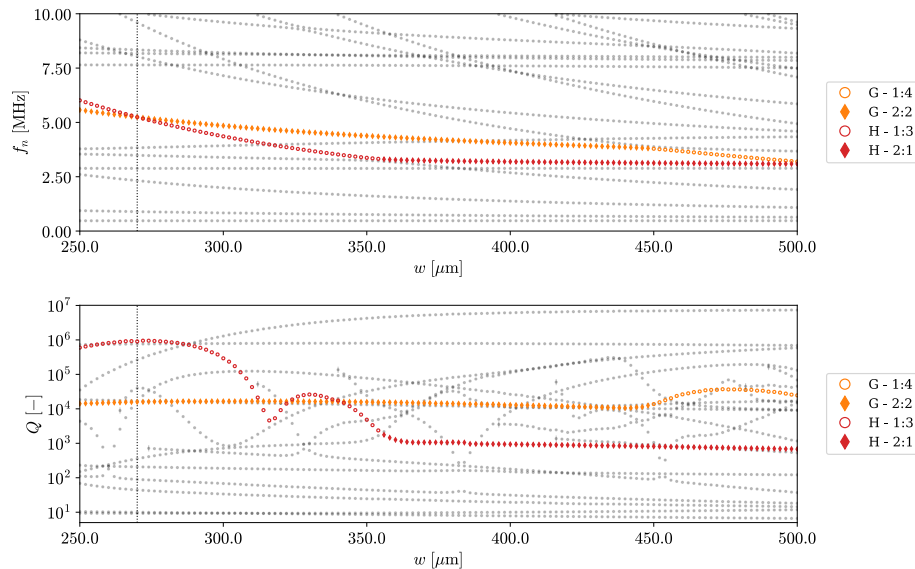
Simple crossing between path G and path H 

Figure 4.26: Plots of the natural frequency (f_n) and the quality factor (Q) for paths G and H . The \circ marker identifies the 1:3 mode, and the \diamond marker the 2:1 mode. The width of crossing resonance frequencies is marked with a dotted line.

After analyzing two points where the quality factor is affected by mode shapes with similar or equal resonance frequency, a crossing in frequency is analyzed without effect on the Q-factor. In Figure 4.26 is shown the crossing between the 1:3 mode on H and the 2:2 mode on path G .

Figure 4.27 shows the crossing region in more detail. On the left are the natural frequency curves plotted, and the quality factor is on the right. The paths cross in frequency at the plate width of $270\ \mu\text{m}$, marked as width III . For reference, the other width markers are placed arbitrarily around this position. The Q-factor for the 1:3 mode is much higher than the 2:2 mode, and the curves are not affected during the crossing. The amplitudes of the nodal lines count matrices are plotted in Figure 4.28 for the widths I to V . The values of both amplitudes are shown in the annotation. Both paths show only one peak for the nodal number of the related mode shape, and no other significant amplitudes appear.

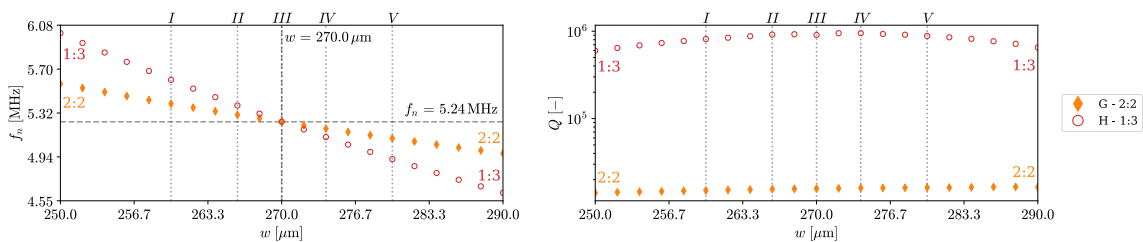


Figure 4.27: Crossing of path G and H : The graph at left shows the natural frequency (f_n) over the width w and the graph at right the Q-factor (Q) over the width w .

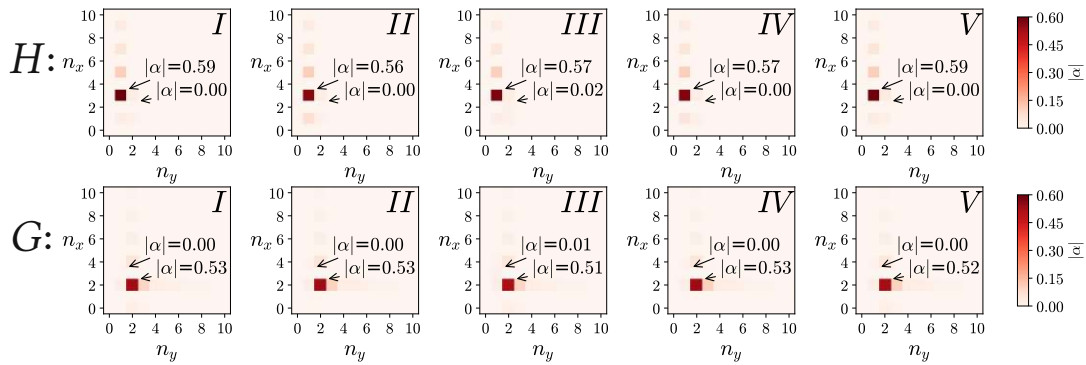


Figure 4.28: The nodal line count matrices from FT-based method with the displacement matrix U_z for the widths I to V .

These results show that no interference occurs during the crossing of these mode shapes.

Summary of the crossing mechanisms

Table 4.2 summarizes the identified crossing mechanisms and assigns them to a symbol for identification. The first example of this section shows how avoided crossing affects the Q-factor and the displacement pattern of both interacting paths. The resonance frequencies only slightly change in this region, while the quality factor decreases or increases heavily. The displacement patterns show a superposition of the participating

Phenomena	$f_n(w)$	$Q(w)$	Symbol
<p>Avoided crossing:</p> <p>The resonance frequencies do not cross, while the quality factors indeed cross. The displacement patterns show the superposition of the interfering mode shapes.</p>			
<p>”Q-drop” crossing:</p> <p>The resonance frequencies cross. The higher quality factor strongly decreases in a tiny interval, while the lower one is not affected. Both displacement patterns are also not affected.</p>			
<p>Simple crossing:</p> <p>The resonance frequencies cross. The quality factors and the displacement patterns are not affected.</p>			

Table 4.2: Mode shape interference patterns on plate resonators

mode shapes. However, analyzing these patterns requires much more effort than determining the Q-factor. Therefore, the quality factor is a better criterion for identifying this phenomenon.

The second example illuminates the behavior of "Q-drop" crossing. At "Q-drop" crossing, only one mode shape is affected by a drastic decrease in the quality factor. However, the minimum of this Q-factor is always at a much higher level than the Q-factor of the second path. Therefore, they can always be distinguished clearly. Neither the resonance frequency nor the displacement patterns are affected by the "Q-drop" crossing. Also, for this phenomenon, the quality factor is a suitable criterion. The last example shows the crossing in frequency, where no interference between the mode shapes is detected.

4.2.2 Analysis of mode shape interference on other paths

With the knowledge of the interference phenomena identified in the 2nd RTS mode, all other paths are evaluated and categorized. The following paragraphs do not describe new phenomena but the same interference patterns with more complex behavior, as in the last three examples.

Avoided crossing between path G and path N

Figure 4.29 shows the paths where this mode shape appears. The 1:4 mode shape appears on path N for the first time on the plate width of $264 \mu\text{m}$ with a natural frequency slightly below 10 MHz . The resonance frequency for this mode shape continuously decreases and, on path G , reaches 3.2 MHz at $500 \mu\text{m}$. An avoided crossing among the

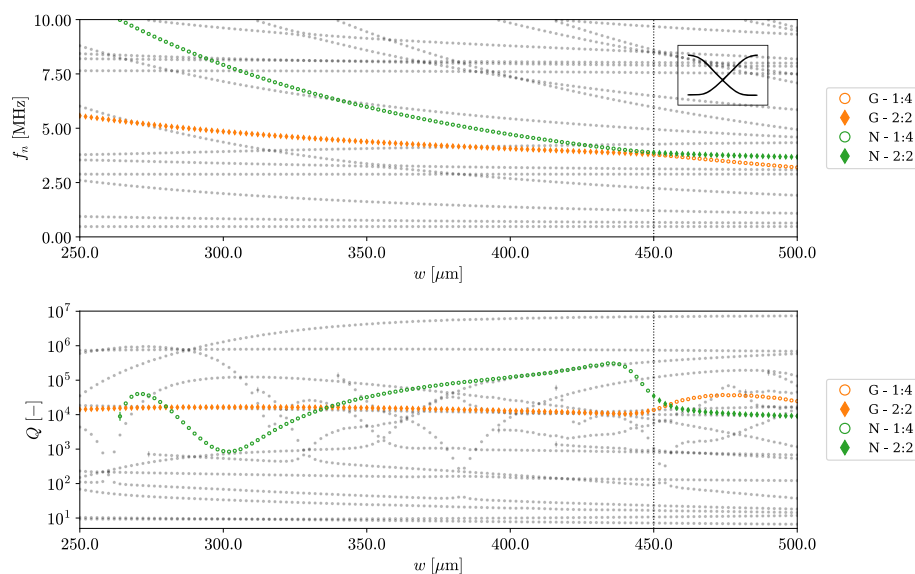


Figure 4.29: Plots of the natural frequency (f_n) and the quality factor (Q) for paths G and N . The \circ marker identifies the 1:4 mode, and the \diamond marker the 2:2 mode. The first occurring point of path N is marked with $|$ over the marker.

marked width 450 μm is visible from the frequency paths. The Q-factor plot shows a crossing for these paths at a higher width. However, the involved mode shapes, identified from the FT-based method, are swapped right at the marked width. The Q-factor crossing and the mode shapes swap are shown on the same plate width for the example of the paths *E* and *H*. This different behavior will be analyzed with a higher width resolution.

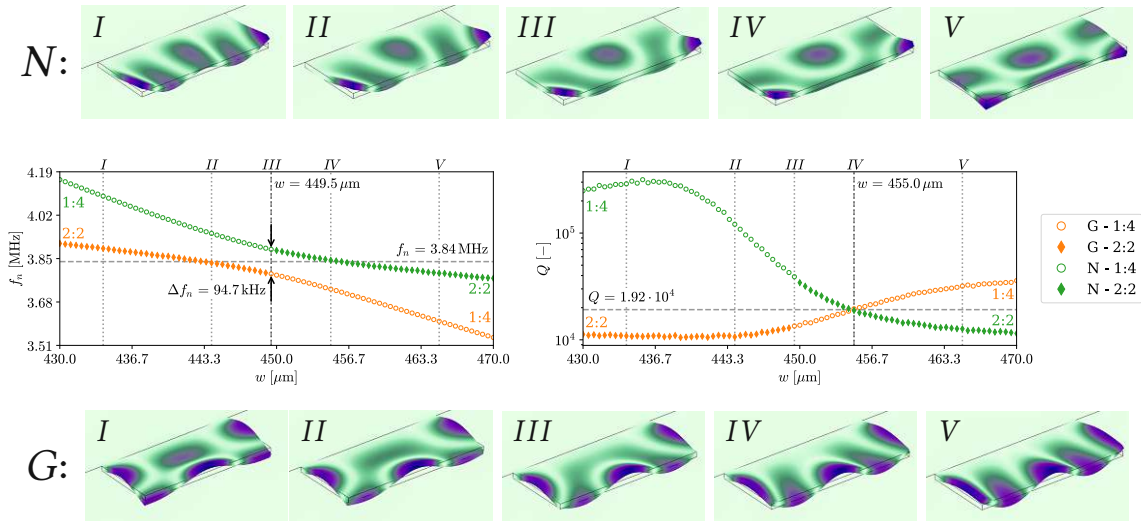


Figure 4.30: Avoided-crossing of path *G* and *N*: The graph in the middle at left shows the natural frequency (f_n), and the graph at middle right shows the Q-factor (Q). The pictures above and below show the displacement patterns at the widths *I* to *V*. Above for the path *N*, below for path *G*.

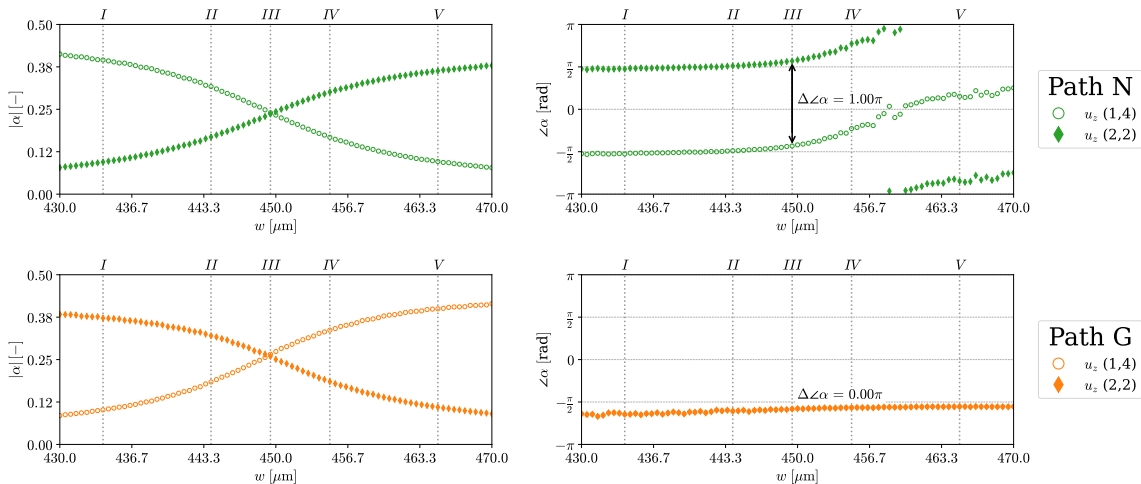


Figure 4.31: The complex amplitudes of the nodal numbers $u_z(1,4)$ and $u_z(2,2)$ resulting from the FT-based method spitted in modulus at left and argument at right. Above is shown the path *N* and below the path *G*.

Figure 4.30 shows eigenfrequencies in the right plot and the quality factor at the left. The frequency plot shows that the curves G and N exhibit avoided crossing. They become very close to each other without crossing in the interval from width I at $434\ \mu\text{m}$ to width V at $465\ \mu\text{m}$. The width III marks the closest distance in frequency where both paths are identified as 1:4 modes. For both paths, the mode shapes II , III , and IV cannot be classified using the Leissa notation.

The nodal lines are curved or even circular, and some do not show a direct course in parallel or longitudinal direction. The Q-factor, shown in Figure 4.30 at right, for path N starts very high. From $439\ \mu\text{m}$ on, it decreases sharply until the width IV afterward decreases much slower. The Q-factor of path G until the width II is nearly constant. Then, the values increase slowly during the curve veering until the width V afterward becomes more stable. The crossing of the quality factors is located at a much higher width than plate III . This is quite unexpected and will be evaluated, focusing more on the related mode shapes. The quality factor's initial and final values of the 2:2 mode are not significantly changed. It is different for the 1:4 mode. There, the values are approx. one order of magnitude distant. Because the quality factor for this mode shape is much lower at the end, the path G has a lower slope than path N . Due to the different gradients of the paths, the equality point of the Q-factor may have shifted to a wider plate. Figure 4.31 shows the at the left amplitudes and at the right the phase for the nodal numbers $u_z(1,4)$ and $u_z(2,2)$ of the paths. The amplitude plots look very similar and intersect around width III at similar widths. The largest amplitude at the width III is the nodal number $u_z(1,4)$ for both paths. However, the values are very close, and no amplitude dominates on both paths. The argument of the maxima is plotted on the right of the figure. For the path N , the shown nodal numbers are anti-phase, and for the path G , they are in phase for the entire plotted width. Both path phases of path N are shifted around $3/4\pi$ in the interval between width II and V . This phase change is also visible in the displacements. Comparing the displacement patterns IV and V shows that the corners of the free edge are bent oppositely. The phases for path G are constant, although the free corners are bent in opposite directions in the related displacement patterns, I and V . Following the mode shape transition shows that the relevant bending to compare is not in the corner for the 2:2 mode. The 1:4 mode has in his free corners ending the first bending from the anchor. Considering also the bending starting from the anchor for the 2:2 mode, both displacements are in the same direction, which means they are in phase. The phase for the 2:2 mode at width I in path G and at width V in path N shows the same sign. The bending of the free corners in the related mode shape plots of Figure 4.30 shows in the same direction. This bending shows that the osculations are in phase.

This example shows that the minimum distance in frequency does not determine the width of the intersection of the quality factor.

”Q-drop” crossing on path N

Figure 4.29 shows for path N around $300\ \mu\text{m}$ an intense decrease in Q-factor for more than one order of magnitude. To analyze this drop, the FT-based method is applied to the width of the minimum value.

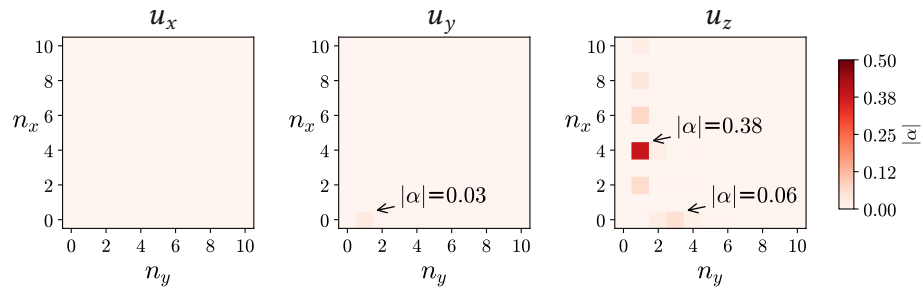


Figure 4.32: Plot of the amplitudes $|\alpha|$ identified from FT method, applied to the three displacement components of path N at the minimum Q-factor on the plate width of 302 μm

Figure 4.32 shows the resulting amplitudes for the individual displacement components. Besides the expected 1:4 amplitude, there are also small but significant amplitudes for the OOP 3:0 mode shape and the extensional 1:0 mode shape. At this width, the OOP 3:0 mode shape appears on path J , and the extensional 1:0 mode shape appears on path K . Figure 4.33 shows all interfering paths.

For further investigations, this region is simulated with smaller width steps. Figure 4.34 shows in the first row the displacement patterns for path N , then the graphs for the natural frequency and the Q-factor, and below the displacement patterns for path K and J . The graph on the right shows how near in frequency the three paths are in this interval. The marked widths, II and IV , are positioned at the intersections between the paths. On the left is the plot of the quality factors, and there at the marked width III is the closed distance in between the path N and the two other paths. At the closet width, the distance from the higher to the lower Q-factors is around two orders of magnitude, while the lower paths have similar values. The displacement patterns for path N look

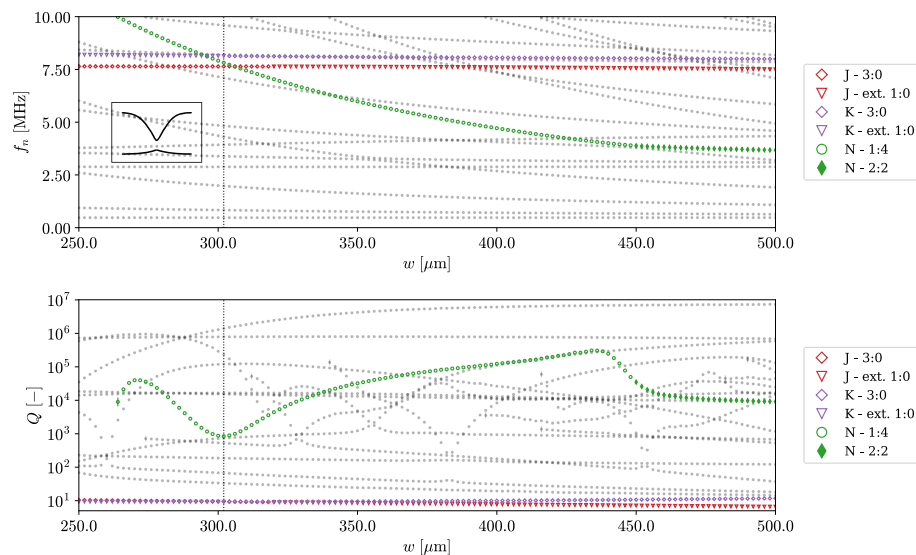


Figure 4.33: Plots of the natural frequency (f_n) and the quality factor (Q) for paths J , K and, N . The width of the first minimum of path N is marked with a dotted line. The first occurring point of path N is marked with | over the marker.

quite the same on all widths. No visual impact can be identified. The displacement patterns below the plots show the influence of the OOP 3:0 and the extensional 1:0.

Figure 4.35 shows the three relevant amplitudes and phases for all paths. The first row shows the path N results. The amplitude of the nodal number $u_z(1,4)$ decreases around the width III , while the other two nodal numbers have a small increase. This increase shows that the other nodal numbers are influencing the Q-factor of the path N . The phases for all paths are not constant during the interval. Initially, the nodal number $u_z(1,4)$ is in phase with the nodal number $u_z(3,0)$ and out of phase with the nodal number $u_y(1,0)$. At the width V , it is out of phase with the other nodal numbers. Around the width III , the nodal number $u_z(1,4)$ and the nodal number $u_y(1,0)$ have equal phases, while the phase of the nodal number $u_z(3,0)$ is distant around $\pi/2$. The plot in the middle shows the nodal numbers for path K . The nodal number $u_z(1,4)$ has a very small amplitude along the whole interval. The other amplitudes cross around the width III . This width is defined by the FT method, where the dominant mode shape is exchanged for this path. Until the crossing at $303 \mu\text{m}$, it is defined as the extensional 1:0 mode, afterward as the OOP 3:0 mode. The phase plot shows that these mode shapes are rather constant in phase. The nodal number $u_z(3,0)$ is decreasing slightly and always distant more than $\pi/2$ to the nodal number $u_y(1,0)$. The nodal number $u_z(1,4)$ starts in phase with the nodal number $u_y(1,0)$ mode shape. It changes the phase and reaches a difference of $\pi/2$ to this mode shape at the end of the interval. The graphs for path J

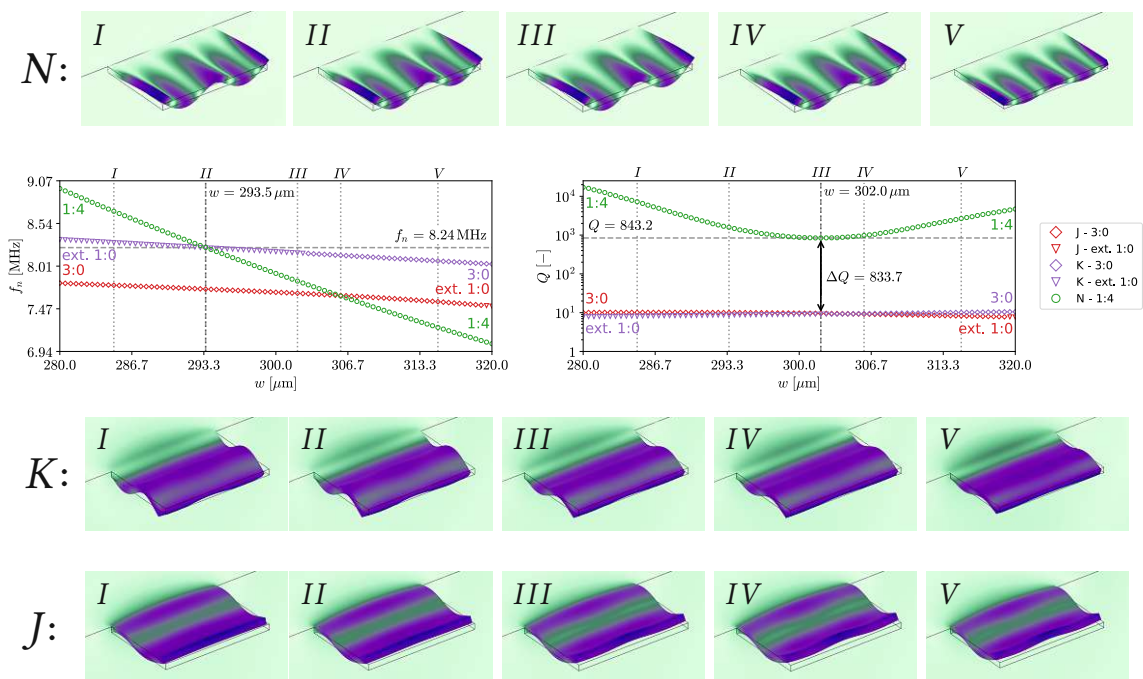


Figure 4.34: Crossing of the paths J , K , and N : The graph in the middle at left shows the natural frequency (f_n), and the graph at middle right shows the Q-factor (Q). The pictures above and below show the displacement patterns at the widths I to V . Above for the path N , below in the upper row the path K and in the lower the path J .

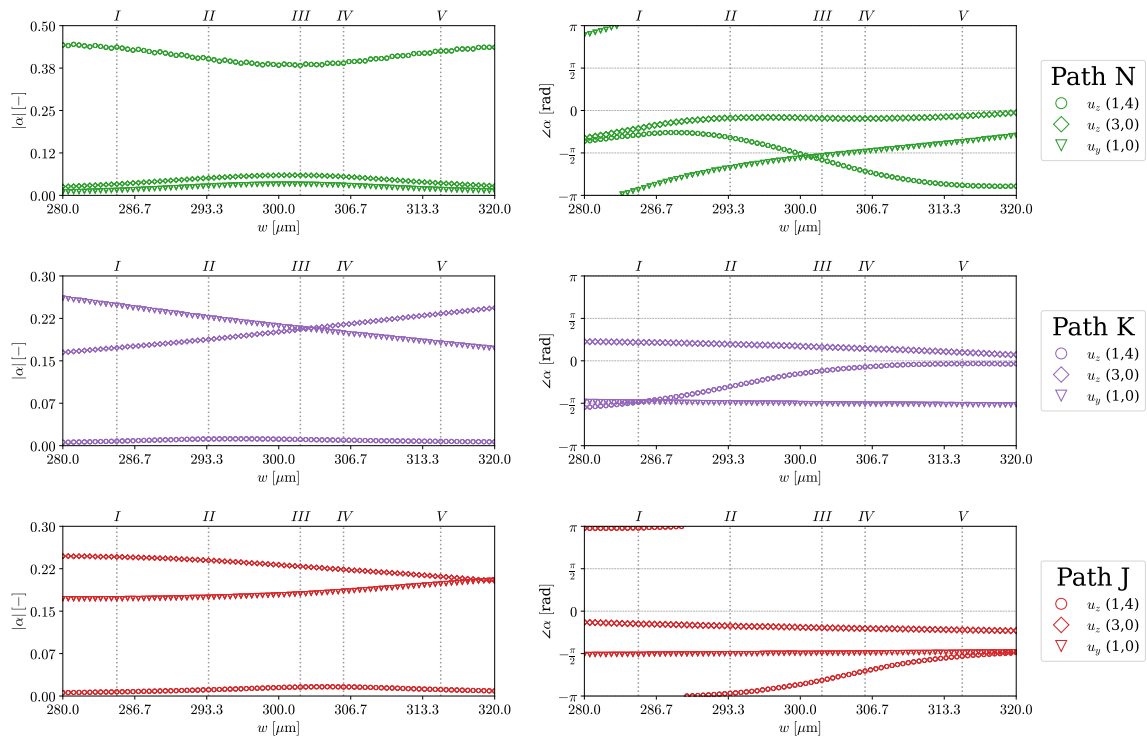


Figure 4.35: The complex amplitudes of the nodal numbers $u_z(1,4)$, $u_z(3,0)$ and $u_y(1,0)$ resulting from the FT-based method spitted in amplitude at left and phase at right. Above is shown the path N, in the middle the path K, and below the path J.

are shown in the next row. The amplitude plot shows that the nodal number $u_z(1,4)$ is very small, like in the plot above. The two other amplitudes cross right before the end of the interval at $319 \mu\text{m}$. Above this width, path J is classified as the extensional 1:0 mode shape. The phases of the crossing mode shapes are also, in this plot, rather constant, but the distance is here less than $\pi/2$. The phase for the nodal number $u_z(1,4)$ shows the opposite trend related to the nodal number $u_y(1,0)$ as for path K. It starts with a difference of $\pi/2$, and at the end, it is in-phase.

With the amplitude and phase information, it is possible to identify the interactions between these paths. The path N is influenced by both other mode shape components of both other paths. The phase has a strong relation between the 1:4 component and the

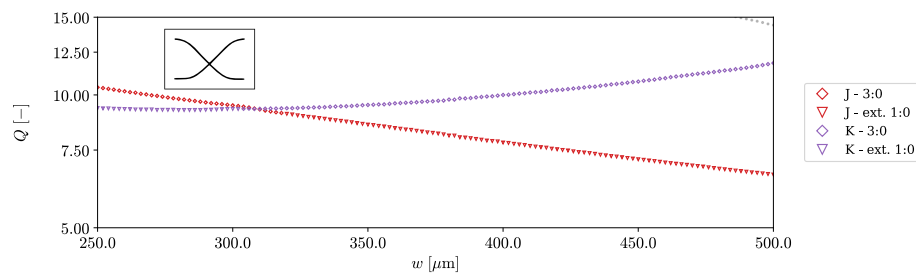


Figure 4.36: The quality factor during avoided crossing for the paths J and K.

extensional 1:0 component. However, the nodal number's amplitude $u_z(3,0)$ is slightly stronger, affecting the mode shape more significantly. Furthermore, it is visible in the amplitude plots of the path J and K that they exhibit avoided crossing right in this interval. Figure 4.36 shows the crossing in Q-factor these paths.

"Q-drop" crossing on path Q

Figure 4.37 show the path Q . On the whole path, the mode shapes were identified as a 1:5 mode. At the plate width of $340\ \mu\text{m}$, it appears in the plot for the first time with a natural frequency below $10\ \text{MHz}$. The Q-factor curve shows a strong drop at around $380\ \mu\text{m}$. Inspecting the natural frequency paths shows that curve veering can be excluded as the reason. To identify the interfering mode shapes, the FT method is applied to the three displacement components at the plate width of $380\ \mu\text{m}$. Figure 4.38 shows the nodal line count matrices. Three other significant modal numbers were identified. Only for the nodal number $u_z(3,1)$, a mode shape occur in this region. The 3:1 mode is identified in this region on path M . The amplitudes of the IP mode shape refer to a resonator bulk mode. However, no corresponding mode shape is identified in the surroundings. Therefore, only the paths Q and M are analyzed with a higher step resolution.

Figure 4.39 shows the natural frequency plot, the Q-factor plot from this simulation, and the displacement patterns for both paths. For the 1:5 mode shape is visible in the Q-factor plot at the left, a strong decrease of around two orders of magnitude, followed by an increase of more than two orders of magnitude. For the 3:1 mode on the lower curve, the Q-factor does not change significantly. Only a small increase between the width markers II and IV is visible. At the width III , where the natural frequencies

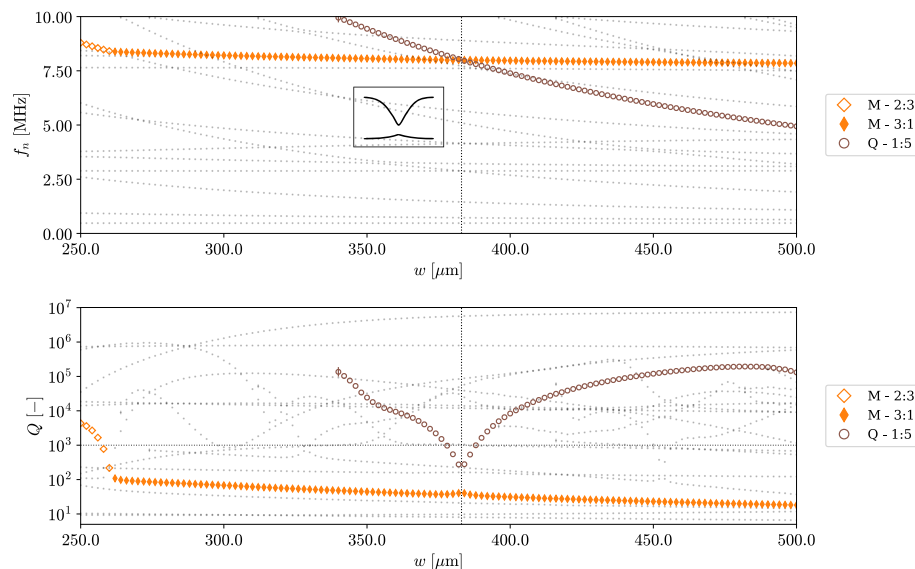


Figure 4.37: Plots of the natural frequency (f_n) and the quality factor (Q) for paths M and Q . The width of the minimum of path Q is marked with a dotted line. The \circ marker identifies the 1:5 mode, the \diamond marker the 2:3 mode, and the \blacklozenge marker the 3:1 mode. The first occurring point of path Q is marked with $|$ over the marker.

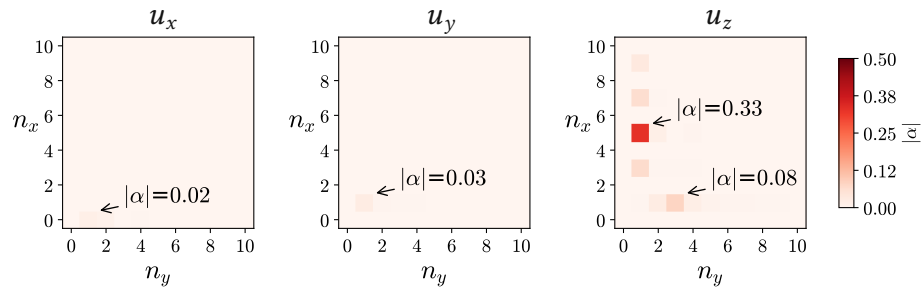


Figure 4.38: Plot of the amplitudes $|\alpha|$ identified from FT method, applied to the three displacement components of path Q at $380 \mu\text{m}$

cross, the gap in the Q-factor is very high. The lower quality factor is around 30, while the upper one has its minimum at 220. In the displacement patterns, it is visible that both paths are affected significantly only at the widths III and IV . In the other widths, no deviation from the expected mode shape aspects can be identified.

Figure 4.40 shows the amplitudes and phases for both paths for the identified nodal numbers. At the right in the amplitude plots in the upper, it is visible that both OOP nodal numbers decrease and increase respectively around width III . The IP nodal numbers $u_x(1,0)$ and $u_y(1,1)$ appear with smaller amplitudes as the nodal number $u_z(3,1)$ between the markers II and IV . The lower plot shows that the amplitude of the nodal number $u_z(3,1)$ is not decreasing as much as the nodal number $u_z(1,5)$ in the upper figure. The IP nodal numbers in the plot for path M show an amplitude around the nodal number $u_z(1,5)$ at width III . The phase plots are shown on the left. In both plots, the phases of the IP mode shapes are constant slightly above $-\pi/2$. The nodal number

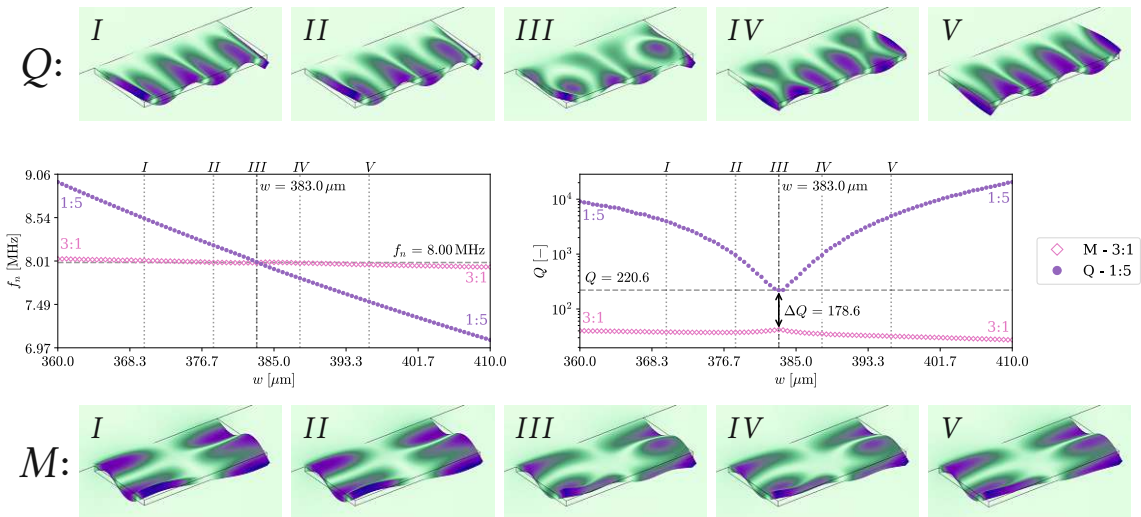


Figure 4.39: Crossing of path M and Q : The graph in the middle at left shows the natural frequency (f_n), and the graph at middle right shows the Q-factor (Q). The pictures above and below show the displacement patterns at the widths I to V . Above for the path Q , below for path M

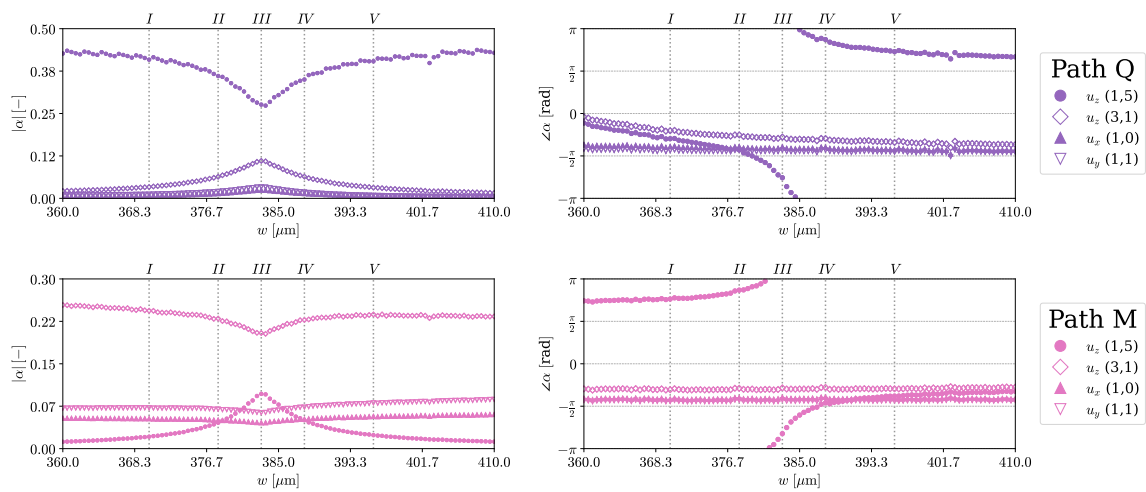


Figure 4.40: The complex amplitudes 1:5 and 3:1 from FT result matrices spitted in modulus at left and argument at right. Above is shown the path M and below the path Q.

$u_z(3,1)$ shows a phase change on both paths. On path Q, the OOP mode shapes are initially in phase, with a small difference, and both decrease slightly. From the width I, the phase of the nodal number $u_z(3,1)$ begins to change sign, while the 1:5 mode shape continues to decrease slightly. After the width III, the sign of the nodal number $u_z(3,1)$ phase is changed, and at the width V, it becomes stable again. The OOP mode shapes are then out of phase of around π . The plot below shows the opposite phase signs for the nodal number $u_z(1,5)$ on path M. The mode shapes are initially out of phase and at the end in phase. The phase of the nodal number $u_z(1,5)$ remains stable slightly below $-\pi/4$ and close to the value of the IP mode shapes for the plotted interval. The nodal number $u_z(3,1)$ changes the sign of the phase slightly before the width III.

As in the second example, a phase of the higher Q-factor path is also changed around the crossing of the natural frequencies. This phase change seems strongly related to the drop in the quality factor. Furthermore, the participation of the IP mode shapes seems also to be fundamental for "Q-drop" crossing.

Further interfering mode shapes

Four other regions of mode shape interference are identified in the analyzed interval. These results are shown in Appendix B. Two avoided crossings [B.1, B.3] are showing an increase in the phase difference for the detected mode shapes in the center of mode veering. This phase difference leads to moving displacement maxima during the oscillation period. For the shown "Q-drop" crossing could not be identified the interfering path [B.2]. This path may have a significantly low Q-factor (<5) and therefore is not detectable.

4.2.3 Comparison of anisotropic silicon and polycrystalline silicon

A smaller region is simulated with polycrystalline silicon to compare the behavior of different morphologies structures. The detailed results are shown in Appendix C. The resonance frequencies are significantly changed only for the second-order OOP mode shapes. It is also notable that the minimum distance in frequency for avoided crossings is doubled or more. Comparing the Q-factor plots shows that the RTS mode shapes are affected by a stronger decrease, while the EB mode shapes and other HO-OOP modes are unaffected.

4.2.4 Summary of interfering mode shapes

Table 4.3 summarizes the interference regions with the interacting paths and appearing mode shapes. The mode shapes appearing twice in the table are highlighted. Avoided crossing and "Q-drop" crossing are not limited to single-mode shapes. Some modes are capable of interacting, and others do simple crossing. Avoided crossing and "Q-drop" crossing are widely present phenomena. Figure 4.41 shows all paths where avoided crossing or "Q-drop" crossing is identified, with annotated index from Table 4.3.







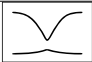
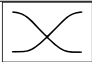
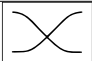
Index	Interference Type	Paths	OOP 1st order	OOP 2nd order	OOP 3rd order	IP mode	Ref.
(a)		$E+H$	1:3	2:1			4.2.1
(b)		$F+H$	1:3			1st lat	4.2.1
(c)		$G+N$	1:4	2:2			4.2.2
(d)		$N+J+K$	1:4		3:0	1st ext.	4.2.2
(e)		$M+Q$	1:5		3:1		4.2.2
(f)		$L+M$		2:3	3:1		B.1
(g)		S	1:6				B.2
(h)		$P+S$	1:6		3:2		B.3
(i)		$O+P$		2:4	3:2		B.4

Table 4.3: Mode shape groups with interference

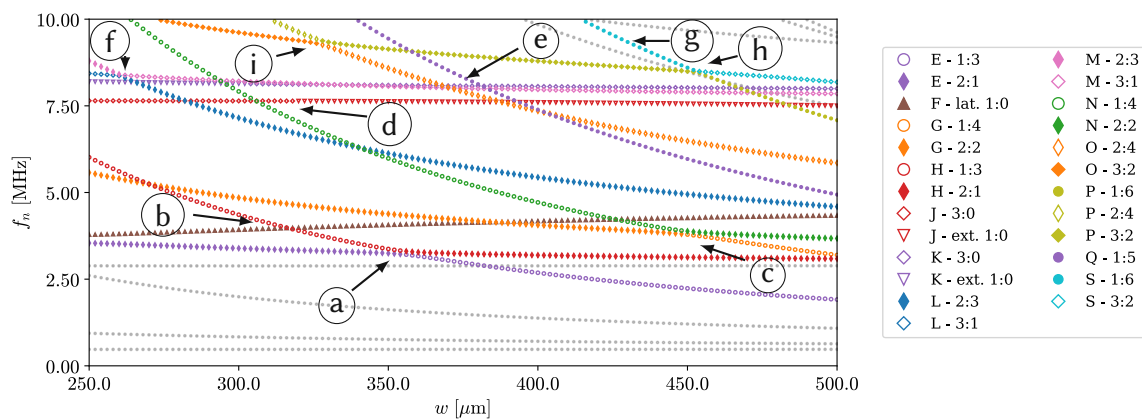


Figure 4.41: Plot of all paths with identified mode shape interference.

4.3 Conclusions

In chapter 3, it is identified that some RTS modes have lower quality factors than expected. In order to analyze the behavior of the Q-factor when the plate width is increased, a smaller increase in width must be investigated over a larger interval. Therefore, a simulation is performed of 126 plates within the interval from 250 μm to 500 μm . For the mode shape identification, a method based on the FT was developed to characterize all found resonance frequencies below 10 MHz and a quality factor above 5. Many mode shapes are affected by the decrease and increase of the Q-factor in some regions. As the major phenomenon for interfering OOP mode shapes is identified avoided crossing. However, not all Q-factor changes can be explained with curve veering. Sharp drops in Q-factor also appear while OOP mode shapes cross with other modes. These cases are identified as "Q-drop" crossings. The mode shape of this crossing OOP mode is not affected. Only its quality factor shows a significant drop. This interference type always presents small but significant amplitudes of IP nodal numbers in the nodal line matrices of the OOP mode shape. Not in every case is it possible to find an IP mode shape for the IP nodal numbers. However, if the related IP mode shapes are found, they are not affected by the Q-factor or displacement pattern from the interference. This interference pattern is not limited to two modes. In one case, a "Q-dropping" OOP mode shape is identified as interfering with another OOP mode and an IP mode. These two other mode shapes are in avoided crossing among "Q-drop" crossing. This example is the only observed avoided crossing between IP and OOP modes. In another example, this phenomenon is identified when two OOP mode shapes cross. The "Q-drop" affects only one mode, while the other one shows a slight increase. The nodal line matrices of both mode shapes reveal two significant IP nodal numbers. The OOP nodal numbers amplitudes show a comparable behavior to that of avoided crossing. However, the mode shape transition does not take place. Avoided and "Q-drop" crossings modify the quality factor over large width intervals. Therefore, the Q-factor is much lower at many plate widths, as expected from an analytic perspective.

The comparison between anisotropic single-crystalline and polycrystalline silicon

demonstrates that the presented mode shape interference patterns are relevant, depending on morphologic structures.

5 Conclusions and outlook

This investigation on crossing phenomena in non-slender MEMS resonators demonstrated the influence of anchor losses and the related quality factors. With the presented method for mode shape analysis, it is possible to analyze a displacement pattern and measure how many mode shapes the pattern is composed. This Fourier transformation-based method showed its potential not only by quantifying the strength of the different amplitudes but also by the phase of the underlying mode shapes. Three different kinds of frequency crossing are identified, shown in Table 5.1. The first row corresponds to simple crossing, where the mode shapes and their quality factors are not affected by the crossing of resonance frequencies. In the following rows, avoided crossing and simple crossing are described. Both phenomena have a strong effect on the quality factor.

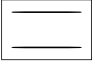
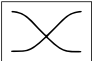
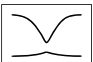
Phenomena	$f_n(\omega)$	$Q(\omega)$	Mode shape	Symbol
Simple crossing	Crossing	not changed	No interference	
Avoided crossing	Not crossing	Decreasing / increasing	Superposition	
"Q-drop" crossing	Crossing	Dropping / not changed	Small interference	

Table 5.1: Mode shape interference phenomenon on plate resonators

Within OOP modes, avoided crossing is identified as the prevalent interference pattern. This interference causes the transfer of mode shapes from one resonant frequency path to another. At the width with minimum distance in frequency, the interacting mode shapes superpose, generating complex displacement patterns. These patterns can have blended or circular nodal lines, and moving maximum peaks also occur due to phase shifts between the underlying mode shapes. The quality factors of the involved modes differ significantly, ranging from one to several orders of magnitude. During the avoided crossing, the Q-factors of the mode shapes are exchanged. The second identified interference pattern is the so-called "Q-drop" crossing. It is found in the region where the resonance frequencies of OOP mode shapes intersect with other compatible mode shapes. During the crossing, the displacement patterns of the modes are not superposed. However, the higher Q-factor of the OOP mode decreases drastically. Although this phenomenon is found at crossing between OOP mode shapes, the FT-based method always showed significant amplitudes of IP mode shapes. "Q-drop" crossing of an OOP mode is also observed with an IP mode shape in avoided crossing with another OOP mode shape. Further research is needed to understand the influence of IP mode shapes with extremely low Q-factors on OOP modes with high factors. Last but not least, it is shown that these interference phenomena also occur in polycrystalline

silicon. Even if the resonance frequencies and Q-factors slightly differ from anisotropic silicon, the same crossing phenomena are identified.

These phenomena identified from theoretical investigation help explain Q-factor variations in previous experimental works, where small changes in the resonator width yield a massive reduction in Q-factor [21]. Furthermore, this investigation opens new sensing strategies based on the highly responsive phenomena of avoided crossing and "Q-drop" crossing.

Appendix

A Definition of the exported Data from *Comsol Multiphysics*

For the export, it is necessary to specify a group of points on the resonator. On the defined surface from Figure 4.4, the displacement is evaluated on a regular grid with $1\ \mu\text{m}$ steps for the x - and y -directions.

For the visualization, the displacement vectors $\mathbf{u}(\mathbf{x})$ for all points $\mathbf{x} = (x, y, 0)$ on the grid are transformed from complex values to the time-dependend form, with

$$\mathbf{u}(x, y, \theta) = \Re(\mathbf{u}(x, y)) \cdot \cos(\theta) - \Im(\mathbf{u}(x, y)) \cdot \sin(\theta), \quad (1)$$

where θ is the oscillation phase of the resonator, defined as $\theta = 2\pi f_n t$ with the natural frequency f_n and the time t . For the plots, the moment where the surface shows the maximum displacement is used.

Further, for the visualization of the displacement, for each element on the grid are calculated the displaced filed position $\mathbf{d}(\mathbf{x})$, with

$$\mathbf{d}(\mathbf{x}) = \mathbf{x} + s \cdot \mathbf{u}(\mathbf{x}), \quad (2)$$

where \mathbf{x} is the initial position of the element on the grid, \mathbf{u} is the complex displacement vector, and s the scaling factor for the visualization of the displacement.

B Interfering mode shapes

In this section, the remaining regions of mode shape interference are analyzed for these geometries below a resonance frequency of 10 MHz.

B.1 Avoided crossing between path L and M

Figure 1 shows at this width interval the curve veering between path M and L . Besides the strong gradient change, this is very hard to identify in the natural frequencies plot. Figure 2 shows that the eigenfrequencies bypass each other, although they are only distant 44.7 kHz at width III . The areas 1 and 2 both have more than twice the distance. Also, the interval is very short, with approximately $15\ \mu\text{m}$ from width I to width V compared to these other areas. The behavior of this avoided crossing is similar to the zone 1. Figure 3 is also comparable with the curve veering in area 1. The only notable differences are the dips for the phase of the 2:3 mode in both plots. The sign has no change, so it can not be identified in the displacement patterns of Figure 2. To demonstrate how these phase changes are affecting the displacement patterns, the plate oscillation in time will be discussed. The data is calculated from equation 1.

Figure 4 shows the displacement patterns of path M for the widths I , II , and III at different moments in time. In the first row at width I , in all images, the 2:3 mode shape is visible. In column 4, the smallest displacement is visible as a very bright image. The mode shape is also more curved than in the other plots, which is caused by interfering with the second mode shape. In the following image, the sign of displace-

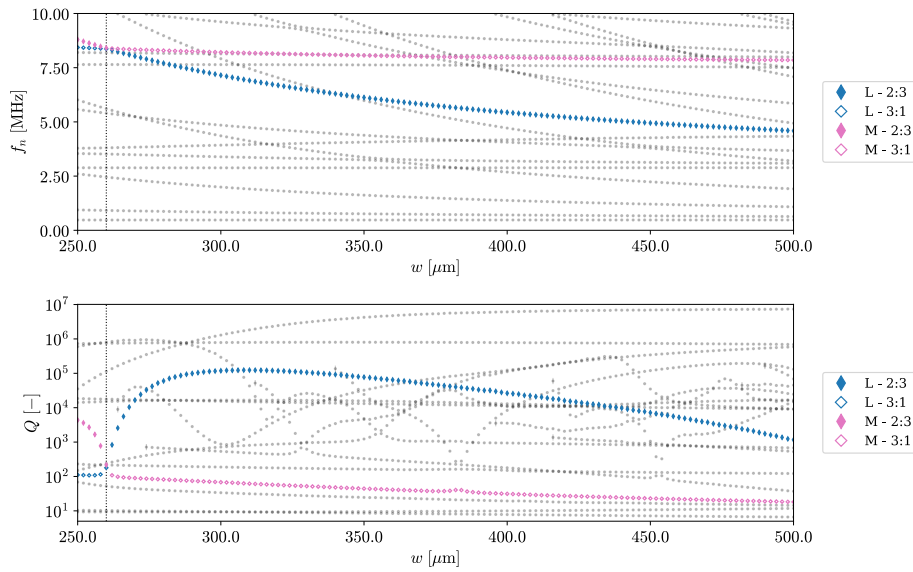


Figure 1: Plots of the natural frequency (f_n) and the quality factor (Q) for paths L and M . The \blacklozenge marker identifies the 2:3 mode and the \diamond marker the 3:1 mode.

ment is changed. Therefore, between these moments, the 2:3 displacement amplitude must be zero. In the second row, only in column 5 is the 3:1 mode visible. Therefore, it can be estimated that the zero displacement for the 2:3 mode shape is located near $\omega t = \pi/2$. Between $\omega t = \pi/4$ and $3\pi/4$, the nodal lines move on the plate, and no simple up-and-down oscillation is visible. From nodal line movement, it can be estimated that the amplitude of the 3:1 mode is zero between columns 3 and 4. This is expected when

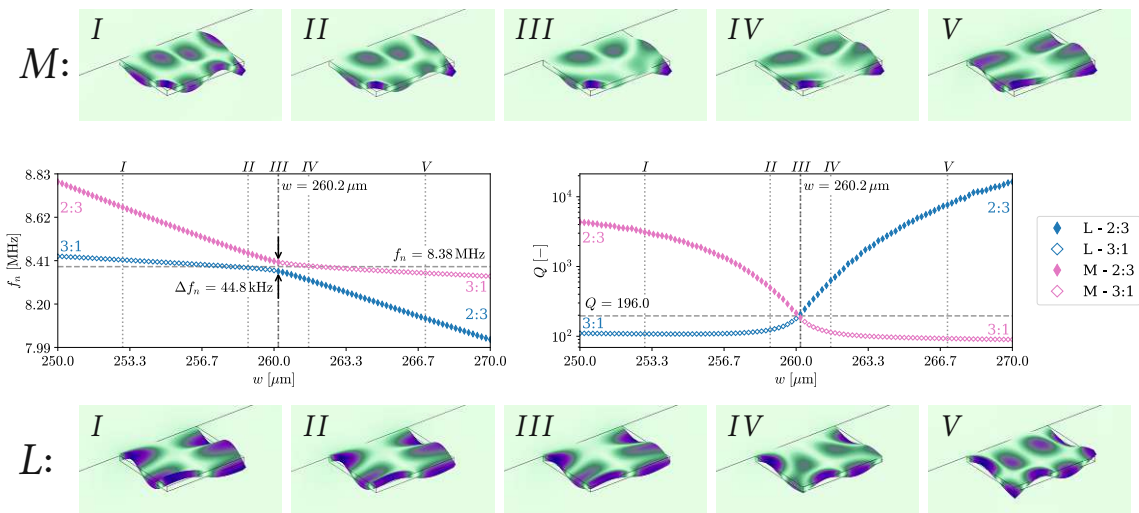


Figure 2: Avoided-crossing of path L and M : The graph in the middle at left shows the natural frequency (f_n), and the graph at middle right shows the Q-factor (Q). The pictures above and below show the displacement patterns at the widths I to V . Above for the path M , below for path L

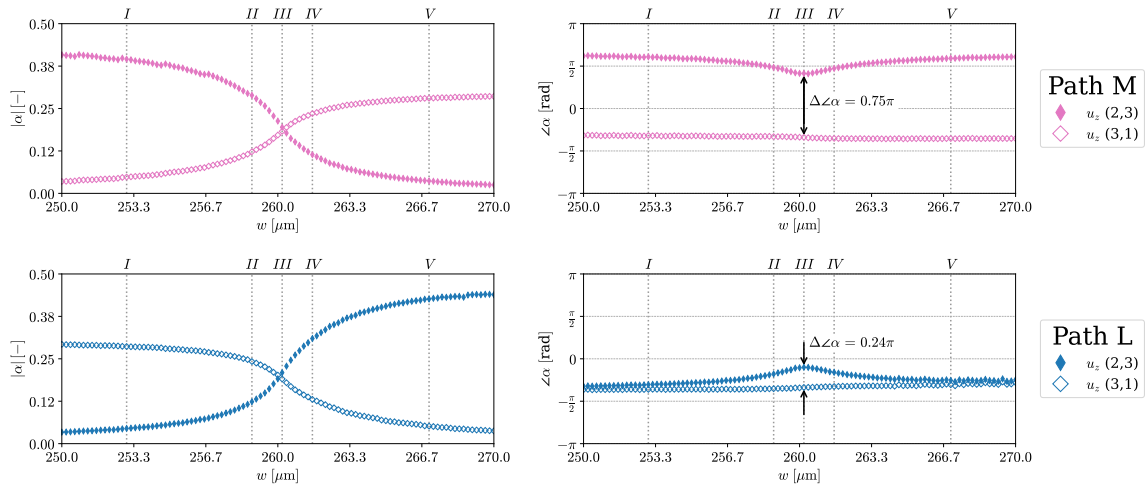


Figure 3: The complex amplitudes of the nodal numbers $u_z(2,3)$ and $u_z(3,1)$ from the nodal line count matrix spitted in modulus at left and argument at right. Above is shown the path L and below the path M.

the 2:3 mode shape has straight nodal lines between the edges. At the third width, the amplitudes $|\alpha|$ for both modes have the same strength, as visible in Figure 3 in the upper right plot. The zero displacement for the 3:1 mode is expected at the same moment as in the widths I and II because its phase is stable. The phase difference is at this width at its minimum. However, the zero displacement appears with a distance of π , so the distance can be interpreted as $-\pi/4$. The zero displacement for the 2:3 mode is estimated between columns 5 and 6. This shows that the distance in the phase plot matches the estimation from visual analysis. Figure 5 shows in the first row the displacements in time at the width I.

From Figure 3, it is known that the amplitude for the 3:1 mode dominates and both phases are around $-\pi/3$. The minimum displacement is visible in column 4, at the same position as in the path above. This is also the only moment where the 3:1 mode does not appear. This mode shape can not be classified, but it leads to the conclusion that a second mode shape is involved. Due to the slight deviation in phase, the nodal lines are moving at tiny displacements. At width II, the minimum displacement is stronger than before. At this width, the contribution from the 2:3 mode is more visible due to the higher amplitude and the larger phase shift. Also, in column 5, this interference can be seen in the nodal line movement. At width III, where the amplitudes are equal, it no longer dominates the 1:3 mode. While this mode shape is visible in columns 1, 2, 8, and 9, in columns 4, 5, and 6, the 2:3 mode dominates. At $\omega t = \pi/8$, the 1:3 mode appears very clear. This leads to the conclusion that the 2:3 mode has there zero displacement. At $\omega t = 3\pi/8$ is the opposite situation. Therefore, it can be estimated that the 1:3 amplitude here is zero. Then the distance in phase should be around $\pi/4$, the same value as marked in Figure 3 in the lower phase plot.

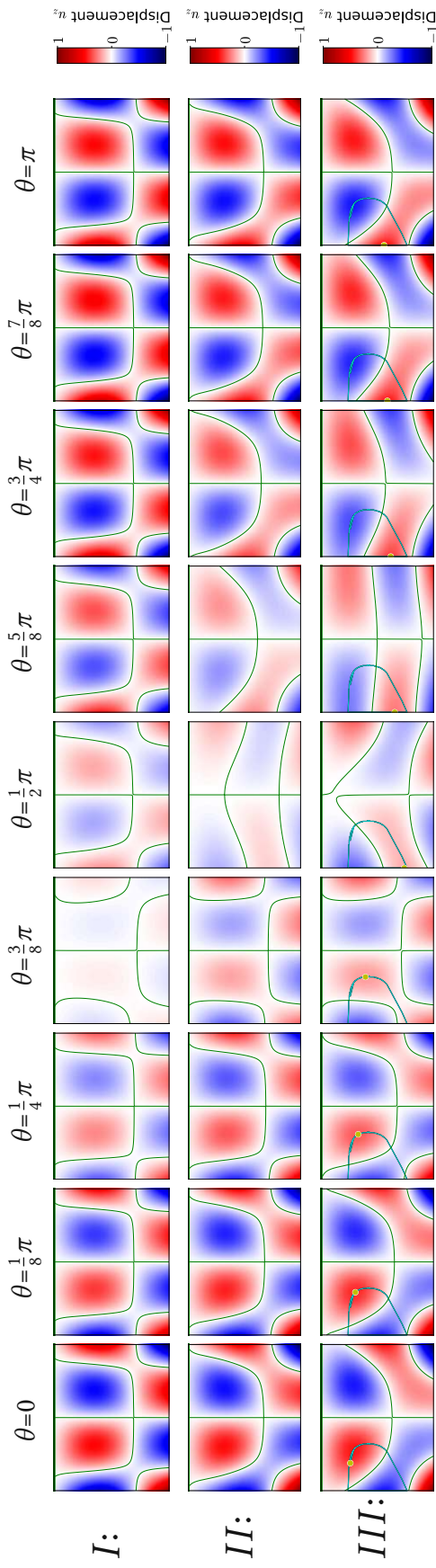


Figure 4: 2D plot of the OOP displacement component u_z for path M in the first half period, derived from complex displacement with Equation 1. Each row shows one width of the widths I , II , and III .

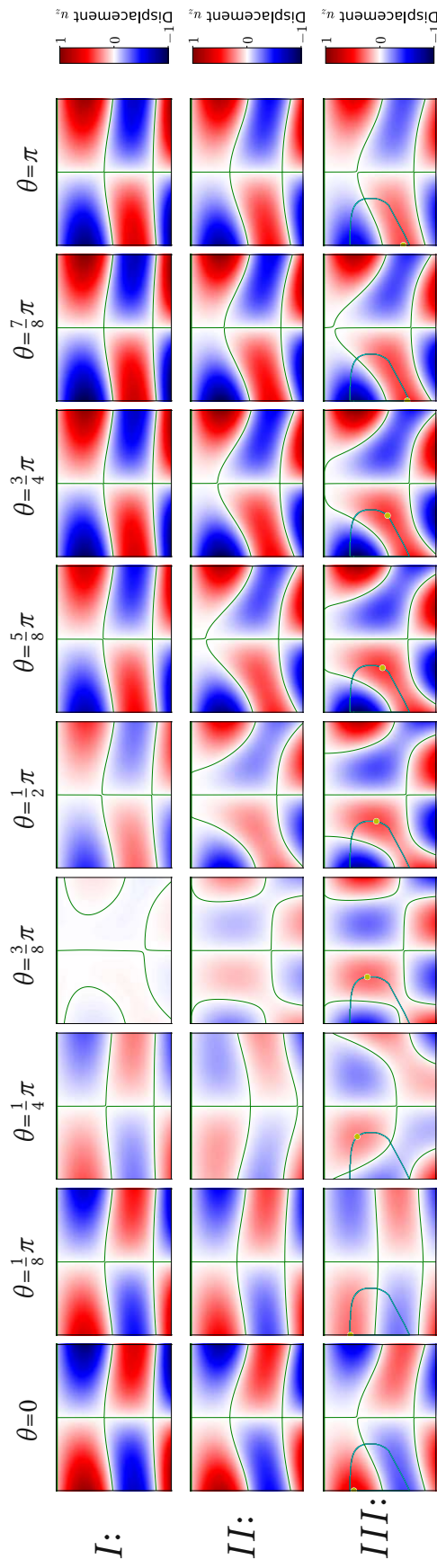


Figure 5: 2D plot of the OOP displacement component u_z for path L in the first half period, derived from complex displacement with Equation 1. Each row shows one width of the widths I , II , and III .

B.2 "Q-drop" crossing on path S

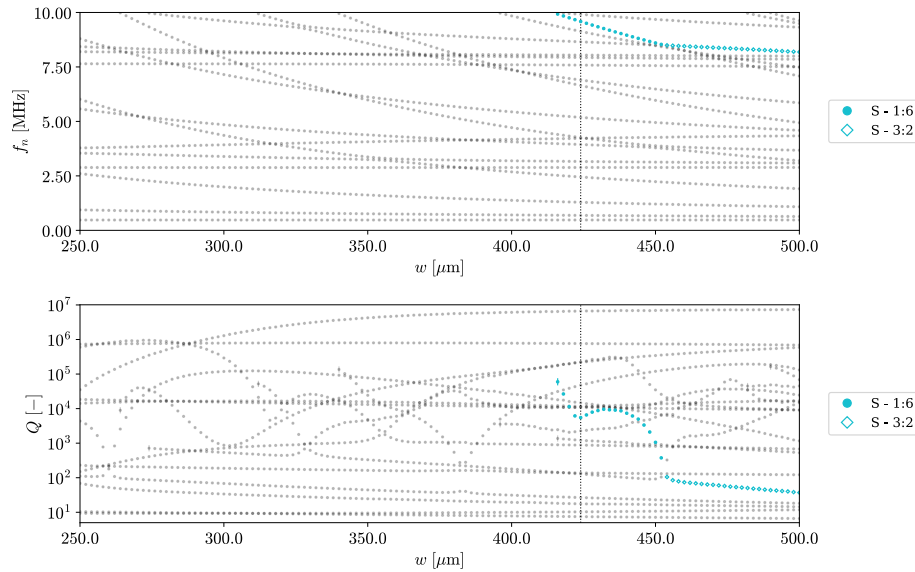


Figure 6: Plots of the natural frequency (f_n) and the quality factor (Q) for path S . The \bullet marker identifies the 1:6 mode and the \diamond marker the 3:2 mode. The first occurring point of the path is marked with $|$ over the marker.

Figure 13 shows two regions where a significant drop appears. The first drop is marked in the figure at its minimum Q-factor at $424 \mu\text{m}$. Figure 7 shows the result of the FT-based method at the plate widths around the minimum. Besides the strong amplitude for the nodal number $u_z(1,6)$, two IP nodal numbers also appear. No displacement pattern with these mode shapes is found in the surroundings. IP mode types tend to have low Q-factor. Therefore, this mode shape may not appear in the simulation results.

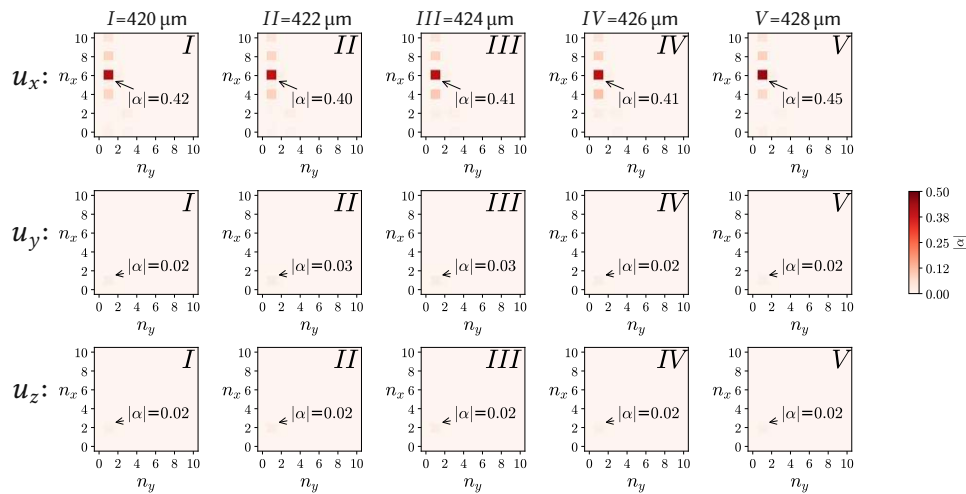


Figure 7: Plot of the amplitudes $|\alpha|$ identified from FT method, applied to the three displacement components of path S at the widths $420 \mu\text{m}$, $422 \mu\text{m}$, $424 \mu\text{m}$, $426 \mu\text{m}$, $428 \mu\text{m}$

B.3 Avoided crossing between path P and S

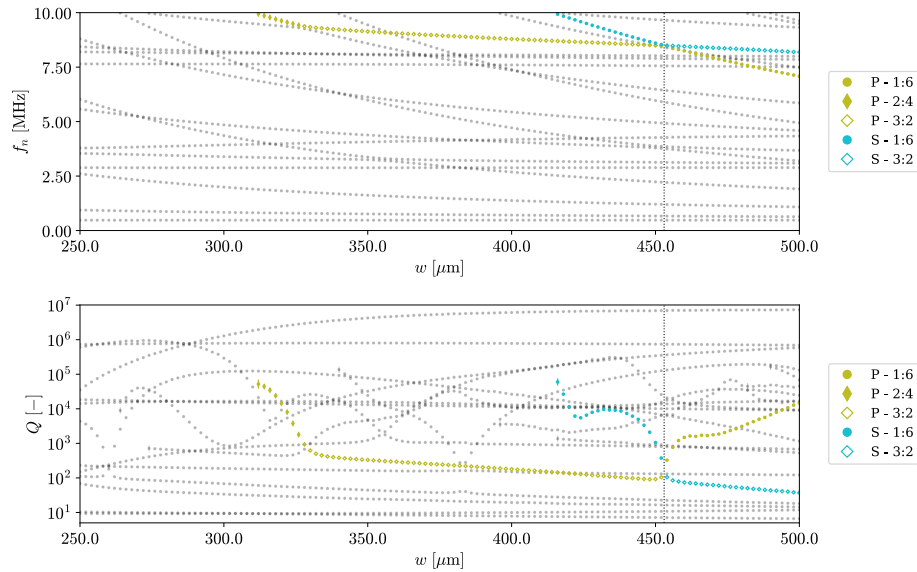


Figure 8: Plots of the natural frequency (f_n) and the quality factor (Q) for paths P and S . The \bullet marker identifies the 1:6 mode, the \blacklozenge marker the 2:4 mode, and the \blacklozenge the 3:2 mode. The first occurring points of the paths are marked with $|$ over the marker.

Figure 8 shows the avoided crossing between path P and S at slightly above $450 \mu\text{m}$. In the frequency plot, the region of non-crossing is not clearly visible. In more detail, it is shown in Figure 9. At the marked width III is annotated only 25.6 kHz distance

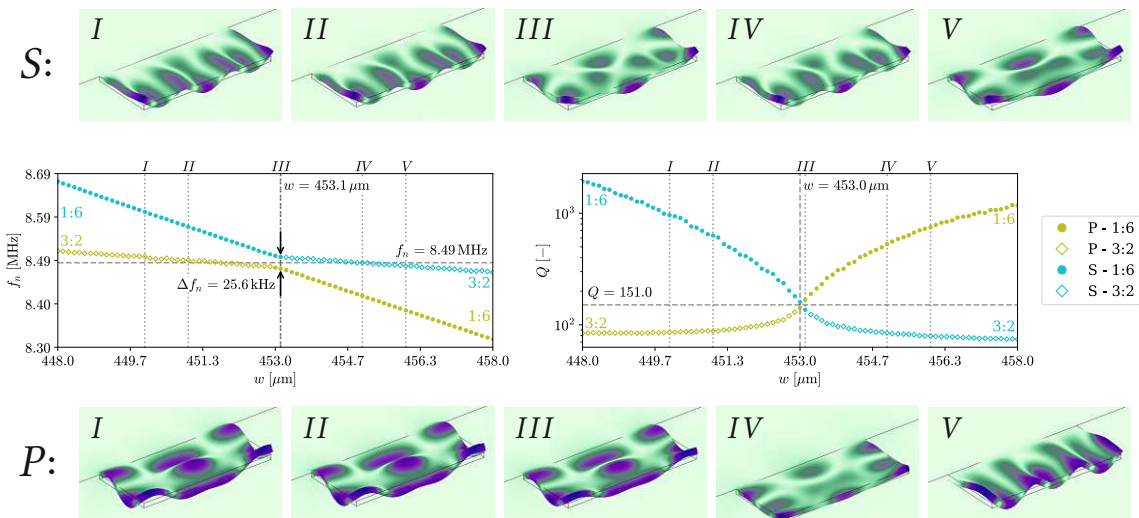


Figure 9: Avoided-crossing of path S and P : The graph in the middle at left shows the natural frequency (f_n), and the graph at middle right shows the Q -factor (Q). The pictures above and below show the displacement patterns at the widths I to V . Above for the path P , below for path S .

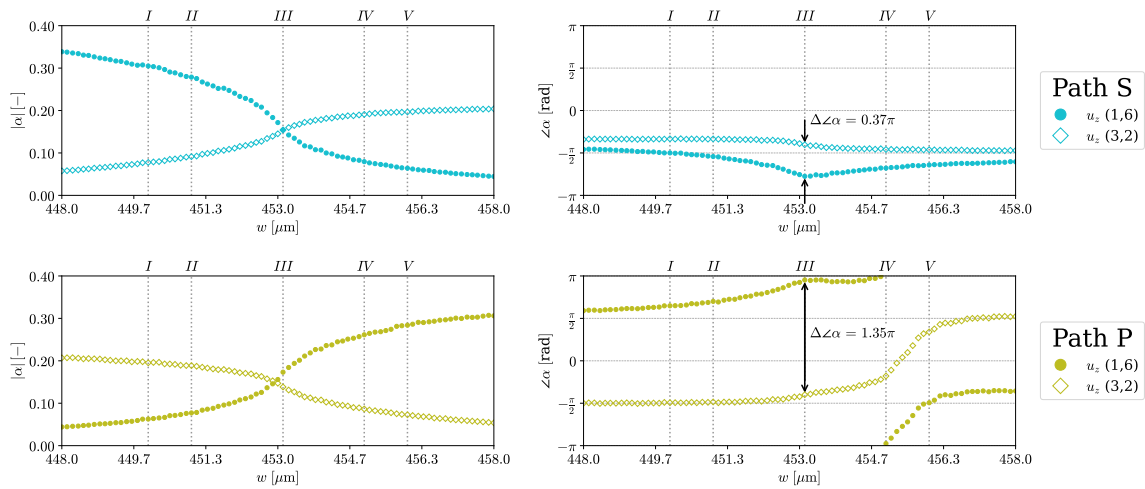


Figure 10: The complex amplitudes of the nodal numbers $u_z(1,6)$ and $u_y(3,2)$ from FT result matrices spitted in modulus at left and argument at right. Above is shown the path P and below the path S.

between the resonance frequencies. Although this, it looks in natural frequency and Q-factor very similar to the curve veering, shown in section 4.2.1. Only the intersection width of the Q-factor is located slightly before the closest distance in frequency. In the displacement patterns for path S above the graphs, the 1:6 mode can be identified in the first two images. In the third image, the appearing mode shape is somewhat complex and can not be described with nodal line count. At width IV, the displacement looks very similar to a 1:6 mode. The nodal lines starting from the anchor are curved, but all end at the free edge. However, the FT method assigned the 3:2 mode as the primary mode shape. At the last shown width, a 3:2 mode shape is clearly visible. In the lower images is shown path P. The displacement shown for the first three widths looks very similar, but the amplitude slightly decreases. At width, IV, the 3:2 mode can also be identified, but the deflection is heavily decreased. Like in the other path, the identified mode is different. It is detected as a 1:6 mode. In the last picture, the 1:6 mode shape is visible. Figure 10 shows for path S that the amplitudes $|\alpha|$ are quite different at the beginning. At the end of the plot, the amplitude of the stronger mode shape is not so high, while the lower maxima remain around the same value. Below in the figure for path P is the same behavior in the opposite directions. In the plots at right, the argument for both paths is shown. For path S, both modes are in phase, although having a slightly different phase. The highest deviation is at the width III. Also, it is visible that both are changing in absolute values. The lower graph for path P shows that the modes are out-of-phase. Also, the distance is not constant and different than π . Around the width IV, the phase for the 1:6 mode changes sign, and soon after, the phase for the 3:2 mode also changes. To analyze how the changes in phase affect the displacement patterns, Figure 11 and 12 show the mode shapes for both paths at different times for the width III, IV and V. It is visible that the nodal lines in the first row and the second row of each path, the nodal lines are highly moving and show rather complex mode shapes.

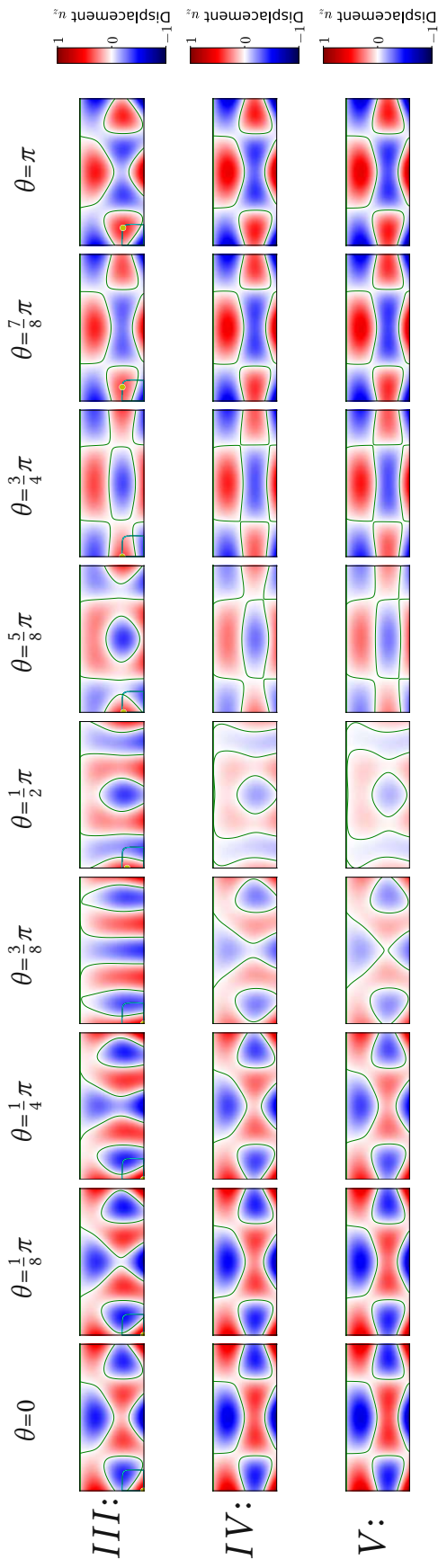


Figure 11: 2D plot of the OOP displacement component u_z for path S in the first half period, derived from complex displacement with Equation 1. Each row shows one width of the widths III , IV , and V .

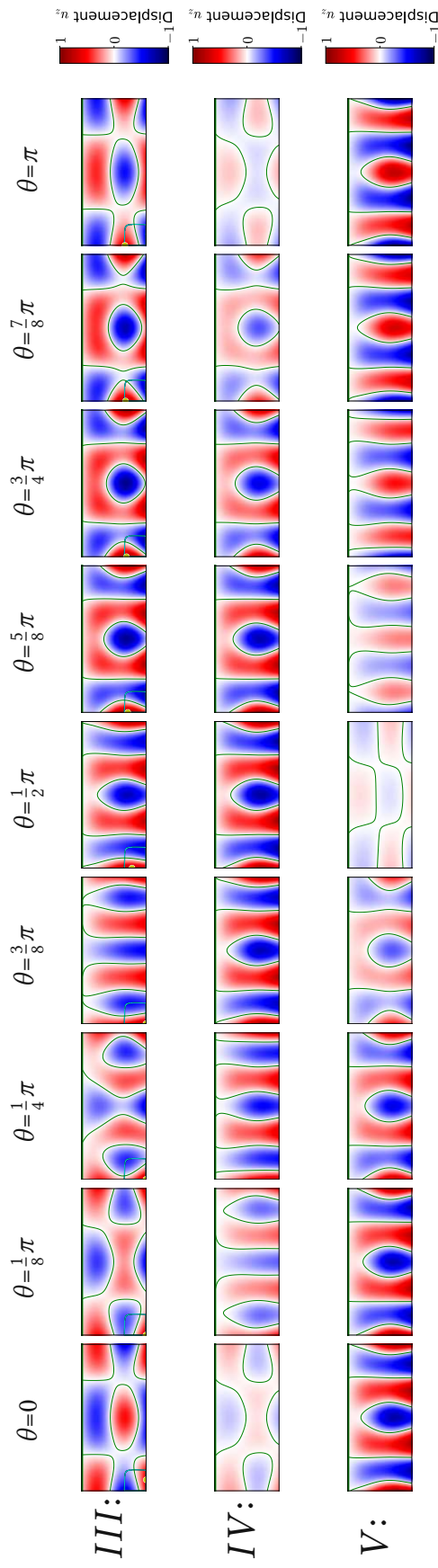


Figure 12: 2D plot of the OOP displacement component u_z for path P in the first half period, derived from complex displacement with Equation 1. Each row shows one width of the widths III , IV , and V .

For the width V , it is visible that the mode shapes are becoming more the shape of the stronger base mode. This demonstrates that differences in the phase lead to complex mode shapes and moving nodal lines during the oscillation.

B.4 Avoided crossing between path O and P

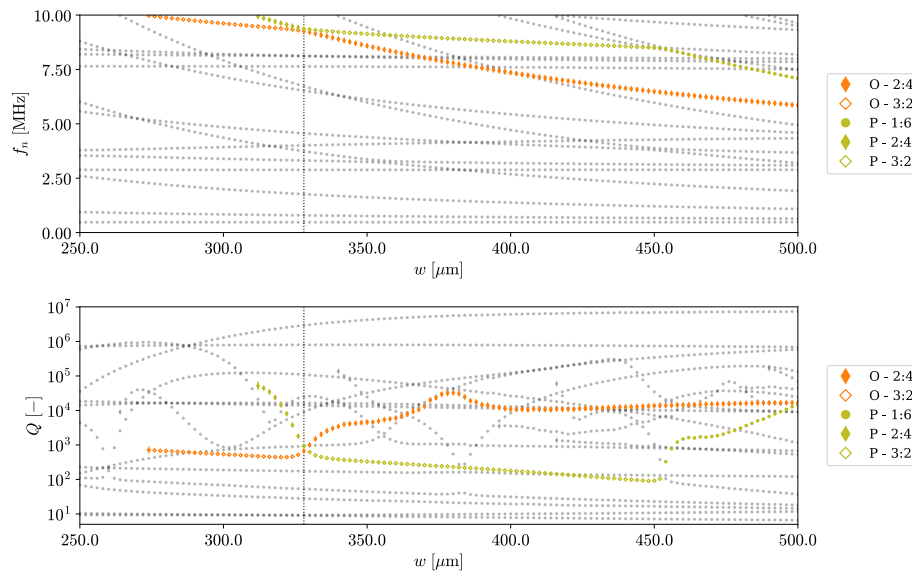


Figure 13: Plots of the natural frequency (f_n) and the quality factor (Q) for paths O and P . The \bullet marker identifies the 1:6 mode, the \blacklozenge marker the 2:4 mode, and the \blacklozenge the 3:2 mode. The first occurring points of the paths are marked with $|$ over the marker.

Figure 13 shows the avoided crossing for path O and P . In the region where the transition from one to the other path occurs, a significant increase in the quality factor is visible. This region will be analyzed in more detail. Figure 14 and 15 show the results of this simulation. The behavior of the paths is comparable to area 2. The shift of the Q-factors intersection is not so strong but also visible. The Q-Factor for the 2:4 mode is decreasing by almost one order of magnitude from the initial to the final value. As estimated in area 2, this seems to be the cause of the shifted crossing point of the quality factors. The displacement patterns show a smooth transition from one to the other mode shape. Also, the modulus and argument plots are very smooth in transition. The phases for path P are out-of-phase and changing signs at the same width. The distance is close to π and constant along the avoided crossing. The phases are in phase and very close for path O .

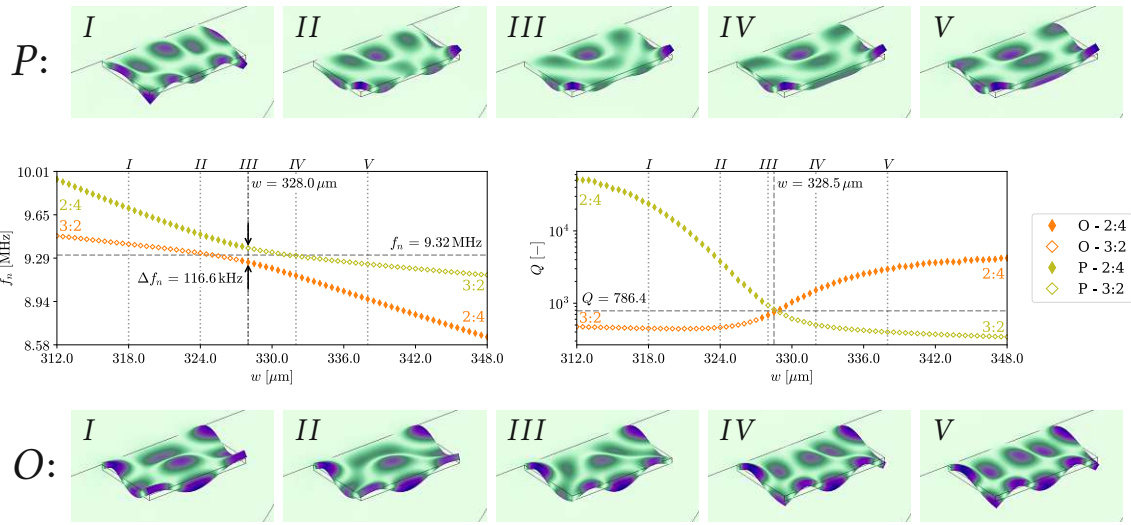


Figure 14: Avoided-crossing of path *O* and *P*: The graph in the middle at left shows the natural frequency (f_n), and the graph at middle right shows the Q-factor (Q). The pictures above and below show the displacement patterns at the widths *I* to *V*. Above for the path *P*, below for path *O*

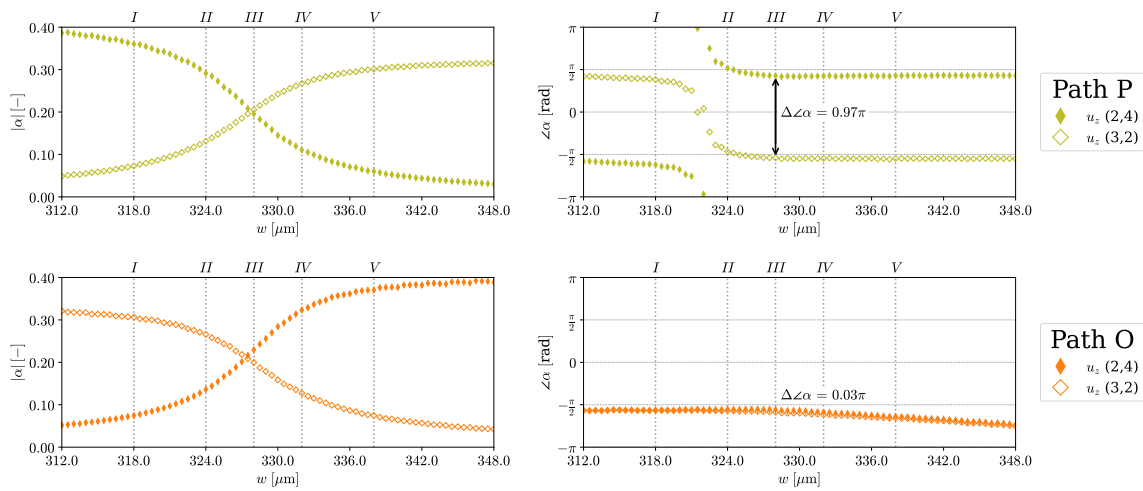


Figure 15: The complex amplitudes of the nodal numbers u_y (2,4) and u_y (3,2) from FT result matrices spitted in modulus at left and argument at right. Above is shown the path *P* and below the path *O*.

C Results polycrystalline silicon

The model is used as defined in Table 4.1. However, the material is changed to polycrystalline silicon from the Comsol Multiphysics MEMS material database.

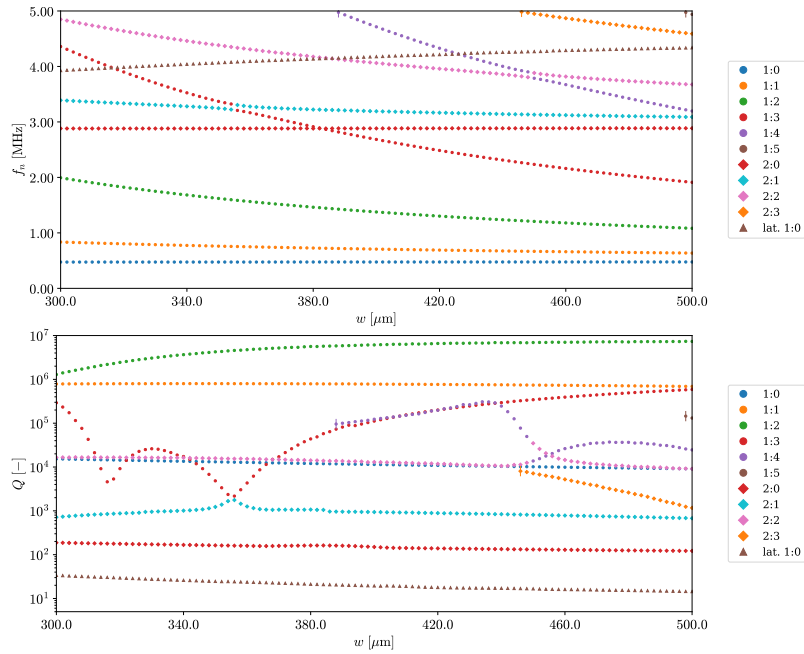


Figure 16: Plot of the natural frequencies and the quality factors for anisotropic silicon.

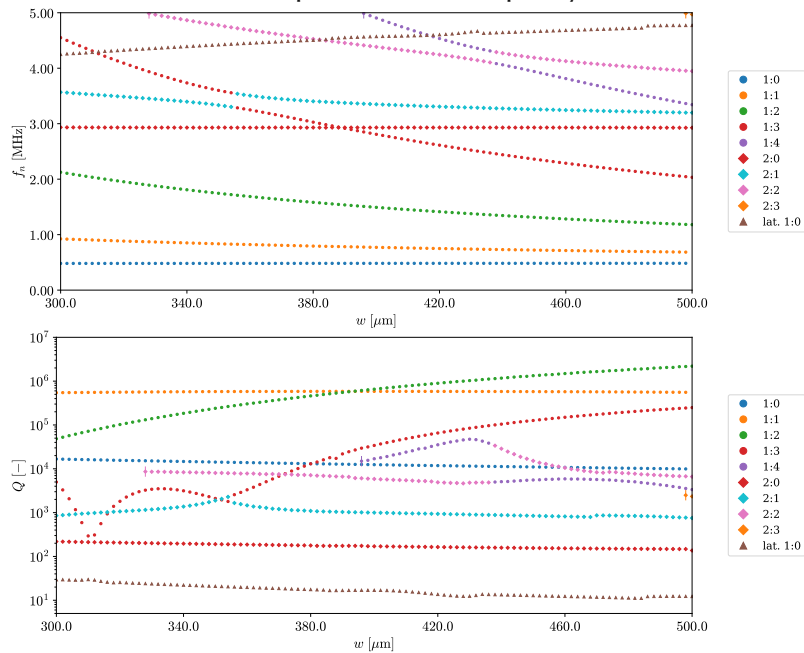


Figure 17: Plot of the natural frequencies and the quality factors for polycrystalline silicon.

List of Figures

1.1	Fabricated MEMS cantilevered plate resonator [14]	2
1.2	Measured quality factor of roof-tilde-shaped modes at different widths w of fabricated devices reported by Stixenberger [21]	2
2.1	Cantilever resonator, in a) in the non-excited state, and in b) excited in the 2nd Euler-Bernoulli mode	4
2.2	Natural frequency f_n of the EB modes for the first five eigenvalues for different lengths l . The resonator material properties and geometry are defined in Table 2.1	6
2.3	Total quality factor of the EB modes for the first five eigenvalues assuming isotropic silicon cantilevers with $w = 100 \mu\text{m}$, $h = 15 \mu\text{m}$ and different lengths l from the interval $100 \mu\text{m}$ to $1000 \mu\text{m}$	8
2.4	Total quality factor and as well as individual Q-factor contributions plotted over the frequency range of the first five EB mode shapes assuming isotropic silicon cantilevers with $w = 100 \mu\text{m}$, $h = 15 \mu\text{m}$ and different lengths l starting from $100 \mu\text{m}$ to $1000 \mu\text{m}$	9
2.5	Geometry of the half-sphere model	11
2.6	Convergence of mesh for the half-sphere model for the first EB mode. The red line is assigned to the left axis and shows the ratio of the Q-factor and the Q-factor with the finest mesh size over the number of mesh elements. The blue line is assigned to the right axis and shows the execution time. The green section marks the acceptable deviation of the ratio.	12
2.7	Half sphere model with defined mesh from COMSOL Multiphysics	13
2.8	Q-factor Q for anchor losses over resonance frequency f_n , in blue from the analytic solution and in red the simulation results of the FEM	13
2.9	Geometry of the quarter-sphere model	13
2.10	The Q-factor for anchor losses over the resonance frequency of the half-sphere and the quarter-sphere model	14
3.1	Geometries of the evaluated cantilevers	16
3.2	Examples for the different mode types on cantilever resonators	18
3.3	Types of out-of-plane mode shape on slender beam resonator.	19
3.4	Types of in-plane mode shape on slender beam resonator.	19
3.5	Occurring mode shapes for the slender beam resonator, showing the quality factor Q over the natural frequency f_n . The dashed lines delimit the region of promising mode shapes with resonant frequencies above 3 MHz and Q-factor above 10^3	20
3.6	Quarter sphere model: The section of the substrate evaluated for the mechanical energy flow is marked in green.	21
3.7	Radial mechanical energy flux for out-of-plane modes.	22
3.8	Radial mechanical energy flux for in-plane modes.	22

3.9	New appearing mode shapes for non-slender resonators. In a) the 3:4 HO-OOP mode shape and in b) an IP bulk mode.	23
3.10	Occurring mode shapes for the quadratic plate resonator, showing the quality factor Q over the natural frequency f_n . The dashed lines delimit the region of promising mode shapes with resonant frequencies above 3 MHz and Q-factor above 10^3	24
3.11	Radial mechanical energy flux for out-of-plane modes.	25
3.12	Radial mechanical energy flux for in-plane modes	25
3.13	Occurring mode shapes for the wider plate resonator, showing the quality factor Q over the natural frequency f_n . The dashed lines delimit the region of promising mode shapes with resonant frequencies above 3 MHz and Q-factor above 10^3	26
3.14	Radial mechanical energy flux for out-of-plane modes.	27
3.15	Radial mechanical energy flux for in-plane modes.	27
3.16	Radial mechanical energy flux for RTS modes.	28
4.1	Examples of the analyzed plate widths. In a) the smallest plate with 250 μm and in b) the widest plate with 500 μm	30
4.2	Result of the simulation sweep: The resonance frequencies f_n over the plate width w . Highlighted are all identified RTS modes. The other modes are in gray in the background. For some widths, the 1:3, 1:4, and 1:6 mode shapes cannot be identified. For the 1:3 mode, a zoom is shown in this area. The resonance frequencies in grey between the identified red dots show a repulsive trend.	31
4.3	Results of the simulation with increasing width. The natural frequencies are grouped by paths from A to V ordered by ascending frequency.	31
4.4	The plate, drawn as a wire body, with the axis orientation at the origin \mathcal{O} . The plane at half thickness marked in magenta is used for the data export.	32
4.5	Visualization of the 1:1 mode shape. In a) from <i>Comsol Multiphysics</i> and in b) the maximum displacement matrix $U_{z,max}$. The black tick line at $y = 0$ marks the anchor of the plate. In both images, the plate is 200 μm long and 250 μm wide.	33
4.6	a) The maximum displacement field U_z for a 1:1 mode as a heat map. b) Plot of the amplitudes $ \alpha $ for the wavenumbers of the displacement field U_z . Only a slice from the result matrix of the 2D DFT containing the first ten spacial oscillations in both directions is shown to ensure the visibility of the highest expected oscillation. It shows a maximum in $(\xi_y, \xi_x)=(0, 1)$. Each amplitude is normalized to the sum of all amplitudes in the first quadrant.	33
4.7	Steps from original to the extended displacement data for the 1:1 mode in a) along the free edge and b) along a lateral edge. Displacement is normalized and not in scale.	34
4.8	a) The extended dataset from U_z as a heat map. b) Slice of the result matrix from 2D DFT with the extended dataset	35

4.9	FT result matrices for the 2:3 mode, in a) the result matrix of the 2D-DFT with the extended data and in b) the nodal lines count matrix.	35
4.10	Transition mode shape: In a) the displacement pattern from <i>Comsol Multiphysics</i> , in b) the heat map of the displacement matrix U_z and in c) the nodal lines count matrix for the displacement component U_z	36
4.11	The 1:0 mode shape: The displacement pattern in a) and the nodal lines count matrix from displacement component U_x in b), from displacement component U_y in c), and from displacement component U_z in d).	36
4.12	The 1st lateral EB mode: The displacement pattern in a) and the nodal lines count matrix from displacement component U_x in b), from displacement component U_y in c), and from displacement component U_z in d).	36
4.13	The 1st extensional mode shape: The displacement pattern in a) and the nodal lines count matrix from displacement component U_x in b), from displacement component U_y in c), and from displacement component U_z in d).	37
4.14	The resonance frequencies (f_n), identified from the FT based method, of the sweep simulation sorted by the mode shapes. For paths that only have one mode shape, it is noted in the legend.	37
4.15	Plots of the natural frequency (f_n) and quality factor (Q) for the RTS modes. Different marks are used for different mode shapes. The first occurring point with a natural frequency below 10 MHz of each path is marked with over the marker. In the background, all other eigenmodes are shown in gray.	38
4.16	Plots of the natural frequency (f_n) and the quality factor (Q) for the 1:3 mode on the paths <i>E</i> and <i>H</i> . The • marker identifies the 1:6 mode and the ◊ marker the 3:2 mode.	39
4.17	Plots of the natural frequency (f_n) and the quality factor (Q) for paths <i>E</i> and <i>H</i> . The ○ marker identifies the 1:3 mode, and the ◆ marker the 2:1 mode.	40
4.18	Avoided-crossing of path <i>E</i> and <i>H</i> : The graph in the middle shows the natural frequency (f_n) over the plate width (w). The pictures above and below show the displacement patterns at the widths <i>I</i> to <i>V</i> , as marked in the plot. Above for the path <i>H</i> , below for path <i>E</i>	41
4.19	Avoided-crossing of path <i>E</i> and <i>H</i> : The graph shows the quality factor (Q) over the plate width (w). The markers <i>I</i> to <i>V</i> are referring to the displacement patterns depicted in Figure 4.18.	41
4.20	Nodal lines count matrices from FT-based method for U_z for the widths <i>I</i> to <i>V</i> . Nodal lines count matrices from FT-based method result for the widths <i>I</i> to <i>V</i> . The amplitudes for nodal numbers $u_z(3,1)$ and $u_z(2,1)$ are annotated.	42
4.21	The amplitudes of the nodal numbers $u_z(1,3)$ and $u_z(2,1)$ for path <i>H</i> and path <i>E</i>	43
4.22	The phase of the nodal numbers $u_z(1,3)$ and $u_z(2,1)$ for path <i>H</i> and path <i>E</i>	43

4.23	Plots of the natural frequency (f_n) and the quality factor (Q) for paths F and H . The \circ marker identifies the 1:3 mode, the \blacklozenge marker the 2:1 mode, and the \blacktriangle the lateral 1:0 mode. The width of the first minimum of path H is marked with a dotted line.	44
4.24	Crossing of path F and H : The graph in the middle at left shows the natural frequency (f_n), and the graph at middle right shows the Q-factor (Q). The pictures above and below show the displacement patterns at the widths I to V . Above for the path H , below for path F	45
4.25	The complex amplitudes of the nodal number u_z (1,3) and u_x (1,0) from FT result spitted in modulus at left and argument at right. Above is shown the path H and below the path F	45
4.26	Plots of the natural frequency (f_n) and the quality factor (Q) for paths G and H . The \circ marker identifies the 1:3 mode, and the \blacklozenge marker the 2:1 mode. The width of crossing resonance frequencies is marked with a dotted line.	46
4.27	Crossing of path G and H : The graph at left shows the natural frequency (f_n) over the width w and the graph at right the Q-factor (Q) over the width w	46
4.28	The nodal line count matrices from FT-based method with the displacement matrix U_z for the widths I to V	47
4.29	Plots of the natural frequency (f_n) and the quality factor (Q) for paths G and N . The \circ marker identifies the 1:4 mode, and the \blacklozenge marker the 2:2 mode. The first occurring point of path N is marked with $ $ over the marker.	48
4.30	Avoided-crossing of path G and N : The graph in the middle at left shows the natural frequency (f_n), and the graph at middle right shows the Q-factor (Q). The pictures above and below show the displacement patterns at the widths I to V . Above for the path N , below for path G	49
4.31	The complex amplitudes of the nodal numbers u_z (1,4) and u_z (2,2) resulting from the FT-based method spitted in modulus at left and argument at right. Above is shown the path N and below the path G	49
4.32	Plot of the amplitudes $ \alpha $ identified from FT method, applied to the three displacement components of path N at the minimum Q-factor on the plate width of $302\ \mu\text{m}$	51
4.33	Plots of the natural frequency (f_n) and the quality factor (Q) for paths J , K and, N . The width of the first minimum of path N is marked with a dotted line. The first occurring point of path N is marked with $ $ over the marker.	51
4.34	Crossing of the paths J , K , and N : The graph in the middle at left shows the natural frequency (f_n), and the graph at middle right shows the Q-factor (Q). The pictures above and below show the displacement patterns at the widths I to V . Above for the path N , below in the upper row the path K and in the lower the path J	52

4.35	The complex amplitudes of the nodal numbers $u_z(1,4)$, $u_z(3,0)$ and $u_y(1,0)$ resulting from the FT-based method spitted in amplitude at left and phase at right. Above is shown the path N , in the middle the path K , and below the path J	53
4.36	The quality factor during avoided crossing for the paths J and K	53
4.37	Plots of the natural frequency (f_n) and the quality factor (Q) for paths M and Q . The width of the minimum of path Q is marked with a dotted line. The \circ marker identifies the 1:5 mode, the \diamond marker the 2:3 mode, and the \blacklozenge marker the 3:1 mode. The first occurring point of path Q is marked with $ $ over the marker.	54
4.38	Plot of the amplitudes $ \alpha $ identified from FT method, applied to the three displacement components of path Q at $380\ \mu\text{m}$	55
4.39	Crossing of path M and Q : The graph in the middle at left shows the natural frequency (f_n), and the graph at middle right shows the Q-factor (Q). The pictures above and below show the displacement patterns at the widths I to V . Above for the path Q , below for path M	55
4.40	The complex amplitudes 1:5 and 3:1 from FT result matrices spitted in modulus at left and argument at right. Above is shown the path M and below the path Q	56
4.41	Plot of all paths with identified mode shape interference.	58
1	Plots of the natural frequency (f_n) and the quality factor (Q) for paths L and M . The \blacklozenge marker identifies the 2:3 mode and the \diamond marker the 3:1 mode.	64
2	Avoided-crossing of path L and M : The graph in the middle at left shows the natural frequency (f_n), and the graph at middle right shows the Q-factor (Q). The pictures above and below show the displacement patterns at the widths I to V . Above for the path M , below for path L	64
3	The complex amplitudes of the nodal numbers $u_z(2,3)$ and $u_z(3,1)$ from the nodal line count matrix spitted in modulus at left and argument at right. Above is shown the path L and below the path M	65
4	2D plot of the OOP displacement component u_z for path M in the first half period, derived from complex displacement with Equation 1. Each row shows one width of the the widths I , II , and III	66
5	2D plot of the OOP displacement component u_z for path L in the first half period, derived from complex displacement with Equation 1. Each row shows one width of the the widths I , II , and III	66
6	Plots of the natural frequency (f_n) and the quality factor (Q) for path S . The \bullet marker identifies the 1:6 mode and the \diamond marker the 3:2 mode. The first occurring point of the path is marked with $ $ over the marker.	67
7	Plot of the amplitudes $ \alpha $ identified from FT method, applied to the three displacement components of path S at the widths $420\ \mu\text{m}$, $422\ \mu\text{m}$, $424\ \mu\text{m}$, $426\ \mu\text{m}$, $428\ \mu\text{m}$	67

8	Plots of the natural frequency (f_n) and the quality factor (Q) for paths P and S . The \bullet marker identifies the 1:6 mode, the \blacklozenge marker the 2:4 mode, and the \blacklozenge the 3:2 mode. The first occurring points of the paths are marked with over the marker.	68
9	Avoided-crossing of path S and P : The graph in the middle at left shows the natural frequency (f_n), and the graph at middle right shows the Q-factor (Q). The pictures above and below show the displacement patterns at the widths I to V . Above for the path P , below for path S	68
10	The complex amplitudes of the nodal numbers u_z (1,6) and u_y (3,2) from FT result matrices spitted in modulus at left and argument at right. Above is shown the path P and below the path S	69
11	2D plot of the OOP displacement component u_z for path S in the first half period, derived from complex displacement with Equation 1. Each row shows one width of the widths III , IV , and V	70
12	2D plot of the OOP displacement component u_z for path P in the first half period, derived from complex displacement with Equation 1. Each row shows one width of the widths III , IV , and V	70
13	Plots of the natural frequency (f_n) and the quality factor (Q) for paths O and P . The \bullet marker identifies the 1:6 mode, the \blacklozenge marker the 2:4 mode, and the \blacklozenge the 3:2 mode. The first occurring points of the paths are marked with over the marker.	71
14	Avoided-crossing of path O and P : The graph in the middle at left shows the natural frequency (f_n), and the graph at middle right shows the Q-factor (Q). The pictures above and below show the displacement patterns at the widths I to V . Above for the path P , below for path O	72
15	The complex amplitudes of the nodal numbers u_y (2,4) and u_y (3,2) from FT result matrices spitted in modulus at left and argument at right. Above is shown the path P and below the path O	72
16	Plot of the natural frequencies and the quality factors for anistropic silicon.	73
17	Plot of the natural frequencies and the quality factors for polycrystalline silicon.	73

Nomenclature

C_m	Damping factor for the m th eigenvalue
C_p	Specific heat capacity
E	Young's modulus
E^*	Complex Young's modulus
F	Force
F_0	Characteristic damping frequency of the resonator
I_{in}	Moment of inertia
I_{norm}	Average radial component of the energy flux
Q	Quality factor
T	Temperature of the resonator
Δx	Oscillating displacement in x -direction
Δy	Oscillating displacement in y -direction
Δz	Oscillating displacement in z -direction
Γ	Material dependent loss factor
Ω	Frequency dependent loss factor
α_{th}	Thermal expansion coefficient
$\alpha_{z,kl}$	Complex Fourier coefficient for the OOP displacement
α_z	Complex Fourier coefficient matrix for the OOP displacement
σ	Stress vector
ε	Strain vector
δ	Surface layer thickness
η	Material loss coefficient
γ	Number of supports
κ	Thermal conductivity
λ_{EIGEN}	Complex eigenvalue
λ_m	m th eigenvalue

λ_{WAVE}	Wavelength
\mathbf{F}	External force density
\mathbf{I}_{mech}	Mechanical energy flux vector
\mathbf{K}	Elasticity matrix
\mathbf{K}_{ijkl}	Elements of the fourth-order elasticity tensor
\mathbf{U}	Displacement matrices vector
\mathbf{U}_x	Displacement matrix in x -direction
\mathbf{U}_y	Displacement matrix in y -direction
\mathbf{U}_z	Displacement matrix in z -direction
\mathbf{d}	Displaced field vector
\mathbf{u}	Spacial displacement vector
\mathbf{u}_{xy}	Displacement vector
\mathbf{v}	Velocity vector
\mathbf{x}	Vector from origin to a specific point
\mathcal{O}	Origin of the Euclidian space
\mathcal{P}	Specific point in the the Euclidian space
∇	Vector differential operator
ω	Angular frequency
ρ	Mass density
σ_{ij}	Stress tensor
j	Imaginary unit
θ	Oscillation period
ε_{kl}	Strain tensor
φ	Oscillating rotary displacement in $z - x$ plane
d	Spacial displacement
f	Frequency
f_{EIGEN}	Complex eigenfrequency

f_{SYSTEM}	Frequency of the resonating system
f_n	Resonance frequency, natural frequency
h	Cantilever thickness
k_m	Root of the m th eigenvalue
l	Cantilever length
m	Mass
n	Nodal number
n	parallel nodal count
n_x	longitudinal nodal count
s	Displacement scaling factor for visualization
t	Time
u_x	Displacement component in x -direction
u_y	Displacement component in y -direction
u_z	Displacement component in z -direction
$u_{z,mn}$	Elements of the matrix \mathbf{U}_z
v_p	Phase velocity
w	Cantilever width
x	Cartesian axes
y	Cartesian axes
z	Cartesian axes
E_S^*	Complex surface layer Young's modulus

List of Acronyms

- MEMS** Micro-Electro-Mechanical System
- IoT** Internet of Things
- TED** Thermo-elastic damping
- EB** Euler Bernoulli
- OOP** Out-of-plane
- HO-OOP** Higher order out-of-plane
- RTS** Roof-tilde shaped
- IP** In-plane
- FEM** Finite Element Method
- SAW** Surface acoustic wave
- BAW** bulk acoustic waves
- PDE** Partial differential equation
- FT** Fourier transformation
- DFT** Discrete Fourier transformation
- 2D-DFT** Two dimensional discrete Fourier transformation

Bibliography

- [1] X. Zeng and S. Bao, *Key Technologies of Internet of Things and Smart Grid*. Springer, 2023.
- [2] L. Wei, X. Kuai, Y. Bao, J. Wei, L. Yang, P. Song, M. Zhang, F. Yang, and X. Wang, "The Recent Progress of MEMS/NEMS Resonators," *Micromachines*, vol. 12, no. 6, 2021.
- [3] H. D. Ngo, M. Rasras, and I. A. M. Elfadel, *MEMS Accelerometers*. MDPI - Multidisciplinary Digital Publishing Institute, 2019.
- [4] N.-T. NGUYEN, X. HUANG, and T. K. CHUAN, "Mems-micropumps: A review : Pump analysis and design," *Journal of fluids engineering*, vol. 124, no. 2, pp. 384–392, 2002.
- [5] A. Gemelli, M. Tambussi, S. Fusetto, A. Aprile, E. Moisello, E. Bonizzoni, and P. Malcovati, "Recent trends in structures and interfaces of mems transducers for audio applications: A review," *Micromachines (Basel)*, vol. 14, no. 4, p. 847, 2023.
- [6] L. Pelliccia, F. Cacciamani, P. Farinelli, and R. Sorrentino, "High- q tunable waveguide filters using ohmic rf mems switches," *IEEE transactions on microwave theory and techniques*, vol. 63, no. 10, pp. 3381–3390, 2015.
- [7] Y. Wang, Z. Ma, G. Fu, J. Wang, Q. Xi, Y. Wang, Z. Jia, and G. Zi, "A low-frequency mems magnetolectric antenna based on mechanical resonance," *Micromachines (Basel)*, vol. 13, no. 6, p. 864, 2022.
- [8] Y. Wang, H. Zhang, M. Wang, and X.-S. Zhang, "Distributed micro-energy harvesting for next generation of IoT in various scenarios," *Journal of Micromechanics and Microengineering*, vol. 33, 2023.
- [9] J. M. L. Miller, A. Ansari, D. B. Heinz, Y. Chen, I. B. Flader, D. D. Shin, L. G. Villanueva, and T. W. Kenny, "Effective quality factor tuning mechanisms in micromechanical resonators," *Applied Physics Reviews*, vol. 5, no. 4, p. 041307, 2018.
- [10] M. Jandak, T. Neuzil, M. Schneider, and U. Schmid, "Investigation on different damping mechanisms on the q factor of mems resonators," *Procedia Engineering*, vol. 168, pp. 929–932, 2016. Proceedings of the 30th anniversary Eurosensors Conference – Eurosensors 2016, 4-7. September 2016, Budapest, Hungary.
- [11] S. Schmid, L. G. Villanueva, and M. L. Roukes, *Fundamentals of Nanomechanical Resonators*. Springer International Publishing, 2023.
- [12] A. Gesing, T. Tran, D. Huber, D. Steinmüller-Nethl, G. Pfusterschmied, M. Schneider, D. Platz, and U. Schmid, "The gas-liquid-Q-factor-inversion in MEMS plate resonators," *Journal of Sound and Vibration*, vol. 559, no. 117777, 2023.
- [13] D. Chen, J. Zhao, Y. Wang, and J. Xie, "An electrostatic charge sensor based on micro resonator with sensing scheme of effective stiffness perturbation," *Journal of micromechanics and microengineering*, vol. 27, no. 6, p. 65002, 2017.
- [14] G. Pfusterschmied, J. Toledo, M. Kucera, W. Steindl, S. Zemmann, V. Ruiz-Díez, M. Schneider, A. Bittner, J. L. Sanchez-Rojas, and U. Schmid, "Potential of piezoelectric mems resonators for grape must fermentation monitoring," *Micromachines (Basel)*, vol. 8, no. 7, p. 200, 2017.
- [15] Y. JIMBO and K. Ito, "Energy loss of a cantilever vibrator," *Journal of the Horological Institute of Japan*, vol. 47, pp. 1–15, 1968.
- [16] Q. Liu, Y. Fu, Z. Qin, Y. Wang, S. Zhang, and M. Ran, "Progress in the applications of atomic force microscope (afm) for mineralogical research," *Micron*, vol. 170, p. 103460, 2023.
- [17] H. Lyu, Z. Liu, Z. Wang, W. Yang, X. Xiong, J. Chen, and X. Zou, "A high-resolution MEMS magnetoresistive sensor utilizing magnetic tunnel junction motion modulation driven by the piezoelectric resonator," *Appl. Phys. Lett.*, vol. 121, no. 123504, 2022.

- [18] Z. Zhang, X. Fan, Y. Xu, Y. Wang, Y. Tang, R. Zhao, C. Li, H. Wang, and K. Chen, “Silicon-Cantilever-Enhanced Single-Fiber Photoacoustic Acetylene Gas Sensor,” *Sensors*, vol. 23, no. 17, 2023.
- [19] D. Platz and U. Schmid, “Vibrational Modes in MEMS Resonators,” *Journal of Micromechanics and Microengineering*, vol. 29, no. 12, p. 123001, 2019.
- [20] M. Schlögl, *Energy Harvesters and low power MEMS strain sensors for wind turbine applications*. PhD thesis, TU Wien, 2023.
- [21] M. Stixenberger, “Dissipation and fluctuations: Investigation of anchor losses for micromechanical plate resonators,” Master’s thesis, Technische Universität Wien, Wien, Jan. 2022.
- [22] J. A. Judge, D. M. Photiadis, J. F. Vignola, B. H. Houston, and J. Jarzynski, “Attachment loss of micromechanical and nanomechanical resonators in the limits of thick and thin support structures,” *JOURNAL OF APPLIED PHYSICS*, vol. 101, p. 013521, 2007.
- [23] I. Wilson-Rae, “Intrinsic dissipation in nanomechanical resonators due to phonon tunneling,” *Phys. Rev. B*, vol. 77, p. 245418, Jun 2008.
- [24] K. Y. YASUMURA, T. D. STOWE, E. M. CHOW, T. PFAFMAN, T. W. KENNY, B. C. STIPE, and D. RUGAR, *Quality factors in micron- and submicron-thick cantilevers*, vol. 9. New York, NY: Institute of Electrical and Electronics Engineers, 1999.
- [25] T. V. Roszhart, *IEEE 4th Technical Digest on Solid-State Sensor and Actuator Workshop*, ch. The effect of thermoelastic internal friction on the q of micromachined silicon resonators, pp. 13–16. IEEE, 1990.
- [26] D. Montalvão, R. Cláudio, A. Ribeiro, and J. Duarte-Silva, “Experimental measurement of the complex young’s modulus on a cfrp laminate considering the constant hysteretic damping model,” *Composite structures*, vol. 97, pp. 91–98, 2013.
- [27] M. Ashby, “Overview no. 80: On the engineering properties of materials,” *Acta metallurgica*, vol. 37, no. 5, pp. 1273–1293, 1989.
- [28] P. L. Gould and Y. Feng, *Introduction to Linear Elasticity*. Cham: Springer International Publishing Imprint: Springer, 4th ed. 2018 ed., 2018.
- [29] “Comsol multiphysics, reference manual.”
- [30] A. Logg, *Automated solution of differential equations by the finite element method : the FEniCS book*. Lecture notes in computational science and engineering, Berlin [u.a.]: Springer, 2012.
- [31] A. Frangi, A. Bugada, M. Martello, and P. Savadkoohi, “Validation of pml-based models for the evaluation of anchor dissipation in mems resonators,” *European Journal of Mechanics-A/Solids*, vol. 37, pp. 256–265, 2013.
- [32] P. Fromme, M. Pizzolato, J.-L. Robyr, and B. Masserey, “Lamb wave propagation in monocrystalline silicon wafers,” *The Journal of the Acoustical Society of America*, vol. 143, no. 1, pp. 287–295, 2018.
- [33] M. A. Hopcroft, W. D. Nix, and T. W. Kenny, “What is the young’s modulus of silicon?,” *Journal of Microelectromechanical Systems*, vol. 19, no. 2, pp. 229–238, 2010.
- [34] A. W. Leissa, “The Free vibration of rectangular plates,” *Journal of Sound and Vibration*, vol. 31, no. 3, pp. 257–293, 1973.
- [35] NumPy Contributors, “Numpy fft documentation,” 2022. Accessed on: January 9, 2024.
- [36] M. A. Mahmoud, M. A. Alrahmani, and H. A. Alawadi, “Resonance patterns in cantilevered plates with micro electromechanical systems (mems) applications,” *Microsystem technologies : sensors, actuators, systems integration*, vol. 25, no. 3, pp. 997–1016, 2019.
- [37] E. Kausel, P. Malischewsky, and J. Barbosa, “Oscillations of spectral lines in a layered medium,” *Wave motion*, vol. 56, pp. 22–42, 2015.
- [38] L. Novotny, “Strong coupling, energy splitting, and level crossings: A classical perspective,” *American journal of physics*, vol. 78, no. 11, pp. 1199–1202, 2010.